



NAGOYA INSTITUTE OF TECHNOLOGY

**Chemical vapor deposition of tungsten disulfide (WS_2)
crystals on graphene and hexagonal boron nitride (h-BN)**

by
Amutha Thangaraja

A thesis submitted to the Department of Frontier materials of
Nagoya Institute of Technology
in partial fulfillment of the Requirements for the Degree of
Doctor of Philosophy (Ph.D.)

March 2016

Declaration of Authorship

I, Amutha Thangaraja, declare that this thesis titled, 'Chemical vapor deposition of tungsten disulfide (WS_2) crystals on graphene and hexagonal boron nitride (h-BN)' and the work presented in it are my own.

I confirm that:

- This work was done wholly or mainly while in candidature for a research degree at this University.
- Where any part of this thesis has previously been submitted for a degree or any other qualification at this University or any other institution, this has been clearly stated.
- Where I have consulted the published work of others, this is always clearly attributed.
- Where I have quoted from the work of others, the source is always given. With the exception of such quotations, this thesis is entirely my own work.
- I have acknowledged all main sources of help.
- Where the thesis is based on work done by myself jointly with others, I have made clear exactly what was done by others and what I have contributed myself.

Signed:

Date:

Index

Declaration of Authorship.....	ii
Acknowledgements.....	vi
Abstract.....	viii
Chapter 1 Introduction.....	1
1.1 2D layered materials.....	1
1.1.1 Graphene.....	1
1.1.2 h-BN.....	2
1.1.3 TMDCs (MoS ₂ , WS ₂).....	4
1.2 Structural analogy of 2D layered materials.....	5
1.3 Properties of 2D layered materials.....	5
1.4 Applications of 2D layered materials.....	9
1.5 Methods of 2D materials synthesis.....	11
1.6 Motivation and objectives of current work.....	17
1.7 Organization of the dissertation.....	18
1.8 References.....	19
Chapter 2 Experimental.....	27
2.1 WS ₂ synthesis.....	27
2.1.1 WS ₂ crystal synthesis using WO ₃	27
2.1.2 WS ₂ crystal synthesis using WCl ₆	28
2.2 Graphene.....	30
2.2.1 Synthesis of graphene by APCVD.....	30
2.2.2 Transfer of graphene.....	31
2.3 h-BN.....	31
2.3.1 Synthesis of h-BN by APCVD.....	31
2.3.2 Transfer of h-BN.....	32

Chapter 3	Effect of WO₃ precursor and sulfurization process on WS₂ crystals growth by atmospheric pressure CVD.....	33
3.1	Introduction.....	33
3.2	Materials and methods.....	34
3.3	Results and discussion.....	34
3.3	Conclusions.....	40
3.4	References.....	40
Chapter 4	An effective approach to synthesis monolayer WS₂ crystals using tungsten halide precursor.....	43
4.1	Introduction.....	43
4.2	Materials and methods.....	44
4.3	Results and discussion.....	44
4.4	Conclusions.....	58
4.5	References.....	59
Chapter 5	Synthesis of graphene and study of hydrogen etching of its crystals and film	63
5.1	Introduction.....	63
5.2	Materials and methods.....	64
5.3	Results and discussion.....	64
5.4	Conclusions.....	71
5.5	References.....	72
Chapter 6	Synthesis of WS₂ crystals on transferred graphene and h-BN films.....	76
6.1	Introduction.....	76
6.2	Materials and methods.....	77
6.3	Results and discussion.....	77
6.4	Conclusions.....	82
6.5	References.....	83

Chapter 7	Conclusions and future prospects.....	86
7.1	Conclusions.....	86
7.2	Future prospects.....	87
List of research achievements.....	88	
A	Publications in international journals.....	88
B	Other Publications.....	88
C	Conference presentation.....	89
List of figures.....	90	
List of tables.....	94	

ACKNOWLEDGEMENTS

My deep gratitude goes first to my supervisor **Professor Masaki Tanemura** for selecting me as his student without a hesitation. I highly appreciate the opportunity provided to study under his valuable guidance. He offered me so much advice, patiently supervising me, and always guiding me in the right direction. I've learned a lot from him, without his guidance I could not have completed my dissertation successfully.

I would also like to express my sincere thank **Associate Professor Golap Kalita** for insightful comments and encouragement. He has supported me a lot through my hardest time. I will never forget whatever he did for me. Thank you so much for guiding me in all the time of research and writing this thesis.

I also appreciate the advice of the committee members, and **Professor Tetsuo Soga**, for his critical comments, which enabled me to notice the weaknesses of my dissertation and thereby make the necessary improvements according to their comments.

I acknowledge my indebtedness to **NGK** for providing me with scholarship during my PhD research. Without this support it would not have possible for me to complete this research.

I am so thankful to my senior **Dr. Zurita Zulkifli, Dr. Pradip Ghosh, Dr. Mohd Zamri Yusop and Dr. Yazid Yakob** for cheering me up to do research. I also thank my lab mates in for the stimulating discussions, for the sleepless nights we were working together before deadlines, and for all the fun we have had in the last years. Also I thank my friends **Mr. Sachin Shinde, Mr. Mohamad Saufi Rosmi, Mr. Riteshkumar Vishwakarma, and Miss. Nor Dalila, Miss. Ashmi Mewada,** I am specially thankful to all masters and bachelor students of my lab for their help naming some **Mr. Matsui, Mr. Tsuchiya, Mr. Hirano, Mr. Sugiura, Mr. Wakamatsu, Mr. Watanabe, Mr. Nakamura, and Mr. Taneyama,** they were always present whenever I needed them to help me and solving my problem.

I want to thank my dear akka (sister) **Miss. Vijitha Thangaraja.** Thank you so much for providing me opportunity to work in Japan and giving such a great experience in my life. You always provided valuable advices. And I would like to thank my mama **Mr. Arulkumaran Subramanian** for supporting me.

I would like to thank my family **Amma, Appa, Akka (Mageswari Kumaresan, Jeyalakshmi Ganesh, Suji Selvakumar), Thangachi, (Bala, Subha), Anni (Subana, Suganya) and Sridhar Anna** for supporting throughout my carrier.

Abstract

Graphene, a two dimensional (2D) layered carbon nanomaterial has been the subject of intense interest because of its attractive and exceptional physical and chemical properties. Over the past few years, 2D layered inorganic nanomaterials (2D-LINs) have attracted attention because of their unique thickness dependent physical and chemical properties and potential technological applications. Some 2D-LINs like MoS₂, WS₂ and SnS₂ have been recently developed and employed in various applications because of their layer-dependent electrical properties. This thesis contributes to the synthesis of large size WS₂ crystal on graphene and hexagonal boron nitride (h-BN) by atmospheric pressure chemical vapor deposition (APCVD) and their characterization.

Chapter 1 describes the general introduction of 2D layered materials including graphene, h-BN and transition metal dichalcogenides (TMDCs), with regard to their properties, applications, physical and chemical synthesis methods.

Chapter 2 deals with the experimental methods for WS₂ crystal synthesis, graphene synthesis and transfer, h-BN synthesis and transfer.

Chapter 3 is about the effect of WO₃ precursor and sulfurization process on WS₂ crystals. The quantity of WO₃ precursor spread over SiO₂/Si substrate significantly affect the nucleation density and numbers of layer for triangular-shaped WS₂ crystals. Larger triangular crystals (~70 μm) were obtained by controlling the amount of WO₃ precursor as nucleation and growth sites. Pyramid-like few-layers stacked structure of WS₂ crystals were obtained from densely spread WO₃ powder. By controlling the amount of WO₃ precursor and the rate of sulfur introduction in the high temperature chemical vapor deposition (CVD) zone, large WS₂ crystals were synthesized.

Chapter 4 discusses an effective approach to synthesize high quality monolayer WS₂ crystals using tungsten hexachloride (WCl₆) as solid precursor in APCVD process. In this technique, 0.05M solution of WCl₆ in ethanol was drop casted on SiO₂/Si substrate to create a uniform distribution of the precursor, which was reduced and sulfurized at 750 °C in argon atmosphere. The growth of triangular, star-shaped, as well as dendritic WS₂ crystals on the substrate was observed. The crystal geometry evolved with shape and size of the nuclei as observed from the dendritic structures. Our finding shows an easier and effective approach to grow WS₂ monolayer crystals using tungsten halide coating on substrate surface rather than evaporating the precursor for gas phase reaction.

In Chapter 5, synthesis of graphene and the effect of hydrogen etching were studied upon graphene crystals and continuous film. Highly anisotropic and fractal etching was demonstrated with the formation of hexagonal graphene hole, ribbon like structures and hexagonal-hexagonal stacking

(stacking of three hexagonal layers) along with the snowflake dendritic crystals. This finding can be significant to understand the nucleation and growth of graphene crystals as well as their selective etching process to fabricate well-defined structures.

Chapter 6 discusses about the synthesis of WS₂ crystals on graphene and h-BN by APCVD. Triangular WS₂ crystals of around 2-7 μm in size were obtained. Vertically aligned WS₂ crystals were observed on graphene.

Chapter 7 summarizes the whole thesis and future prospects.

Dedicated to
My lovely **அம்மா** (Amma) and
Handsome **அப்பா** (Appa)

CHAPTER 1

Introduction

1.1 Introduction to different 2D layered materials

1.1.1 Graphene

Graphene is a hexagonal structure made of a single layer of sp^2 hybridized carbon atoms [1]. Graphene is defined as a sheet of carbon atoms bound together with double electron bonds (called a sp^2 bond) in a thin film which is only one atom thick. Atoms in graphene are arranged in a honeycomb-style lattice structure as shown in figure 1-1.

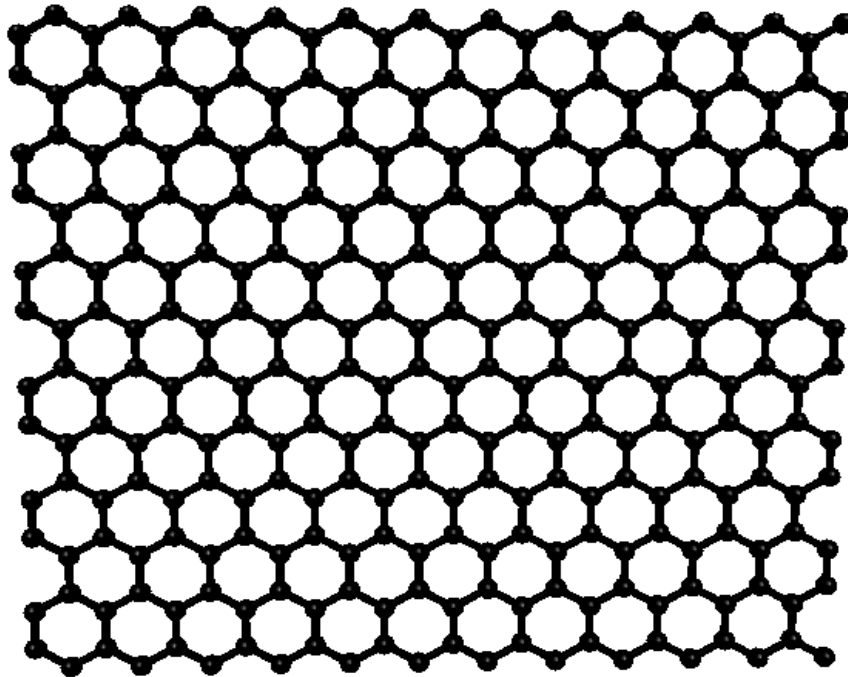


Figure 1-1 Schematic diagram of graphene with honeycomb lattice

By stacking of these layers on top of each other, the well-known 3-dimensional graphite crystal is formed. Thus, graphene is nothing else than a single graphite layer. The quasi-1-dimensional carbon nanotubes are formed by rolling the graphene sheets. By adding five-membered rings it is possible to form the quasi-0-dimensional fullerenes. The most prominent one is the Buckminster fullerene (C_{60}), which is also known as bucky ball and looks like a football (soccer ball).

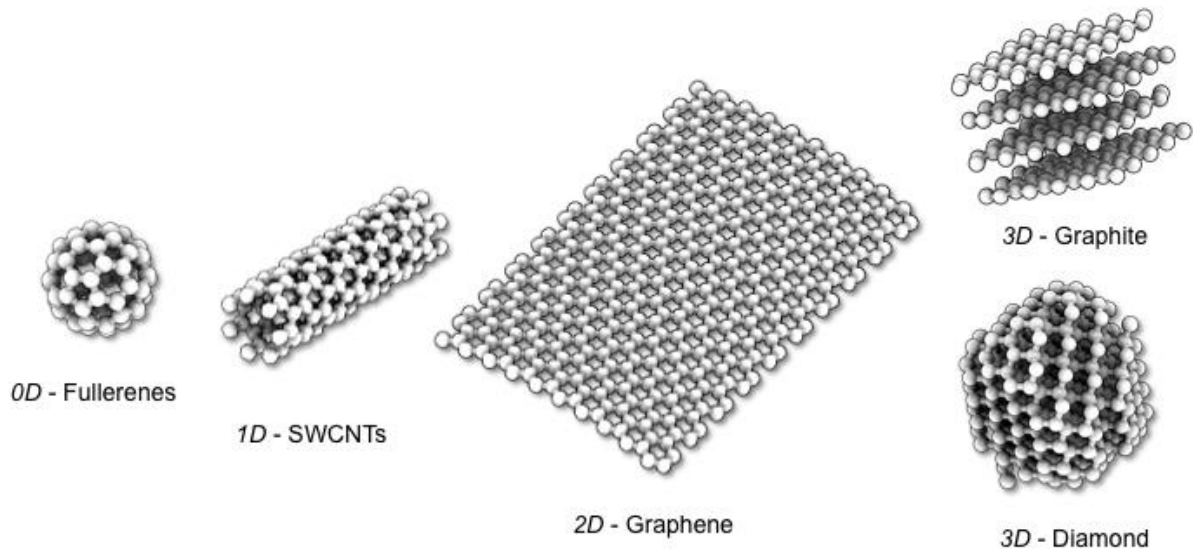


Figure 1-2 Graphene: the basic building block for other carbon allotropes, graphite (3D), fullerene (0D), and CNT (1D)^a.

1.1.2 h-BN

BN is a high bandgap semiconductor formed of B and N atoms. BN can be obtained in three different crystallographic structures i.e. cubic BN, rutile and h-BN as shown in figure 1-3. The hexagonal form (h-BN) is a sp^2 hybridized layered structure of B and N atoms analogous to graphene. The layered structure can also be stacked in the rhombohedral form. The first synthesis of BN was carried out in 1842 by Balmain [2, 3]. h-BN is formed by alternating B and N atoms forming honeycomb-like networks, similar to graphene [4, 5] as shown in figure 1-4. However, h-BN with a high bandgap is an insulator in contrast to semi metallic (zero bandgap) graphene.

^a<http://graphita.bo.imm.cnr.it/graphita2011/graphene.html>

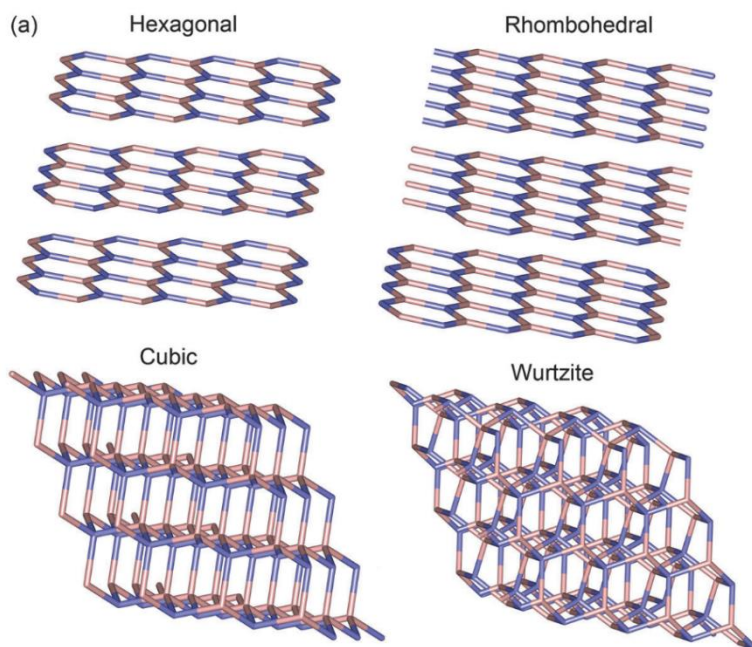


Figure 1-3 Boron nitride crystal structures

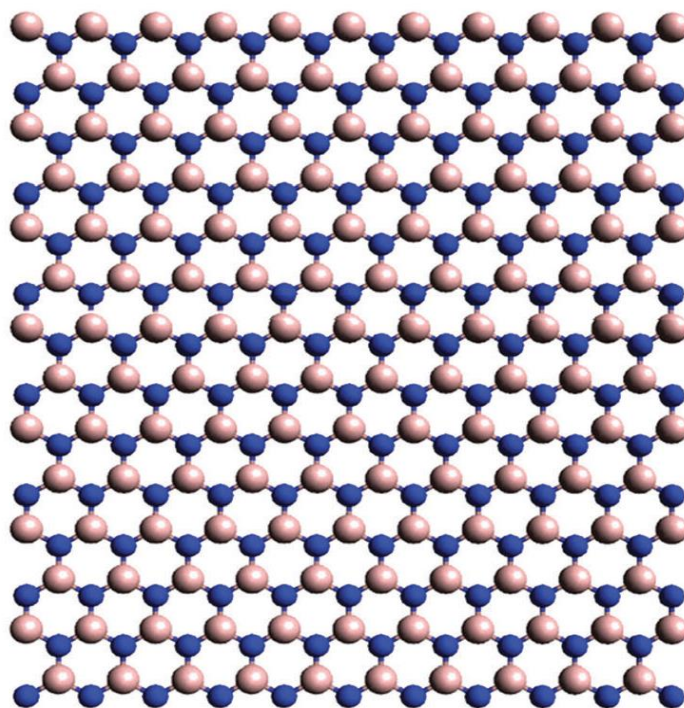


Figure 1-4 Structure of h-BN is formed by alternating B and N atoms (reprinted with permission from Amir Pakdel et.al Chem. Soc. Rev., 2014) [107]

1.1.3 TMDCs

TMDCs monolayers are atomically thin semiconductors of the type MX_2 , with M a transition metal atom (Mo, W, etc.) and X a chalcogen atom (S, Se, or Te.). One layer of M atoms is sandwiched between two layers of X atoms [6, 7]. In particular, monolayer Mo and W-based TMDCs (MoS_2 , MoSe_2 , WS_2 , WSe_2 , etc.), which become direct band gap semiconductors, exhibit excellent on/off current ratios in field-effect transistors (FETs), [8,9] strong photoluminescence (PL), [10-13] and unique spin-valley physics [14-16]. Therefore, TMDCs are expected to be a possible component in future electronic and optoelectronic devices [6,17]. WS_2 is uniquely interesting for optoelectronic devices because its conduction band seems aligned to the Dirac point of graphene and its band gap is well matched to the solar spectrum. For WS_2 , the crystal belongs to the P63/mmc space group ($a = 3.155$, $c = 12.36$), [18] and its planar projection shows a perfect hexagonal lattice of S atoms, with interleaved W atoms coordinated by S in a trigonal prismatic arrangement. The structure is similar to that of MoS_2 and some of the other dichalcogenides.

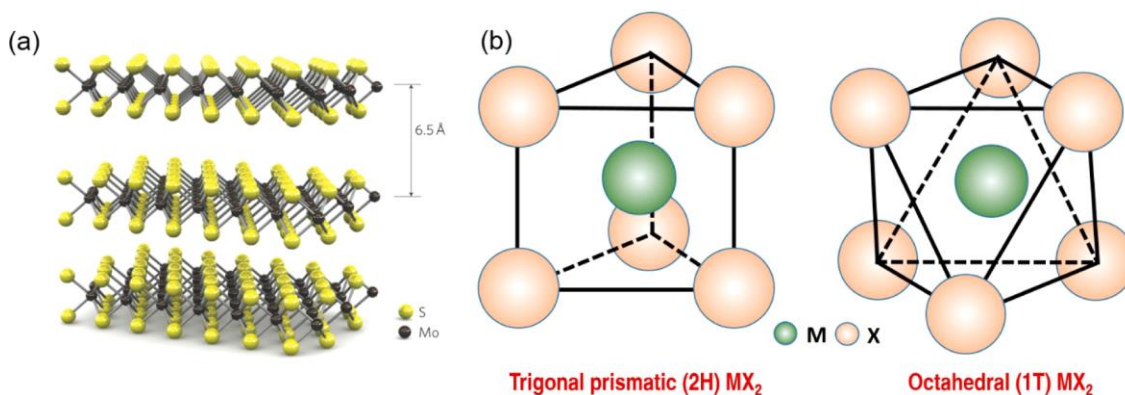


Figure 1-5 Crystal structures of TMDs with a typical formula of MX_2 . (a) 2D model of the MoS_2 crystal structure. Reprinted with permission from ref [19]. Copyright 2011 Macmillan Publishers Ltd. (b) Unit cell structures of 2H- MX_2 and 1T- MX_2 .

1.2 Structural analogy of 2D layered materials

Boron nitride nanosheets (BNNSs), MoS_2 , and WS_2 are hexagonal structures analogous to graphene (Figure 1-6). The bond between C-C (in graphene) and Mo/W-S (in MoS_2 and WS_2) is covalent whereas B-N is ionic (in BN). The layers of BNNSs, MoS_2 , and WS_2 are stacked together by van der Waals forces similar to graphene [25]. In the case of MoS_2 and WS_2 , weak van der Waals forces are holding adjacent sulfur sheets together [20]. Three dimensional (3D) crystals are formed by stacking up 2D sheets by van der Waals forces [26]. Carbon allotropes such as carbon nanotubes (CNTs), fullerenes (C_{60}), and graphene have delocalized π electrons [1, 27]. The key difference between the organic (graphene) and inorganic nanosheets is the presence of the delocalized π electron distribution.

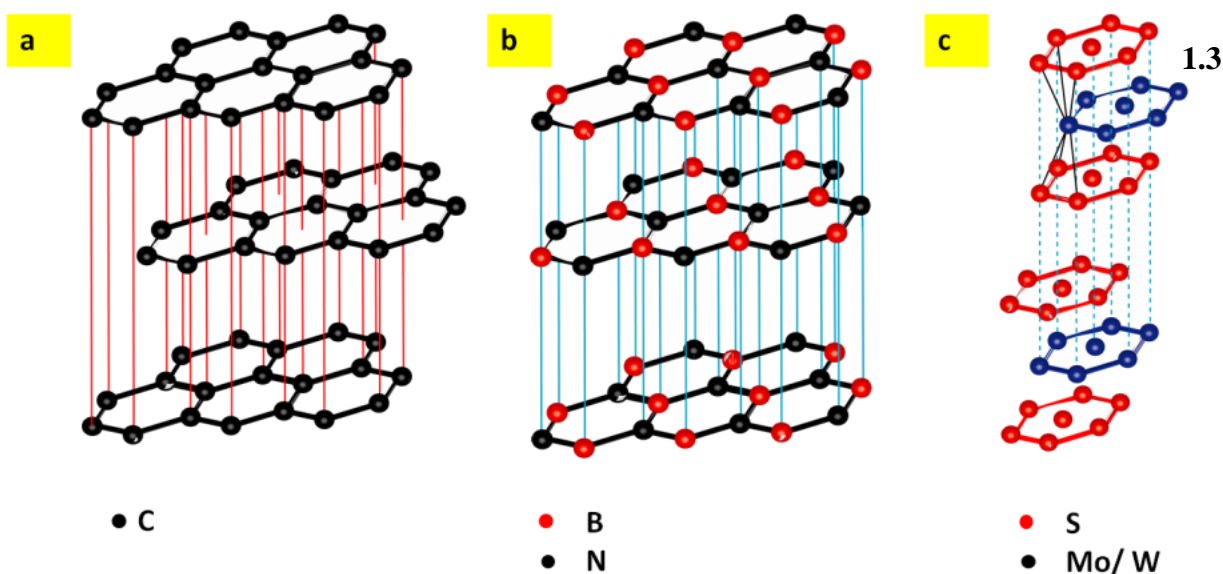


Figure 1-6. Layered structure of (a) graphite, (b) hBN, (c) molybdenum disulfide/ tungsten disulfide^b

1.3 Properties of 2D layered materials

Graphene

Mechanical properties

Single layer of graphene is one of the most rigid materials. Young's modulus of graphene is a remarkably high ~ 1 TPa with an ultimate tensile strength of 130 GPa [28]. Graphene is harder than diamond and stronger (~ 300 times) than steel. Although graphene is robust, this nanosheet can be

^bTexas Tech University, Rozana Bari, August 2014

stretched up to 20% of its initial length. Having these mechanical properties, mechanically strong composite material can be produced with graphene.

Thermal properties

Graphene has very high thermal conductivity. The thermal conductivity of graphene is $5000 \text{ W m}^{-1} \text{ K}^{-1}$ whereas, the thermal conductivity of single walled nanotube (SWNT) is $3500 \text{ W m}^{-1} \text{ K}^{-1}$ [29]. Ho et al. reported the experimental thermal conductivity of bulk graphite as $2000 \text{ W m}^{-1} \text{ K}^{-1}$ [30]. Nika et al. compared thermal conductivity of bulk graphite and graphene and they mentioned (theoretically) that thermal conductivity of single layer graphene depends on the flake size and ranges from $3000\text{-}5000 \text{ W m}^{-1} \text{ K}^{-1}$ [31].

Electrical properties

In graphene each C atom is connected to three other C atoms and leaves one free electron. The electrical conductivity of graphene is 6000 S cm^{-1} [33]. Moreover, the resistance of graphene is $10^{-6} \text{ }\Omega\text{cm}$ at low temperature. Graphene is a zero-band gap semiconductor with an electronic mobility of $150,000 \text{ cm}^2 \text{ V}^{-1} \text{ s}^{-1}$ at room temperature [34].

Properties of BNNSs and TMDCs

Electrical insulation

Due to the ionic bonding between B and N, BNNSs are electrically insulating, with a large electronic bandgap ($\sim 4\text{-}6\text{eV}$) [35, 36]. The electrical resistivity of BNNSs is 10^{17} and $10^{14} \text{ }\Omega\text{cm}$ at room temperature and at 200°C respectively [37]. BNNSs composites can be used as electrical insulator in electronics.

Thermal conductivity

The thermal conductivity of BNNSs is $2000 \text{ W m}^{-1} \text{ K}^{-1}$ [38]. CNTs and graphene are thermally and electrically conductive, therefore cannot be used in thermal management of electronic materials. Since BNNSs are electrically insulating and thermally conductive, BNNSs composite can be

used in thermal management of high power electronics. In presence of BNNSs the thermal conductivity of nanofibrillated cellulose (NFC) increases from $0.035 \text{ W m}^{-1} \text{ K}^{-1}$ to $26.2 \text{ W m}^{-1} \text{ K}^{-1}$ while loading by 5% of nanofiller [39].

For applications such as high-speed electronics and dielectronics, a material with property of quick heat releasing as well as electrical insulation is necessary. BNNSs can be used as nanofiller in polymer materials to improve the thermal stability, thermal conductivity, and dielectric properties in polymeric composites. For example, the dielectric constant increases with BNNSs loading in polymer composite of poly (methylmethacrylate) (PMMA) [40].

Chemical inertness and thermal stability

BNNSs are oxidation-resistant and chemically inert. Oxidation resistance of metals can be improved at high temperatures by applying BNNSs coatings on metal surface. A very recent study by Li et al. has shown that BNNSs can sustain up to $850 \text{ }^\circ\text{C}$ [41]. Another study performed by Liu et al. indicated that very thin BNNSs coating ($\sim 5\text{nm}$) on top of nickel prevents oxidation upto 1100°C [42]. Hence, BNNSs are more suitable for high-temperature applications since it is more resistant to oxidation than graphene [43].

Optoelectronic properties

WS_2 and MoS_2 nanosheets possess different optical and electrical properties than from bulk form. For an example, MoS_2 nanosheets are semiconducting, with a direct electronic band gap of $\sim 1.9 \text{ eV}$ [59, 60], while the bulk material exhibits indirect band gap of 1.2 eV (Figure 1-7). Similarly, monolayer WS_2 has a direct band gap of $\sim 2.1 \text{ eV}$ that is different from bulk WS_2 (1.3 eV) (Figure1-8) [43, 2]. For both of these materials, the bulk material shows indirect band gap since the bottom of the conduction band and the top of the valence band is situated at different reciprocal lattice points (K, M, and Γ) . However, for the monolayer materials, the positions of bottom of the conduction band and the top of the valence band are at same K point of the x (wave vector) axis. In the figures, 1 Hartree (E_h) is equivalent to 27.21 eV . Since these materials exhibit direct band gap behavior, they have strong photoluminescence [45, 46] and spin polarization (degree of alignment of electron's spin) [47]. These materials are also suitable for photovoltaics in a sense that they can be used as absorber materials in thin film solar cell [48]. So, these TMDCs show various potential applications in nano and optoelectronics [23].

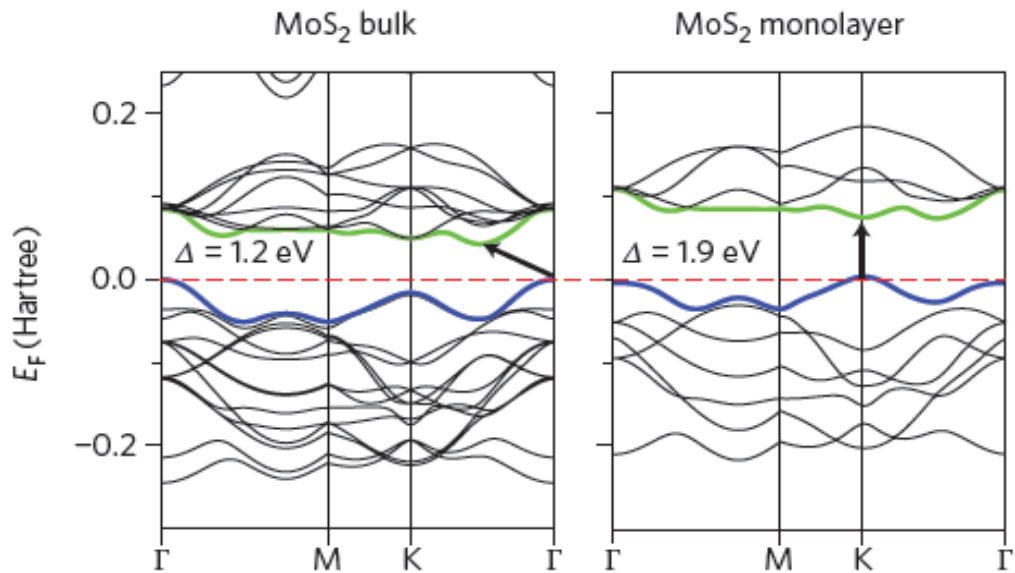


Figure 1-7. Electronic band gap structure of bulk and monolayer MoS₂ (Reprinted with permission from Wang et al., 2012) [43].

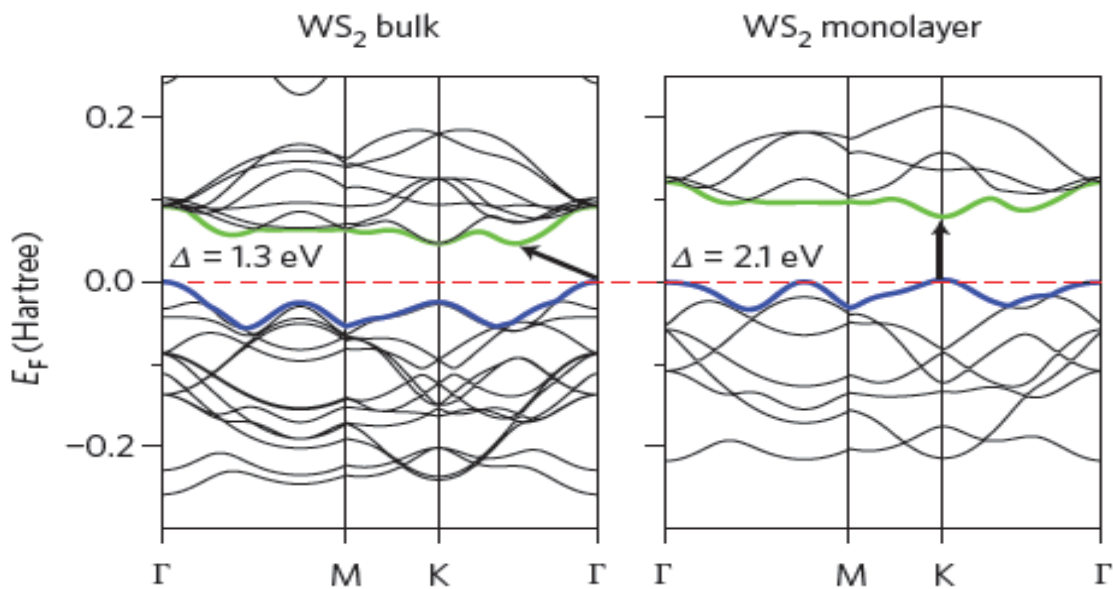


Figure 1-8. Electronic band gap structure of bulk and monolayer WS₂ (Reprinted with permission from Wang et al., Nature Nanotechnology, 2012) [43].

1.4 Applications of 2D layered material

Applications of graphene

Graphene is extensively used in fabricating sensors, solar cells, flexible electronics, electrically conductive composites, and also as thermal management material in electronic circuits [32]. Moreover, the high surface area of graphene is also relevant for various applications such as catalysis, oil absorption, electrodes for super-capacitors, and batteries, energy storage applications. Graphene is also used as nanofiller in polymer to make polymer nanocomposite. The incorporation of graphene (with a very low filler content) makes the insulating polymer to electrically conductive nanocomposite and these composite are widely used in electrostatic dissipation devices and electromagnetic interference shielding which require electrical conductivity at the range of about 10^{-6} Sm^{-1} [48]. The cost effectiveness and lightweight of these composites are attractive features [49-63]. Figure 1-9 shows the diversity of applications of graphene

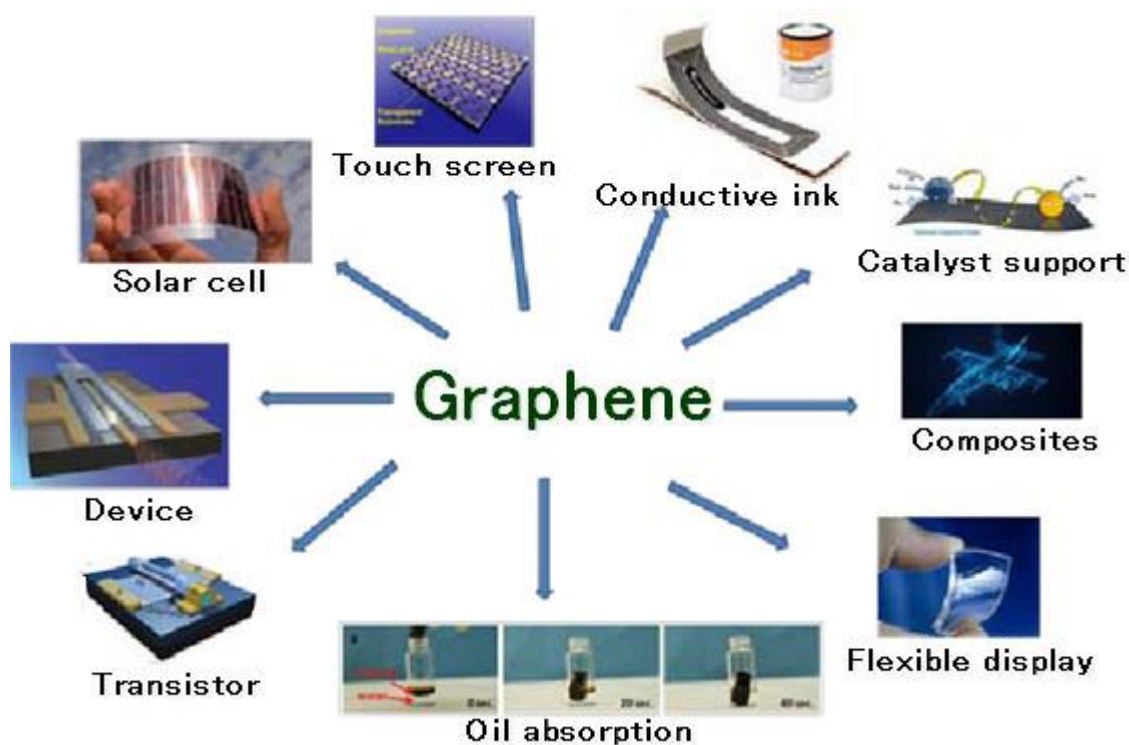


Figure 1-9. Numerous applications of graphene^c

^cTexas Tech University, *Rozana Bari*, August 2014

Applications of BNNSs and TMDCs

BNNSs adsorb organic contaminations and thermally stable [41]. Also BNNSs are thermally conductive and mechanically strong; these collective properties are used to fabricate cellulose wires with BNNSs [23, 39]. The combination of thermal conductivity and electrical insulating property of BNNSs has potential applications in fabricating die attachments, encapsulation of electric wire, and electronic packaging materials [40, 64]. The direct band gap of MoS₂ nanosheets can be potentially used in transistors, light-emitting diodes, solar cells [65] and field-effect transistors (FET) [66, 67], ultra-high strength nanocomposites. WS₂ is a potential semiconducting material for solar energy conversion [68 - 72] and also extensively used as electrode in lithium batteries, [21, 73, 74], catalyst shock absorbers [22, 75], and hydrogen storage [76]. These different types of applications are shown in Figure 1-10.

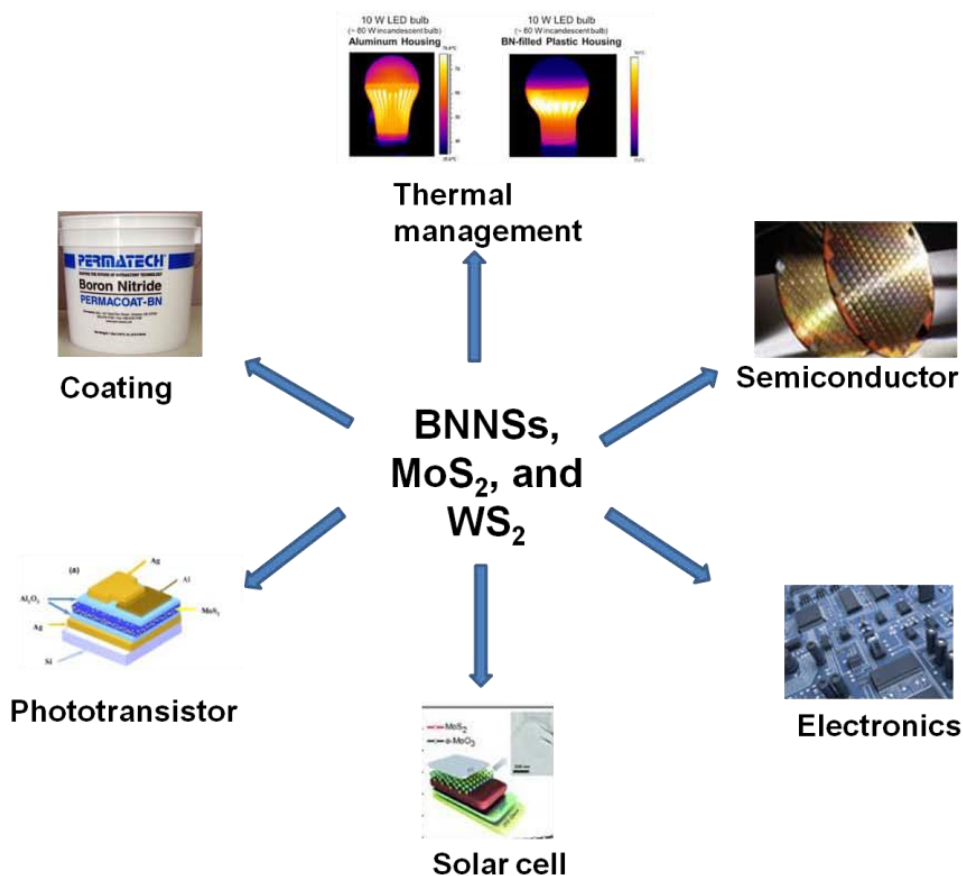


Figure 1-10. Numerous applications of BNNSs, MoS₂, and WS₂^d

^dTexas Tech University, Rozana Bari, August 2014

1.5 Methods of 2D materials synthesis

There are several methods to approaches to synthesize 2D materials. A short introduction to different synthesis method is discussed .This thesis mainly discusses APCVD.

Mechanical exfoliation

(a) Micromechanical cleavage

In cooperation the graphene flake and Nobel Prize for Physics in 2010 are credited to the micro mechanical cleavage of HOPG (Highly Ordered Pyrolytic Graphite) in 2004 [77, 78, 79]. The common idea of this method is the cleavage of graphene layers from the bulk HOPG surface. The procedure is presented in Figure.1-11.

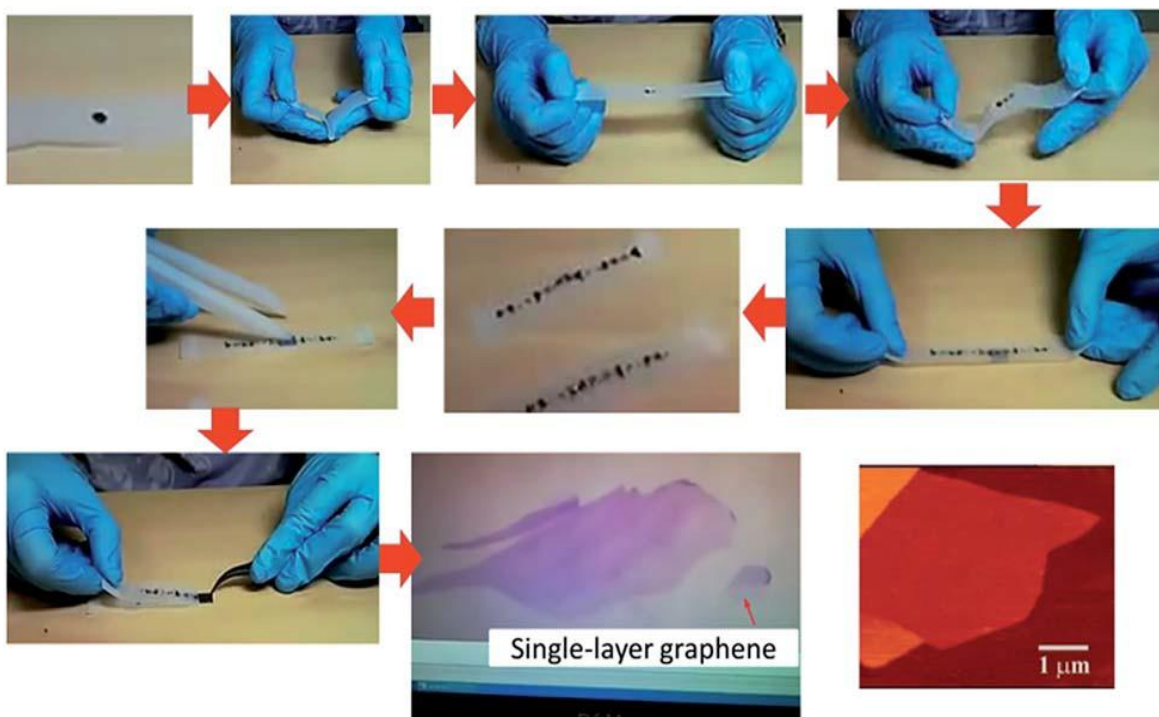


Figure 1-11 An illustrative procedure of the Scotch-tape based micro- mechanical cleavage HOPG (Reprinted with permission from Min Yi et al, J. Mater. Chem. A, 2015) [106].

(b) Sonication

Sonication assisted liquid-phase exfoliation of graphite to give graphene has made the large-scale production of graphene possible. Following their experience in dispersing carbon nanotubes by sonication, Coleman's group first reported the high-yield production of graphene by the sonication assisted liquid-phase exfoliation of graphite in 2008 [80].

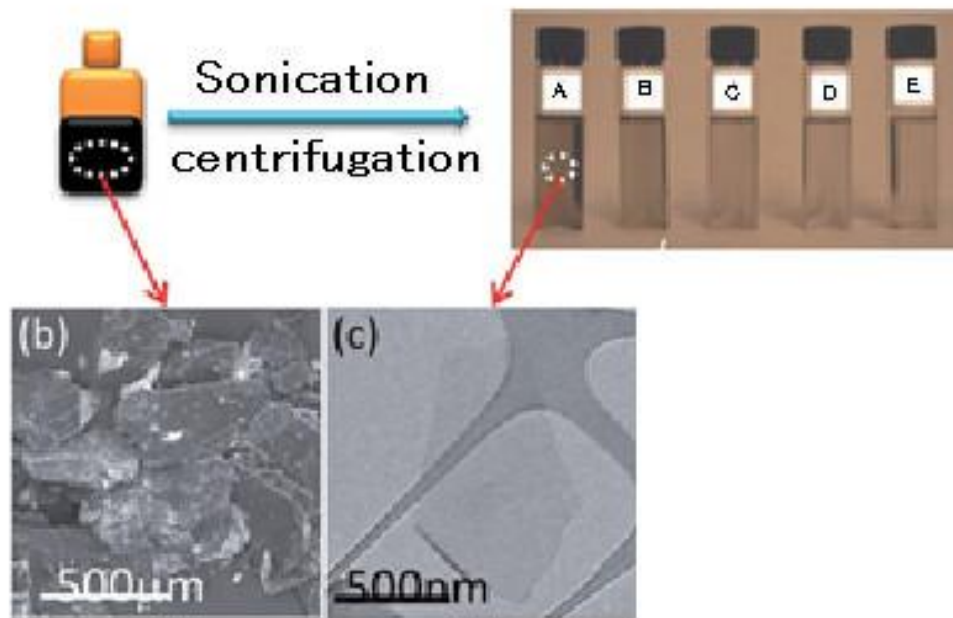


Figure 1-12 (a) Sonication of graphite dispersion giving graphene dispersion. (b) SEM image of the initial graphite flakes. (c) TEM image of the exfoliated graphene. (Reprinted with permission from Min Yi et al, J. Mater. Chem. A, 2015) [106].

(c) Ball milling

Ball milling, a common technique in the powder production industry, is a good candidate for generating shear force. The mechanical mechanism of ball milling in exfoliating graphene can be illustrated in Figure .1-13.

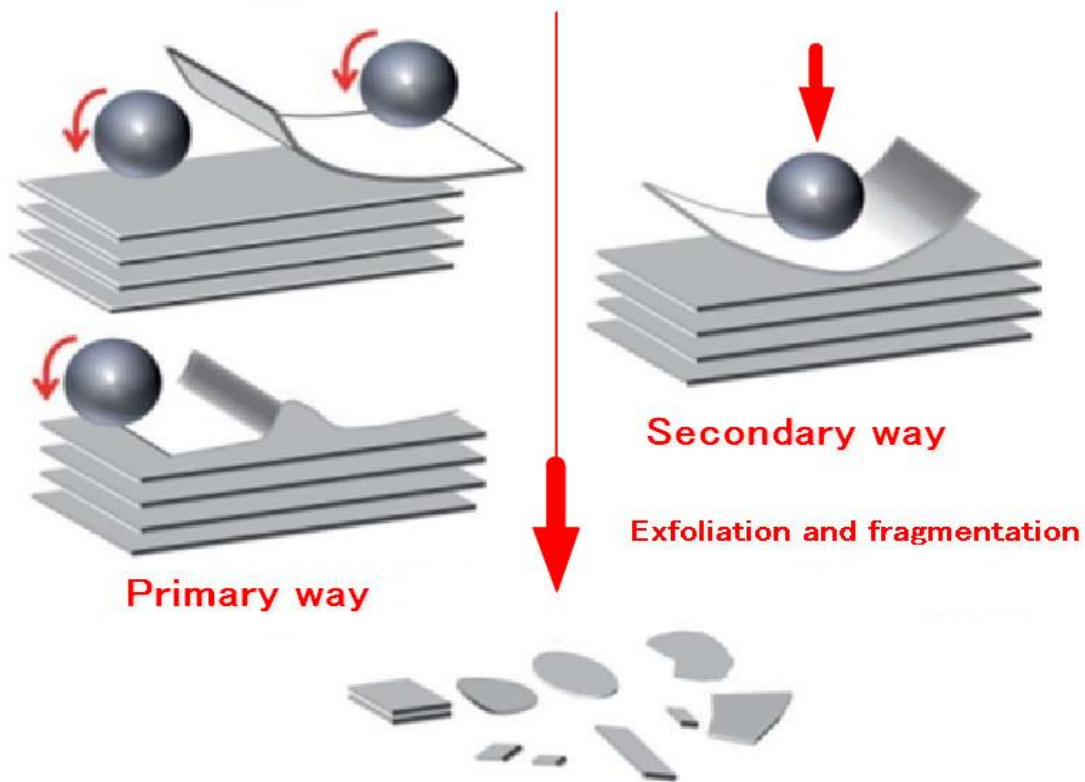


Figure 1-13 Illustration of mechanical mechanism for exfoliation via ball milling. (Reprinted with permission from Min Yi et al, J. Mater. Chem. A, 2015) [106].

Liquid exfoliation

The recent developments in the liquid exfoliation of layered crystals using Geim and Novoselov's 2004. To date, liquid exfoliation has produced graphene, h-BN, a number of TMDs, a range of clays, many oxides and hydroxides, and a scattering of other exfoliated nanosheets. Figure 1-14 illustrates the outline the four main liquid exfoliation techniques for layered materials.

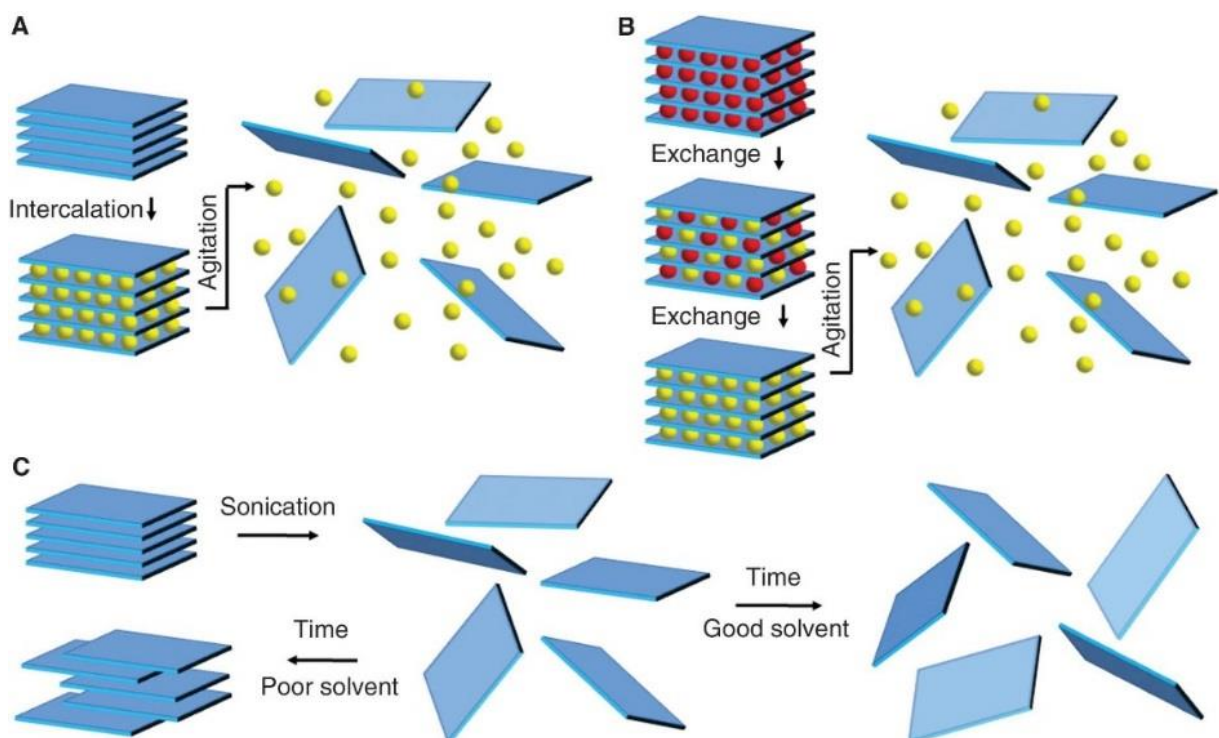


Figure 1-14 Schematic description of the main liquid exfoliation mechanisms, where

(A) **Ion intercalation:** Ions (yellow spheres) are intercalated between the layers in a liquid environment, swelling the crystal and weakening the interlayer attraction.

(B) **Ion exchange:** Some layered compounds contain ions between the layers so as to balance surface charge on the layers. These ions (red spheres) can be exchanged in a liquid environment for other, often larger ions (yellow spheres). As above, agitation results in an exfoliated dispersion.

(C) **Sonication assisted exfoliation:** The layered crystal is sonicated in a solvent, resulting in exfoliation and nanosheet formation. (Reprinted with permission from Min Yi et al, *J. Mater. Chem. A*, 2015) [106].

Chemical vapor deposition

CVD growth of graphene

The earliest reports on CVD synthesized thin graphite materials are from the 1970s in the early days of investigation into the CVD process [81-83]. One of the most important advances in the CVD growth of single layer graphene was reported in 2009. Li et al. prepared large-area graphene films via CVD on copper foils [84] and the grown graphene films were mostly of single-layer thickness, with less than 5% double or triple layers. Besides single or bilayer graphene, it is also important to gain control over the number of layers in CVD grown graphene. Gong et al. controlled the number of layers of CVD graphene to within [85-94] layers mainly by controlling the flow of hydrogen, the thickness of the deposited nickel catalyst, and the growth temperature and time [95]

CVD growth of single crystal graphene was successfully executed on commercial transition metal substrates like copper foils. Vlassioux et al. [91] grew large single crystal graphene via a CVD process under an atmosphere of hydrogen, methane and argon with copper foils as substrates and catalysts, and hydrogen as a co-catalyst. The size of the obtained graphene was around 10 mm, and the graphene showed weak binding to the copper foil substrates.

CVD growth of 2D boron nitride (BN)

Since the 1970s, GaAs thin films have been widely studied via molecular beam epitaxy. Other group III–V compounds such as BN have also attracted much interest from the scientific community. However, due to the high cost of molecular beam epitaxy BN, CVD is introduced to lower the cost and promote the widespread production. BN is very suitable for CVD growth since the precursors of B and N are mostly gaseous sources. Several works have demonstrated the CVD growth of 2D BN thin films. For example, Shi et al. demonstrated CVD growth of h-BN thin films with a thickness of a few to tens of nanometers [96]. Similar work by Song et al. demonstrated the large-scale CVD growth of high quality h-BN films consisting of 2 to 5 atomic layers [97]. Ammonia borane ($\text{NH}_3\text{-BH}_3$) was applied as the precursor of BN, and was carried along by a gas flow of H_2/Ar (15% vol H_2 , 85% vol Ar). The deposition was done at a temperature of around 1000°C with a typical growth time of 30–60 minutes

CVD growth of 2D transition metal dichalcogenides

Single- and few-layer 2D TMDC nanosheets can be obtained from either top-down routes like mechanical exfoliation or bottom-up processes like CVD. The aims of the CVD growth of TMDCs are to grow few- and single- layer sheets, and to prepare single crystal TMD atomic layers. CVD growth of TMDCs dates back to 1988 when Hofmann demonstrated MOCVD growth of MoS_2 and WS_2 on various substrates [98]. The precursors of Mo and W were hexacarbonyls of the corresponding

transition metals and the precursor of S was vaporized sulfur or hydrogen sulfide gas. However, the films are normally thick. To prepare two dimensional atomic layers or single layers, several techniques in CVD have been developed. Liu et al. reported a two-step thermolysis process [99], in which ammonium thiomolybdates $[(\text{NH}_4)_2\text{MoS}_4]$ were dip-coated onto the substrates, and were converted to MoS_2 by annealing at 500°C under an Ar/H_2 atmosphere followed by sulfurization at 1000°C using sulfur vapor along with Ar gas. High-resolution TEM analysis identified that the thickness of MoS_2 is three layers, and the MoS_2 films could be easily transferred onto other arbitrary substrates. The sulfurization process with S vapor drastically enhanced the crystallinity of MoS_2 . In another work, few layer TMDs were obtained through conventional CVD processes. Zhan et al. reported the CVD growth of large-area MoS_2 few-layer atomic layers based on the sulfurization of Mo metal films [100]. A thin layer of Mo was deposited on SiO_2 using an electronic beam evaporator before being placed in the tube furnace for CVD growth. Sulfur vapor was introduced into the process by heating the sulfur powder. The size of the grown MoS_2 depended on the size of the substrates, and the thickness of the MoS_2 depended on the thickness of the Mo films deposited on the substrates. Besides elemental precursors, transition metal oxides could also be applied as the precursors. For example, Lee et al. synthesized few-layer MoS_2 using CVD [101]. In this work, MoO_3 was converted to MoS_2 by sulfurization. McCreary et al. grew monolayer MoS_2 films on graphene substrates [102]. In this study, the precursor for Mo was MoCl_5 which was different from most other works, and MoS_2 films with 1, 2 or 3 layers were obtained by altering the amount of MoCl_5 . CVD growth of single crystal TMDCs is still a big challenge to date, and the obtained single crystal TMDC flakes or domains achieved so far are relatively small compared to the single crystal graphene flakes. However, some success in the CVD growth of single crystal TMDCs with large domain sizes has been realized recently. To grow single crystal TMDCs, the main solutions are still to reduce the nucleation density to form larger domains/grains, and to control the growth process to obtain individual domains that form fewer or no domain boundaries. Zhang et al. demonstrated the CVD growth of monolayer single crystal WS_2 nanosheets on single crystal sapphire substrates using WO_3 and S as precursors [103]. The products were monolayer single crystal WS_2 nanosheets with sizes up to $50\ \mu\text{m}$. Rong et al. demonstrated the CVD growth of large single crystal domains of WS_2 [104]. By controlling the time and amount of sulfur introduced before and during the CVD process, monolayer WS_2 domains with sizes up to $370\ \mu\text{m}$ were obtained. Besides the TMDC materials mentioned above, hetero structures based on TMDC materials are attracting great interest. Bernardi et al. have theoretically demonstrated that bilayer solar cells of MoS_2 /graphene of 1 nm thickness could achieve over 1% power conversion efficiency [105]. These theoretical works predicted that bilayers of TMDC/TMDC or TMDC/graphene could be promising in various fields of applications. There are several experimental works on TMDC based hetero structures.

1.6 Motivation and objectives of current work

TMDCs are fundamentally and technologically intriguing due to their unique electronic and optical properties. The behaviors of TMDCs are varied, ranging from insulating, semiconducting, truly metallic to superconducting. TMDCs such as MoS₂, MoSe₂, WS₂ and WSe₂ possess a bandgap which can be suitable for field-effect transistors (FETs) and optoelectronic devices. Among the TMDCs, WS₂ is uniquely interesting for optoelectronic devices because its conduction band seems aligned to the Dirac point of graphene and its band gap is well matched to the solar spectrum. We have used APCVD method to synthesis WS₂ crystals. The main advantages of APCVD technique is large area synthesis of atomic thin layer of TMDCs and larger size crystals can be grown. Synthesis of WS₂ crystals on various substrates such as SiO₂/Si, graphene and h-BN can be significant. Large number of theoretical work on synthesis of WS₂ on graphene and h-BN has been done using exfoliation. Normally exfoliated samples are only few microns, it cannot be suitable for large area applications. Hence substrate dependent WS₂ crystal growth was explored by CVD technique. The sulfurization of WO₃ with introduction of sulfur vapor is critical to obtain WS₂ crystals by APCVD

The objective of this work is the development of the growth methods for monolayer WS₂ crystals by APCVD using various precursors on transferred CVD graphene and h-BN. The final goal is to synthesize high quality and large size monolayer WS₂ crystals. The synthesis of large area individual crystals with controllable thickness is desirable for various applications. To achieve the goal WS₂ crystals with the sulfurization of WO₃ and WCl₆ precursor at Ar atmosphere was tackled. In parallel the growth and hydrogen etching of graphene, on which WS₂ grows, was investigated. Finally, the direct growth of WS₂ crystals on transferred CVD grown graphene and h-BN film was challenged. The size of obtained WS₂ crystals on the CVD grown and graphene were small, around 5-7 μm.

1.7 Organization of the dissertation

This thesis contributes to the synthesis of large size WS₂ crystal using various precursors and substrates such as graphene, h-BN and SiO₂/Si and graphene synthesis by APCVD and their characterization.

Chapter 1 describes the general introduction of 2D layered materials including graphene h-BN and TMDCs, with regard to their properties, applications and physical and chemical synthesis methods.

Chapter 2 deals with the experimental set-up for synthesis WS₂ crystal, graphene and hexagonal boron nitride.

Chapter 3 is about the effect of WO₃ precursor and sulfurization process on WS₂ crystals sample were grown on SiO₂/Si substrate. Larger triangular crystals (~70 μm) were obtained by controlling the amount of WO₃ precursor to control the nucleation and growth sites. Pyramid-like few-layers stacked structure of WS₂ crystals were obtained from densely spread WO₃ powder.

Chapter 4 discusses the synthesis monolayer WS₂ crystals using tungsten halide precursor. WCl₆ is used as a precursor and SiO₂/Si is used as a substrate. Larger triangular monolayer crystals (~100μm) were obtained. Six pointed and 3 pointed star shaped and butterfly like structures were obtained because of mirror twin boundaries and cyclic twinning of boundaries.

In chapter 5, the synthesis of graphene and the effect of hydrogen etching were studied upon graphene crystals and continuous film. Highly anisotropic and fractal etching was demonstrated with the formation of hexagonal graphene hole, ribbon like structures and hexagonal-hexagonal stacking (stacking of three hexagonal layers) along with the snowflake dendritic crystals. This finding can be significant to understand the nucleation and growth of graphene crystals as well as their selective etching process to fabricate well-defined structures.

Chapter 6 discusses the synthesis of WS₂ crystals on transferred CVD grown graphene and h-BN. Triangular WS₂ crystal size around 2-7 μm were obtained. Vertically aligned WS₂ crystals were observed on graphene.

Chapter 7 Summarizes the whole thesis and future prospects.

1.8 References

- [1] Geim, A. K.; Novoselov, K. S. *Nature Materials* 2007, 6, 183-191.
- [2] W. H. Balmain, *Philos. Mag. Series 3*, 1842, 21, 270–277.
- [3] W. H. Balmain, *J. Prakt. Chem.*, 1842, 27, 422–430.
- [4] Ishii, T.; Sato, T.; Sekikawa, Y.; Iwata, M. 1981, 52, 285-289.
- [5] Paine, R. T.; Narula, C. K. *Chemical Reviews* 1990, 90, 73-91
- [6] Wang, Q. H.; Kalantar-Zadeh, K.; Kis, A.; Coleman, J. N.; Strano, M. S. *Nat. Nanotechnol.* 2012, 7, 699–712.
- [7] Chhowalla, M.; Shin, H. S.; Eda, G.; Li, L.-J.; Loh, K. P.; Zhang, H. *The Chemistry of Nat. Chem.* 2013, 5, 263–275.
- [8] Radisavljevic, B.; Radenovic, A.; Brivio, J.; Giacometti, V.; Kis, A. *Nat. Nanotechnol.* 2011, 6, 147–150.
- [9] Ovchinnikov, D.; Allain, A.; Huang, Y.-S.; Dumcenco, D.; Kis, A. *ACS Nano* 2014, 8, 8174–8181
- [10] Zhao, W.; Ghorannevis, Z.; Chu, L.; Toh, M.; Kloc, C.; Tan, P.-H.; Eda, G. *ACS Nano* 2012, 7, 791–797.
- [11] Mak, K. F.; Lee, C.; Hone, J.; Shan, J.; Heinz, T. F. *Phys. Rev. Lett.* 2010, 105, 136805.
- [12] Splendiani, A.; Sun, L.; Zhang, Y.; Li, T.; Kim, J.; Chim, C.-Y.; Galli, G.; Wang, F. *Emerging Nano Lett.* 2010, 10, 1271–1275.
- [13] Eda, G.; Yamaguchi, H.; Voiry, D.; Fujita, T.; Chen, M.; Chhowalla, M. *Nano Lett.* 2011, 11, 5111–5116.
- [14] Zhang, Y. J.; Oka, T.; Suzuki, R.; Ye, J. T.; Iwasa, Y. 2014, 344, 725–728.
- [15] Zeng, H.; Dai, J.; Yao, W.; Xiao, D.; Cui, X. *Nat. Nanotechnol.* 2012, 7, 490–493.
- [16] Mak, K. F.; He, K.; Shan, J.; Heinz, T. F. *Nat. Nanotechnol.* 2012, 7, 494–498.

- [17] Huang, X.; Zeng, Z.; Zhang, H. *Chem. Soc. Rev.* 2013, 42, 1934–1946
- [18]. Schutte, W. J.; Deboer, J. L.; Jellinek, F. J. *Solid State Chem.* 1987, 70, 207–209
- [19] Radisavljevic, B.; Radenovic, A.; Brivio, J.; Giacometti, V.; Kis, A. *Nanotechnol.* 2011, 6, 147–150
- [20] Tenne, R.; Margulis, L.; Genut, M. E. A.; Hodes, G. *Nature* 1992, 360, 444-446.
- [21] Zak, A.; Feldman, Y.; Lyakhovitskaya, V.; Leitun, G.; Popovitz-Biro, R.; Wachtel, E.; Cohen, H.; Reich, S.; Tenne, R. *Journal of the American Chemical Society* 2002, 124, 4747-4758.
- [22] Zhu, Y. Q.; Sekine, T.; Li, Y. H.; Wang, W. X.; Fay, M. W.; Edwards, H.; Brown, P. D.; Fleischer, N.; Tenne, R. *Advanced Materials* 2005, 17, 1500- 1503.
- [23] Golberg, D.; Bando, Y.; Huang, Y.; Terao, T.; Mitome, M.; Tang, C.; Zhi, C. *ACS Nano* 2010, 4, 2979-2993.
- [24] Xiao, J.; Long, M.; Li, X.; Xu, H.; Huang, H.; Gao, Y. *Scientific Reports* 2014, 4.
- [25] Seifert, G.; Terrones, H.; Terrones, M.; Jungnickel, G.; Frauenheim, T. *Physical Review Letters* 2000, 85, 146-149.
- [26] Smith, R. J.; King, P. J.; Lotya, M.; Wirtz, C.; Khan, U.; De, S.; O'Neill, A.; Duesberg, G. S.; Grunlan, J. C.; Moriarty, G.; Chen, J.; Wang, J.; Minett, I.; Nicolosi, V.; Coleman, J. N. *Advanced Materials* 2011, 23, 3944..
- [27] Novoselov, K. S.; Jiang, D.; Schedin, F.; Booth, T. J.; Khotkevich, V. V.; Morozov, S. V.; Geim, A. K. *Proceedings of the National Academy of Sciences of the United States of America* 2005, 102, 10451- 10453.
- [28] Lee, C.; Wei, X.; Kysar, J. W.; Hone, J. *Science* 2008, 321, 385-388.
- [29] Balandin, A. A.; Ghosh, S.; Bao, W.; Calizo, I.; Teweldebrhan, D.; Miao, F.; Lau, C. N. *Nano Letters* 2008, 8, 902-907.

- [30] Ho, C. Y.; Powell, R. W.; Liley, P. E. *Journal of Physical and Chemical Reference Data* 2009, 1, 279-421.
- [31] Nika, D. L.; Ghosh, S.; Pokatilov, E. P.; Balandin, A. A. *Applied Physics Letters* 2009, 94 203103.
- [32] Ghosh, S.; Calizo, I.; Teweldebrhan, D.; Pokatilov, E. P.; Nika, D. L.; Balandin, A. A.; Bao, W.; Miao, F.; Lau, C. N. *Applied Physics Letters* 2008, 92, 151911-151913.
- [33] Du, X.; Skachko, I.; Barker, A.; Andrei, E. Y. *Nature nanotechnology* 2008, 3, 491-495.
- [34] Meyer, J. C.; Geim, A. K.; Katsnelson, M. I.; Novoselov, K. S.; Booth, T. J.; Roth, S. *Nature* 2007, 446, 60-63.
- [35] Lin, Y.; Williams, T. V.; Connell, J. W. *Journal of Physical Chemistry Letters* 2010, 1, 277-283.
- [36] Rosentsveig, R.; Margolin, A.; Feldman, Y.; Popovitz-Biro, R.; Tenne, R. *Applied Physics A* 2002, 74, 367-369.
- [37] Haberecht, R. R.; Patterson, R. J.; Humphries, R. D. *Annual Report* 1964, 50.
- [38] Lin, Y.; Connell, J. W. *Nanoscale* 2012, 4, 6908-6939.
- [39] Zhu, H.; Li, Y.; Fang, Z.; Xu, J.; Cao, F.; Wan, J.; Preston, C.; Yang, B.; Hu, L. *ACS Nano* 2014, 8.4, 3606-3613.
- [40] Wang, X.; Pakdel, A.; Zhang, J.; Weng, Q.; Zhai, T.; Zhi, C.; Golberg, D.; Bando, Y. *Nanoscale Research Letters* 2012, 7, 1-7.
- [41] Li, L. H.; Cervenka, J.; Watanabe, K.; Taniguchi, T.; Chen, Y. *ACS Nano* 2014, 10.12, 5049-5055.
- [42] Liu, Z.; Gong, Y.; Zhou, W.; Ma, L.; Yu, J.; Idrobo, J. C.; Jung, J.; MacDonald, A. H.; Vajtai, R.; Lou, J. *Nature Communications* 2013, 4.
- [43] Wang, Q. H.; Kalantar-Zadeh, K.; Kis, A.; Coleman, J. N.; Strano, M.S. *Nature*

- Nanotechnology 2012, 7, 699-712.
- [44] Kuc, A.; Zibouche, N.; Heine, T. *Physical Review B* 2011, 83, 245213.
- [45] Mak, K. F.; Lee, C.; Hone, J.; Shan, J.; Heinz, T. F. *Physical Review Letters* 2010, 105, 136805.
- [46] Splendiani, A.; Sun, L.; Zhang, Y.; Li, T.; Kim, J.; Chim, C.-Y.; Galli, G.; Wang, F. *Nano Letters* 2010, 10, 1271-1275.
- [47] Mak, K. F.; He, K.; Shan, J.; Heinz, T. F. *Nature Nanotechnology* 2012, 7, 494-498.
- [48] Aruchamy, A. Springer, 1992; Vol. 14.
- [49] Sandler, J.; Shaffer, M. S. P.; Prasse, T.; Bauhofer, W.; Schulte, K.; Windle, A. H. *Polymer* 1999, 40, 5967-5971.
- [50] Yu, W.; Xie, H.; Wang, X.; Wang, X. *Physics Letters A* 2011, 375, 1323-1328.
- [51] Kim, H.; Macosko, C. W. *Macromolecules* 2008, 41, 3317-3327.
- [52] Stankovich, S.; Dikin, D. A.; Dommett, G. H. B.; Kohlhaas, K. M.; Zimney, E. J.; Stach, E. A.; Piner, R. D.; Nguyen, S. T.; Ruoff, R. S. *Nature* 2006, 442, 282-286.
- [53] Verdejo, R.; Barroso-Bujans, F.; Rodriguez-Perez, M. A.; de Saja, J. A.; Lopez-Manchado, M. A. *Journal of Materials Chemistry* 2008, 18, 2221-2226.
- [54] Eda, G.; Chhowalla, M. *Nano Letters* 2009, 9, 814-818.
- [55] Bourzac, K. *Technology Review* 2008, 321.5887, 385-388.
- [56] Bourzac, K. *Technology Review* 2009, 490.7419, 192-200.
- [57] Wang, X.; Zhi, L.; Muellen, K. *Nano Letters* 2008, 8, 323-327.
- [58] Chatterjee, S.; Nueesch, F. A.; Chu, B. T. T. *Nanotechnology* 2011, 22.
- [59] Bao, Q.; Zhang, H.; Yang, J.-x.; Wang, S.; Tong, D. Y.; Jose, R.; Ramakrishna, S.; Lim, C. T.; Loh, K. P. *Advanced Functional Materials* 2010, 20.
- [60] Gong, L.; Young, R. J.; Kinloch, I. A.; Riaz, I.; Jalil, R.; Novoselov, K.S. *ACS Nano*

- 2012, 6, 2086-2095.
- [61] Jiang, L.; Shen, X.-P.; Wu, J.-L.; Shen, K.-C. *Journal of Applied Polymer Science* 2010, 118, 275-279.
- [62] Kim, H.; Macosko, C. W. *Polymer* 2009, 50.
- [63] Rafiee, M. A.; Rafiee, J.; Wang, Z.; Song, H.; Yu, Z.-Z.; Koratkar, N. *ACS Nano* 2009, 3, 3884-3890.
- [64] Xu, Y.; Chung, D. D. L. *Composite Interfaces* 2000, 7, 243-256.
- [65] Lu, P.; Wu, X.; Guo, W.; Zeng, X. C. *Physical Chemistry Chemical Physics* 2012, 14, 13035-13040.
- [66] Radisavljevic, B.; Radenovic, A.; Brivio, J.; Giacometti, V.; Kis, A. *Nature Nanotechnology* 2011, 6, 147-150.
- [67] Banerjee, S.; Richardson, W.; Coleman, J.; Chatterjee, A. *IEEE Electron Device Letters* 1987, 8, 347-349.
- [68] Roy, P.; Srivastava, S. K. *Thin Solid Films* 2006, 496, 293-298.
- [69] Srivastava, S. K.; Avasthi, B. N. *Journal of Materials Science* 1985, 20, 3801-3815.
- [70] Srivastava, S. K. *Materials Research Bulletin* 1991, 26, 631-639.
- [71] Hulliger, F. Springer, 1968; 83-229.
- [72] Wilson, J. A.; Yoffe, A. D. *Advances in Physics* 1969, 18, 193-335.
- [73] Imanishi, N.; Kanamura, K.; Takehara, Z. I. *Journal of the Electrochemical Society* 1992, 139, 2082-2087.
- [74] Dominko, R.; Arčon, D.; Mrzel, A.; Zorko, A.; Cevc, P.; Venturini, P.; Gaberscek, M.; Remskar, M.; Mihailovic, D. *Advanced Materials* 2002, 14, 1531-1534.
- [75] Zhu, Y. Q.; Sekine, T.; Li, Y. H.; Fay, M. W.; Zhao, Y. M.; Patrick Poa, C. H.; Wang, W. X.; Roe, M. J.; Brown, P. D.; Fleischer, N. *Journal of the American Chemical Society*

- 2005, 127, 16263-16272.
- [76] Chen, J.; Kuriyama, N.; Yuan, H.; Takeshita, H. T.; Sakai, T. *Journal of the American Chemical Society* 2001, 123, 11813-11814
- [77] K. S. Novoselov, A. K. Geim, S. V. Morozov, D. Jiang, Y. Zhang, S. V. Dubonos, I. V. Grigorieva and A. A. Firsov, *Science*, 2004, 306, 666–669.
- [78] K. S. Novoselov, D. Jiang, F. Schedin, T. J. Booth, V. V. Khotkevich, S. V. Morozov and A. K. Geim, *Proc. Natl. Acad. Sci. U. S. A.*, 2005, 102, 10451–10453.
- [79] M. S. Dresselhaus and P. T. Araujo, *ACS Nano*, 2010, 4, 6297–6302
- [80] Y. Hernandez, V. Nicolosi, M. Lotya, F. M. Blighe, Z. Sun, S. De, I. T. McGovern, B. Holland, M. Byrne, Y. K. Gun'Ko, J. J. Boland, P. Niraj, G. Duesberg, S. Krishnamurthy, R. Goodhue, J. Hutchison, V. Scardaci, A. C. Ferrari and J. N. Coleman, *Nat. Nanotechnol.*, 2008, 3, 563–568.
- [81] M. Eizenberg and J. Blakely, *Surf. Sci.*, 1979, 82, 228–236.
- [82] J. Shelton, H. Patil and J. Blakely, *Surf. Sci.*, 1974, 43, 493– 520.
- [83] J. W. May, *Surf. Sci.*, 1969, 17, 267–270.
- [84] X. S. Li, W. W. Cai, J. H. An, S. Kim, J. Nah, D. X. Yang, R. Piner, A. Velamakanni, I. Jung, E. Tutuc, S. K. Banerjee, L. Colombo and R. S. Ruoff, *Science*, 2009, 324, 1312–1314
- [85] A. de Lodyguine, *US Patents*, 1897, US575002A.
- [86] R. Platz and S. Wagner, *Appl. Phys. Lett.*, 1998, 73, 1236–1238.
- [87] K. L. Choy, *Prog. Mater. Sci.*, 2003, 48, 57–170.
- [88] K. S. Novoselov, A. K. Geim, S. V. Morozov, D. Jiang, Y. Zhang, S. V. Dubonos, I. V. Grigorieva and A. A. Firsov, *Science*, 2004, 306, 666–669.
- [89] E. S. Penev, V. I. Artyukhov, F. Ding and B. I. Yakobson, *Adv. Mater.*, 2012, 24, 4956–4976.
- [90] X. Zhang, H. Li and F. Ding, *Adv. Mater.*, 2014, 26, 5488–5495.

- [91] I. Vlasiouk, M. Regmi, P. Fulvio, S. Dai, P. Datskos, G. Eres and S. Smirnov, *ACS Nano*, 2011, 5, 6069–6076.
- [92] P. R. Somani, S. P. Somani and M. Umeno, *Chem. Phys. Lett.*, 2006, 430, 56–59.
- [93] W. Feng, S. Lei, Q. Li and A. Zhao, *J. Phys. Chem. C*, 2011, 115, 24858–24864.
- [94] T. Gao, S. Xie, Y. Gao, M. Liu, Y. Chen, Y. Zhang and Z. Liu, *ACS Nano*, 2011, 5, 9194–9201.
- [95] Y. Gong, X. Zhang, G. Liu, L. Wu, X. Geng, M. Long, X. Cao, Y. Guo, W. Li, J. Xu, M. Sun L. Lu and L. Liu, *Adv. Funct. Mater.*, 2012, 22, 3153–3159.
- [96] Y. Shi, C. Hamsen, X. Jia, K. K. Kim, A. Reina, M. Hofmann, A. L. Hsu, K. Zhang, H. Li, Z.-Y. Juang, M. S. Dresselhaus, L.-J. Li and J. Kong, *Nano Lett.*, 2010, 10, 4134–4139.
- [97] L. Song, L. Ci, H. Lu, P. B. Sorokin, C. Jin, J. Ni, A. G. Kvashnin, D. G. Kvashnin, J. Lou, B. I. Yakobson and P. M. Ajayan, *Nano Lett.*, 2010, 10, 3209–3215.
- [98] W. Hofmann, *J. Mater. Sci.*, 1988, 23, 3981–3986.
- [99] K.-K. Liu, W. Zhang, Y.-H. Lee, Y.-C. Lin, M.-T. Chang, C.-Y. Su, C.-S. Chang, H. Li, Y. Shi, H. Zhang, C.-S. Lai and L.-J. Li, *Nano Lett.*, 2012, 12, 1538–1544.
- [100] Y. Zhan, Z. Liu, S. Najmaei, P. M. Ajayan and J. Lou, *Small*, 2012, 8, 966–971.
- [101] Y. H. Lee, X. Q. Zhang, W. Zhang, M. T. Chang, C. T. Lin, K. D. Chang, Y. C. Yu, J. T. Wang, C. S. Chang, L. J. Li and T. W. Lin, *Adv. Mater.*, 2012, 24, 2320–2325.
- [102] K. M. McCreary, A. T. Hanbicki, J. T. Robinson, E. Cobas, J. C. Culbertson, A. L. Friedman, G. G. Jernigan and B. T. Jonker, *Adv. Funct. Mater.* 2014, 24, 6449–6454
- [103] Y. Zhang, Y. Zhang, Q. Ji, J. Ju, H. Yuan, J. Shi, T. Gao, D. Ma, M. Liu, Y. Chen, X. Song, H. Y. Hwang, Y. Cui and Z. Liu, *ACS Nano*, 2013, 7, 8963–8971.
- [104] Y. Rong, Y. Fan, A. Leen Koh, A. W. Robertson, K. He, S. Wang, H. Tan, R. Sinclair and J. H.

- Warner, *Nanoscale*, 2014, 6, 12096–12103.
- [105] M. Bernardi, M. Palumbo and J. C. Grossman, *Nano Lett.*, 2013, 13, 3664–3670.
- [106] Min Yi and Zhigang Shen A review on mechanical exfoliation for the scalable production of graphene *J. Mater. Chem. A*, 2015, 3, 11700
- [107] Amir Pakdel, Yoshio Bando and Dmitri Golberg Nano boron nitride flatland, *Chem. Soc. Rev.*, 2014, 43, 934

CHAPTER 2

Experimental

2.1 WS₂ Synthesis

There are several methods to synthesize WS₂ crystals such as (top-down routes) mechanical exfoliation, liquid exfoliation and chemical exfoliation or (bottom-up process) chemical vapor deposition. In this thesis work we have used atmospheric pressure chemical vapor deposition method. It is one of the promising method to synthesize WS₂ because of its scalability and wide tunability in growth parameters such as pressure, temperature and source. The aims of the CVD growth of WS₂ are to grow few- and single- layer sheets, and to prepare single crystal WS₂ atomic layers. In a more systematic approach, different strategies for supplying metal sources are adopted before sulfurization in CVD: (i) tungsten or solid tungsten oxide thin-film with various thicknesses and (ii) vaporized solid precursors. Large-area WS₂ thin- film is obtained by a simple sulfurization of thin tungsten film or thin tungsten oxide film deposited by various methods including e-beam evaporation, magnetron sputtering, and atomic layer deposition (iii) tungsten oxides and solid sulfur sources are vaporized simultaneously on the insulating substrate during CVD process

2.1.1 Synthesis of WS₂ crystals using tungsten oxides:

We have used two individual temperature controlled furnace. One is high temperature and another one is low temperature furnace.

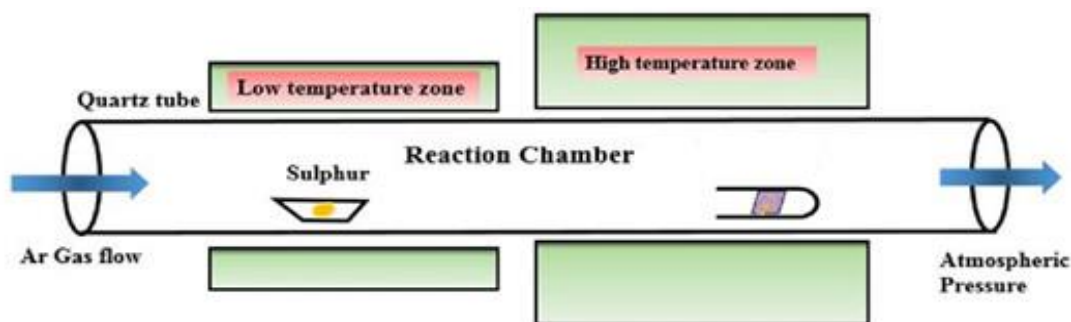


Figure 2-1 Schematic diagram of experimental set up for WS₂ crystal synthesis

Synthesis of WS₂ triangular crystals is investigated by one step sulfurization of WO₃ powder by an APCVD technique. WO₃ powder was spread on 100 nm SiO₂ coated Si substrate and sulfurized in Ar atmosphere. The quantity of WO₃ powder was varied (2 and 10 mg) to explore the sulfurization process.

Sulfurization of WO_3 powder was carried out in a quartz tube using two individually controlled temperature zones. S powder was placed in the center of low temperature furnace and the WO_3 powder spread SiO_2/Si substrate, which was kept in the small ceramic tube and placed in the center of high temperature furnace. Subsequently, Ar gas was purged in the quartz tube for 5 min after which the high temperature furnace was started. As the temperature reached to $550\text{ }^\circ\text{C}$, the low temperature furnace was also started. S vapor was introduced with Ar flow rate of 80 sccm (standard cubic centimeter per minute). Now, the temperature of growth zone (SiO_2/Si substrate with WO_3 powder) was increased upto $750\text{ }^\circ\text{C}$. The ramping rate of growth zone was fixed as $3^\circ\text{C}/\text{min}$. The growth was carried out for 30 min at $750\text{ }^\circ\text{C}$ and subsequently furnace was cooled down to room temperature.

Synthesized materials were analyzed by optical microscopy, Raman spectroscopy and field-emission scanning electron microscopy (FE-SEM). Optical microscopy analysis were performed with the digital optical microscope VHX-500 in reflectance mode with a Moticam 2000 2.0 M pixel camera. Raman analysis was carried out using NRS 3300 laser Raman spectrometer with a laser excitation energy of 532.08 nm. FE-SEM studies were performed with JEOL JSM-7800F using lower electron detector (LED) with an accelerating voltage of 5kV

Experimental parameters for WS_2 crystals synthesis using WO_3

Expt	Amt. of WO_3 (mg)	Amt. of S (mg)	Growth Temp ($^\circ\text{C}$)	Growth Gas(sccm)	Growth time (min)	Growth substrate
WS_2	2 & 10	100	750 & 950	Ar/80	30	SiO_2/Si , Graphene & h-BN

Table 2-1. Experimental parameters of WS_2 crystal synthesis using WO_3

2.1.2 Synthesis of WS_2 crystals using tungsten chloride

Here, we investigate WS_2 crystal growth using a tungsten halide precursor coated on SiO_2/Si substrate. In the developed process, a 0.05M solution of WCl_6 was drop casted on the SiO_2/Si substrate, which was reduced and sulfurized in Ar atmosphere by the APCVD process. The growth of triangular, star-shaped, as well as dendritic monolayer WS_2 crystals on the substrate was observed; where triangular crystals were obtained with a lateral size of more than $100\text{ }\mu\text{m}$. The developed growth technique using drop casted WCl_6 solid precursor can be significant to obtain large single crystals on arbitrary substrates. Synthesis of WS_2 monolayer crystals of various geometries is achieved by one step sulfurization of WCl_6 solid precursor by the APCVD technique. In this technique, we prepared 0.1, 0.05 and 0.01M solution of WCl_6 powder in ethanol. Subsequently, the solution was drop casted on SiO_2/Si substrates

and dried. The SiO_2/Si substrates with WCl_6 precursor were loaded in the center of small diameter ceramic tube sealed at one-end and placed in the center of high temperature furnace. A boat with 200 mg of S powder was placed in the center of low temperature furnace. Experiments were performed at a reaction temperature of 750°C . Ar gas was purged in the quartz tube for 5 minutes prior to the high temperature furnace was started. After the temperature was reached to 750°C , the low temperature furnace was also started. S powder was mildly sublimated at 350°C and growth was carried out for 30 min in 80 sccm (standard cubic centimeter per minute) of Ar atmosphere. Finally, the furnace was cooled down to room temperature and samples were removed from the ceramic tube for analysis.

The synthesized materials were characterized by optical microscopy, FE-SEM, Raman Spectroscopy and atomic force microscopy (AFM). Optical microscopy analysis were performed with the digital optical microscope VHX-500 in reflectance mode with a Moticam 2000 2.0 Mpixel camera. Raman analysis was carried out using NRS 3300 laser Raman spectrometer. FE-SEM studies were performed with JEOL JSM-7800F using an accelerating voltage of 2 kV. AFM analysis were performed with a JSPM-5200 scanning probe microscope.

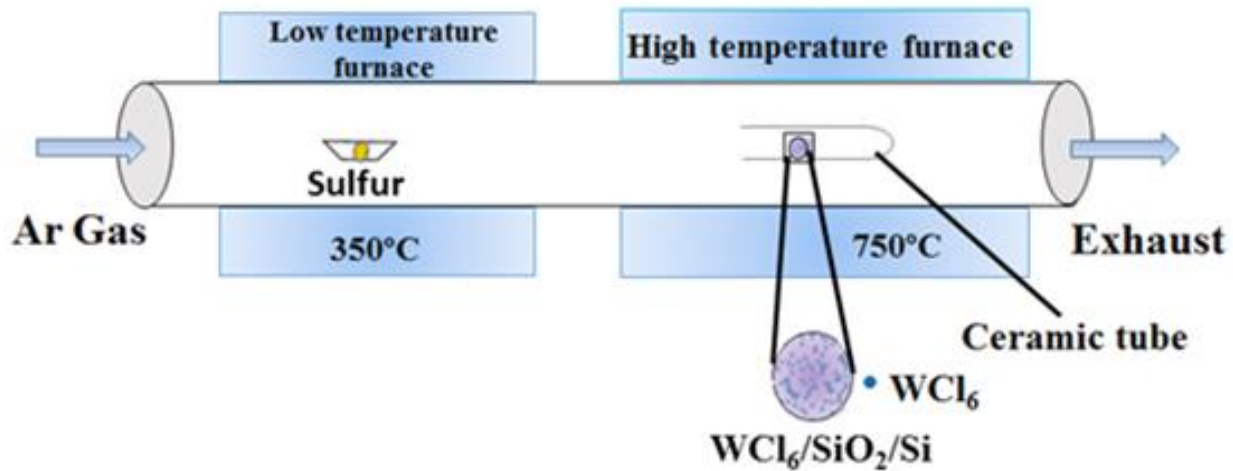


Figure 2-2. Schematic diagram of experimental set up for WS_2 crystal synthesis

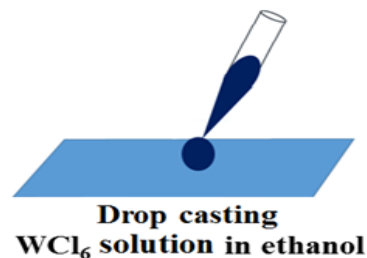


Figure 2-3. Schematic diagram of drop casted WCl_6 solution on SiO_2/Si substrate

Experimental parameters for WS₂ crystals synthesis using WCl₆

Experiment	Amount of WCl ₆ (0.05M)	Amount of Sulfur (mg)	Growth Temperature (°C)	Growth gas (sccm)	Growth time (min)
WS ₂	2 drop	200	750	80	30

Table 2-3. Experimental parameters of WS₂ crystal synthesis using WCl₆

2.2 Graphene synthesis

2.2.1 Graphene synthesis by APCVD

In this study, electro-polished Cu foil (thickness 20 μm , purity 99.98%, Nilaco) was used for graphene synthesis. Electro-polishing of Cu foil was carried out using a thick Cu plate (300 μm) as cathode. The electropolishing solution was composed of water (50 ml), ortho- Phosphoric acid (25 ml), ethanol (25 ml), isopropyl alcohol (5 ml), and urea (0.8 g). The Cu foil was placed into the solution, while it was supported by an alligator clip. AE-8135 my Power II 300 system as DC power source was used to supply constant voltage/ current, and a voltage in the range of 3.0–7.0 V was applied for 2 min. After electro polishing, the Cu foil was rinsed with deionized water and used for graphene synthesis. The experimental set up of graphene synthesis like as WS₂ crystal synthesis. We used camphor and polystyrene as solid source for graphene synthesis in an atmospheric pressure CVD. The Cu foil was annealed at 1055°C under H₂ gas flow of 100 sccm for 30 min. H₂ was reduced from 100 sccm to 2.5 sccm and Ar was introduced with the flow rate of 98 sccm for growth. Heating the low temperature zone camphor was evaporated and introduced in the CVD reactor. We annealed the graphene samples in Ar: H₂ gas mixture after growth was completed to explore the influence of H₂ in etching behavior.

2.2.2 Transfer of graphene

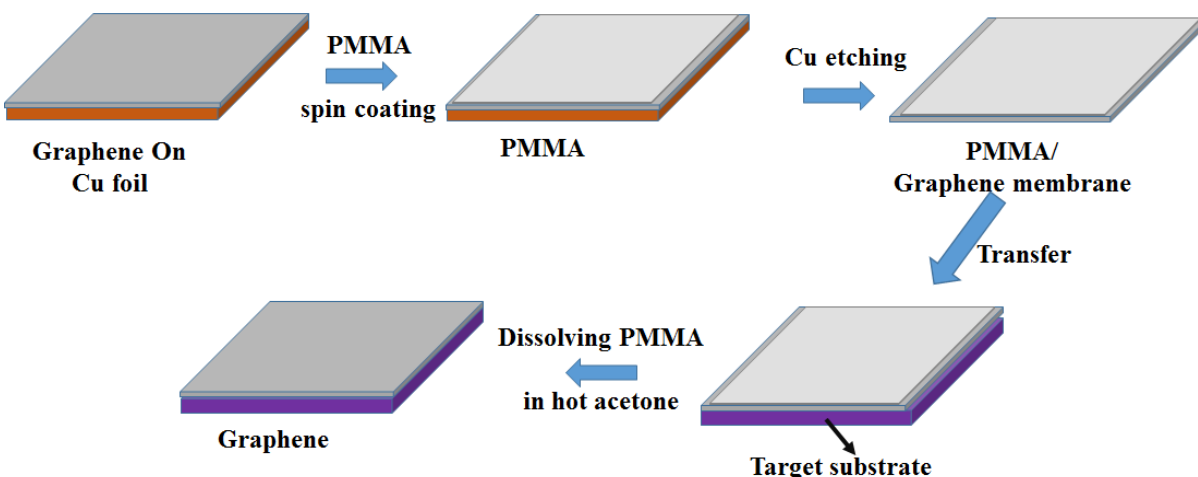


Figure 2-4 Schematic diagram of graphene transfer process on the substrate

Figure 2-4 is a schematic of the steps used to transfer graphene from copper foil to substrates using $\text{Fe}(\text{NO}_3)_2$ etching method. First, PMMA solution was spin coated on the surface of the graphene-Cu foils. The PMMA spin coated graphene-cu foil was soaked in $\text{Fe}(\text{NO}_3)_2$ for 15hrs. Once Cu etched completely, PMMA/ Graphene membrane was transferred on the SiO_2/Si substrate. Finally the PMMA from the graphene was dissolved in hot acetone. The transferred h-BN was used as a substrate for WS_2 growth. The experimental set up for WS_2 crystals synthesis on transferred graphene substrate as shown in the Table 2-1.

2.3 h-BN synthesis

2.3.1 h-BN synthesis by APCVD

In this work, electropolished cu foil was used as a substrate. The electropolishing solution of cu foil was made for h-BN synthesis like as we discussed in the graphene synthesis. We used Ammonia borane as solid source for h-BN synthesis in an APCVD. The Cu foil was annealed at 1020°C under H_2 gas flow of 100 sccm for 30 min. H_2 was reduced from 100 sccm to 2 sccm and Ar was introduced with the flow rate of 80 sccm for growth. Heating the low temperature zone, Ammonia borane was evaporated and introduced in the CVD reactor.

2.3.2 Transfer of h-BN

Transfer of as synthesized h-BN on the insulating SiO₂/Si substrate like as we discussed in Graphene transfer process. The transferred h-BN was used as a substrate for WS₂ growth. The experimental set up for WS₂ crystals synthesis on transferred h-BN substrate as shown in the Table 2-1

CHAPTER 3

Effect of WO₃ precursor and sulfurization process on WS₂ crystals growth by atmospheric pressure CVD

3.1 Introduction

The synthesis of graphene and h-BN crystals has brought tremendous excitement in nano-electronics and various other applications [1-5]. While, graphene does not possess a band gap and h-BN is insulating, many important applications need intermediate properties, i.e. semiconductors [6]. Monolayers of TMDCs have recently caught the attention as 2D semiconductor crystals [7-10]. These 2D layered materials are formed with strong in-plane covalent bonding of individual atomic layers and weak van der Waals interaction between two adjacent layers [11]. TMDC layers have opened up new opportunities for nano-electronic and optoelectronic device applications and it has bandgap i.e. around 1~2 eV can be more suitable for FETs application, as the on/off ratio of graphene device is significantly poor [6, 12-20]. Monolayer WS₂ with a direct band gap, coupled spin and valley physics and band structure tunability with strain has significant importance for nano-electronics and optoelectronics application [21-28]. In these prospects, growth of high quality WS₂ crystals can be the most key aspect for device integration.

Recently, synthesis of MoS₂ and WS₂ layered materials have been explored by several approach, such as, mechanical exfoliation, liquid exfoliation, and sulfurization of transition metal and metal oxides [29-31]. Significant efforts have been made to grow large WS₂ crystals by a CVD process. The CVD technique can be more advantageous to grow high-quality WS₂ sheet with wafer-scale uniformity. However, there are several challenges to grow high quality WS₂ layers with the possibility of forming nanoparticles and few-layers structure, thereby limiting the growth of large-area crystals.

Synthesis of WS₂ crystal has been investigated by sulfurization of WO₃ at an elevated temperature. The possibility of large crystal growth has been explored using WO₃ dispersed powder on SiO₂/Si substrate. In the growth process, the quantity of dispersed powder, growth temperature and sulfurization significantly affect the lateral growth of an individual crystal. Here, we demonstrate the influence of various parameters in the APCVD process to achieve growth of high quality WS₂ crystals.

3.2. Materials and methods

As explained in the chapter 2 section 2.1.1 (A)

3.3 Results and Discussions

Optical microscopy study

Figure 3-1(a) shows an optical microscope image of a large WS₂ crystal nucleated from the WO₃ powder on the SiO₂/Si substrate. The crystal nucleated from a cluster of WO₃ powder with reduction and sulfurization process. The lateral growth of a large WS₂ crystal enhance with continuous supply of the S vapor, thereby obtaining a 70 μm large crystal. Figure 3-1 (b) shows an optical microscope image of small triangular mono and multilayer WS₂ crystals which result of more amount of WO₃ powder spread on the SiO₂/Si substrate.

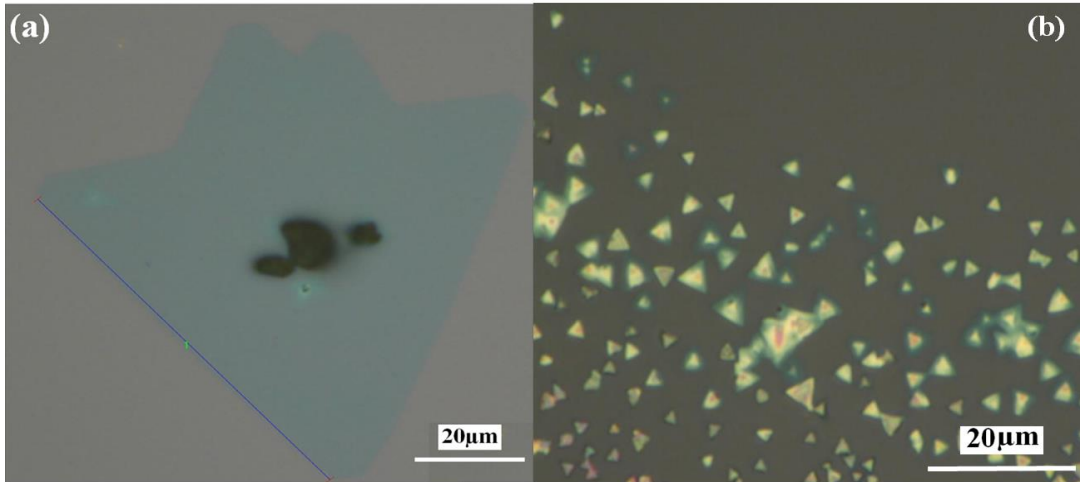


Figure 3-1 Optical microscopy images of synthesized WS_2 crystals on SiO_2/Si substrate with sulfurization of the densely spread (a) 2mg WO_3 powder (b) 10mg WO_3 powder.

FE-SEM Study

The growth of individual crystal with sulfurization of WO_3 powder on a SiO_2/Si substrate is investigated by varying the growth temperature. Figure 3-2(a) shows formation of WS_2 crystals on the insulating substrate with sulfurization of the densely spread WO_3 powder at 750 °C. Growths of thicker triangular and star-shaped crystals are obtained. While, some of the places thinner crystals are observed. Now, elevating the growth temperature to 950 °C, we observed formation of small triangular crystals overlapped each other to form densely packed structures. However, we also observed formation of very small monolayer crystals as indicated by the arrow marks in figure 3-2 (b). These results suggest that the thicker WS_2 crystals can be grown with a wide temperature range without affecting the few-layer structures. Figure 3-3(a) shows FE-SEM images of small triangular WS_2 crystals grown on the SiO_2/Si substrate at the growth temperature of 750 °C. The images clearly show that the top

layers grown with a pyramid structure, where the bottom monolayer is with largest lateral size. The formation of pyramid like structure of few-layer WS_2 crystals is an interesting prospect to achieve controllable synthesis of monolayer WS_2 . Figure 3-3 (b) shows FE-SEM images of much larger WS_2 crystal. In this case we are able to grow larger crystals by spreading less amount of WO_3 powder on the substrate to reduce the nucleation site.

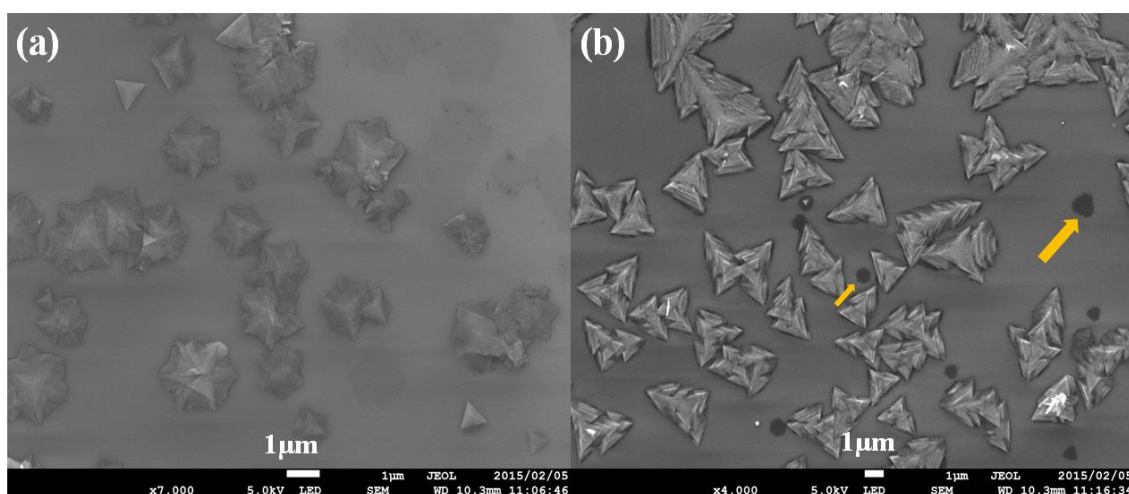


Figure 3-2 FE-SEM images of synthesized WS_2 crystals on SiO_2/Si substrate with sulfurization of the densely spread WO_3 powder at (a), 750 °C and (b) 950 °C.

We introduce the S vapor at a temperature around 550 °C, as the growth temperature was kept fixed at 750 °C similar to the previous conditions. The gas mixture and flow rate are other key aspects to control the S exposure during the WS_2 growth process. The S flow was controlled by Ar gas (80 sccm), such that an effective reaction can occur with the reduction of WO_3 powder. In this process, we have obtained more than 30 μm large triangular WS_2 crystals.

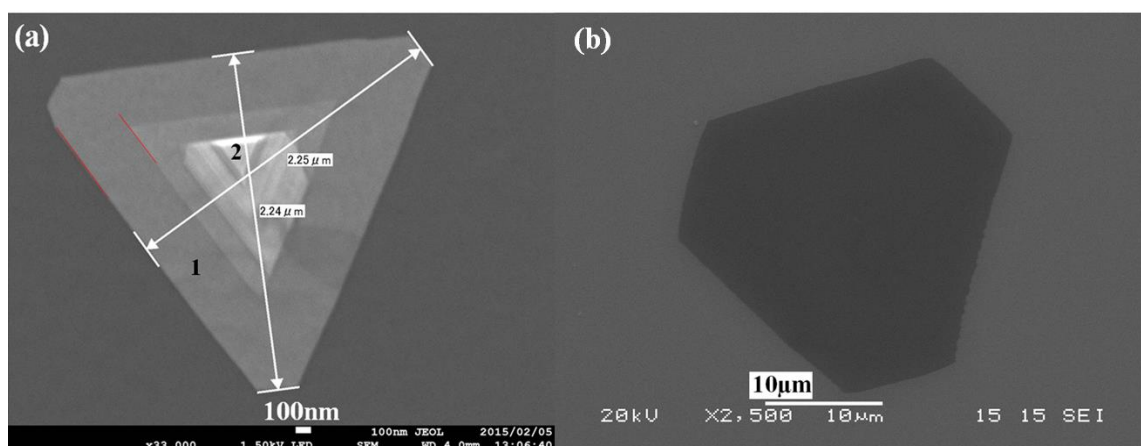


Figure 3-3(a) FE-SEM image of triangular WS₂ crystals on SiO₂/Si substrate where the layers are stacked to form a pyramid-like structure. (b) Much larger triangular WS₂ crystals.

Raman Spectroscopy Study

Figure 3-4 (a) shows a Raman spectra of the thicker WS₂ crystal, presenting the plane vibrational (E_{2g}^1) and out of-plane vibrational (A_{1g}) mode at ~ 348.8 and ~ 419.8 cm^{-1} , respectively [31]. The frequency differences of the E_{2g}^1 and A_{1g} mode is around 71 cm^{-1} , where the two peaks intensity ratio (A_{1g}/E_{2g}^1) is around 0.59. The high intensity of the A_{1g} peak confirmed the few layer structure of the crystals. Figure 3-4 (b) shows Raman spectra of the synthesized crystals, presenting the E_{2g}^1 and A_{1g} mode peaks at ~ 348.8 and ~ 419.8 cm^{-1} , respectively. The intensity ratio of the peaks of A_{1g} and E_{2g}^1 (A_{1g}/E_{2g}^1) is around 0.18, which is corresponding to monolayer WS₂ crystal. The Raman study confirms almost similar quality of WS₂ obtained at 750 and 950°C.

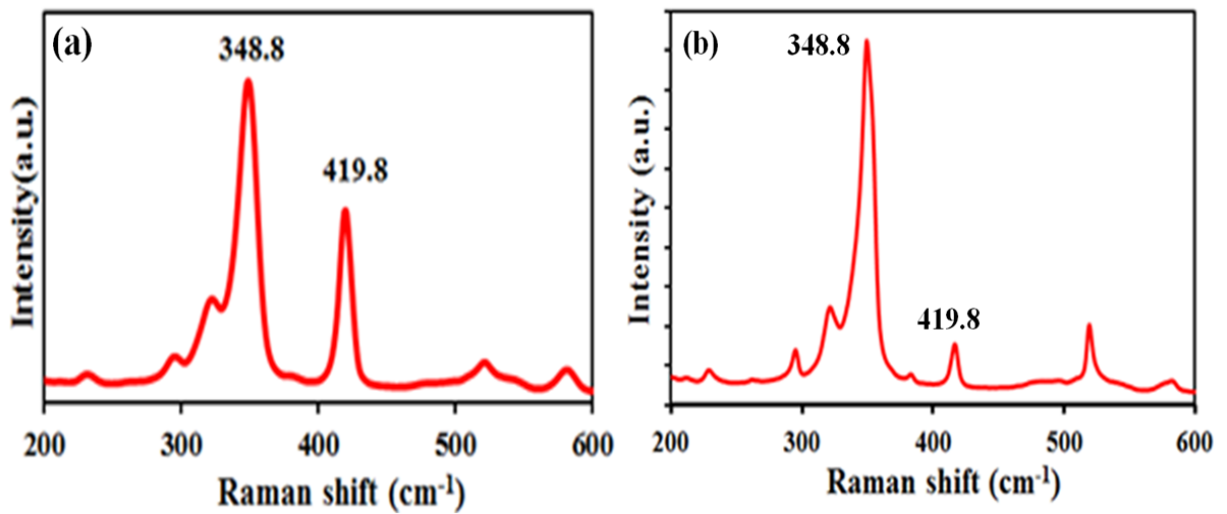


Figure 3-4(a) Raman spectra of the WS₂ crystal, presenting the plane vibrational (E¹_{2g}) and out-of-plane vibrational (A_{1g}) mode at ~348.8 and ~419.8 cm⁻¹.(b) Raman spectra of the synthesized crystals, presenting the E¹_{2g} and A_{1g} mode peaks at ~348.8 and ~419.8 cm⁻¹.

We have carried out Raman studies at various points to identify the WS₂ crystal layers number. Figure 3-5(a) shows a Raman spectra of the WS₂ crystal at position 1 of SEM image (figure 3-3(a)). The peaks for E¹_{2g} and A_{1g} mode are observed at ~348.8 and ~419.8 cm⁻¹, respectively. The intensity ratio of the peaks of A_{1g} and E¹_{2g} (A_{1g}/E¹_{2g}) is around 0.23. The significant reduction in the intensity of A_{1g} peak than that of the E¹_{2g} peak as shown in the inset of the figure 3-5(a), confirm a monolayer WS₂. Similarly, figure 3-5(b) shows Raman spectra of the WS₂ crystal at position 2 of SEM image (at the top of the pyramid structure). The peaks for E¹_{2g} and A_{1g} mode are observed at ~348.8 and ~419.8 cm⁻¹, respectively. In this position, we observed higher intense A_{1g} peak, corresponding to the few-layer structure. In this case we observed that the WO₃ spread on the SiO₂/Si substrate and subsequent sulfurization process significantly influence the crystals growth. The nucleation of such crystals is observed near the cluster of WO₃ powder spread on the substrate.

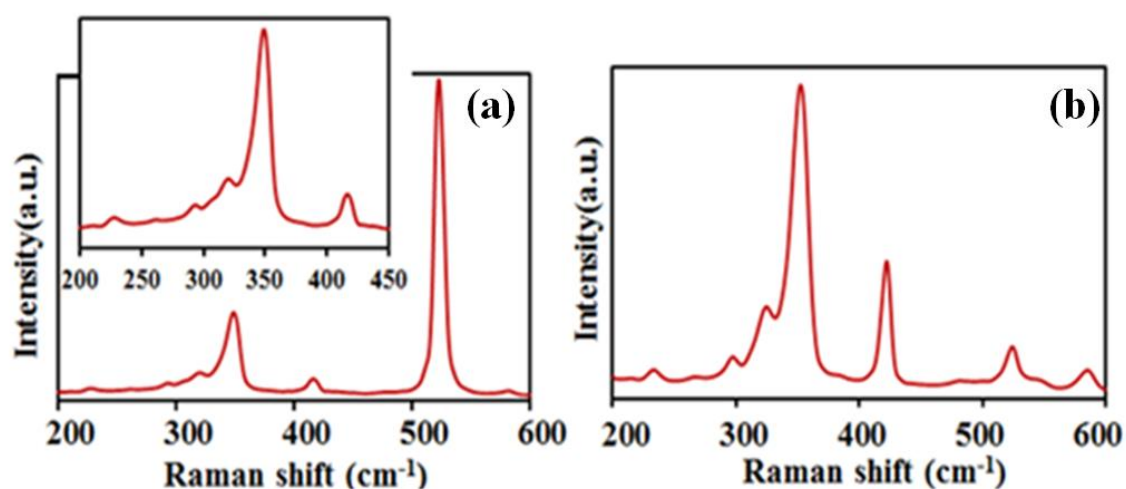


Figure 3-5 (a) and (b) Raman spectra of the WS₂ crystal at two different positions of (1 and 2) of figure 3-3(a)

Figure 3-6(a) shows Raman spectra at the edge of the WS₂ crystal, presenting the E_{2g}¹ and A_{1g} mode peaks at ~363.8 and ~433 cm⁻¹, respectively. The intensity ratio of the A_{1g} and E_{2g}¹ peaks (A_{1g}/E_{2g}¹) is around 0.27, which is almost same as that of the monolayer of pyramid structure WS₂ crystal. Figure 3-6(d) shows Raman spectra at the middle part of the crystal. We observed two splitted peaks at 715 and 813 cm⁻¹, corresponding to O-W-O stretching peaks. These results clearly suggest that the lateral growth of WS₂ crystal occurred from the center with the sulfurization. Thus, the additional layers of pyramid structures grow with further sulfurization of the WO₃ powder at the center.

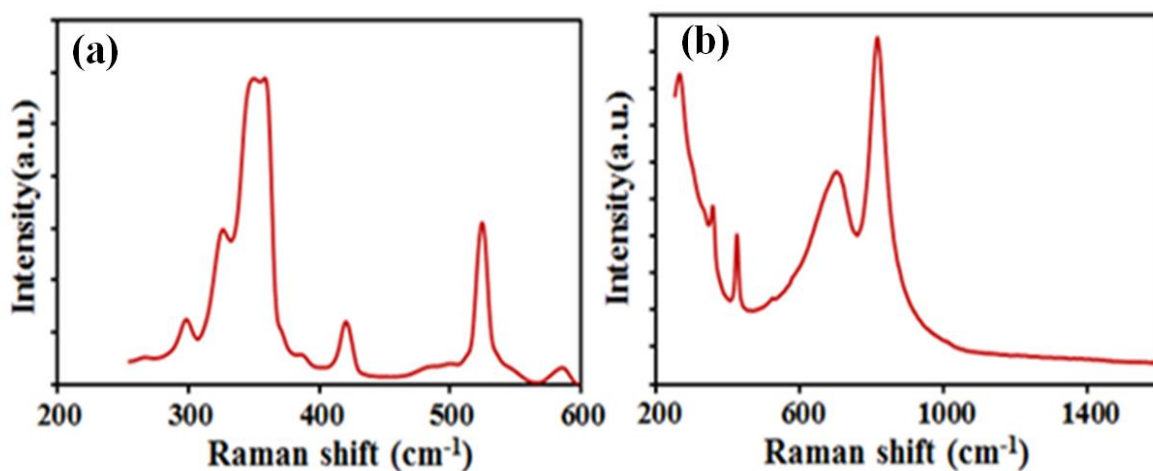


Figure 3-6 Raman spectra at the (a) edge, and (b) center part of the figure 3-1 (a)

3.4. Conclusions

We have revealed the effect of sulfurization process and quantity of WO_3 precursor on WS_2 crystals growth in the APCVD technique. The quantity of WO_3 precursor spread over SiO_2/Si substrate significantly influenced the nucleation density and layer numbers of triangular-shaped WS_2 crystals. Pyramid-like few-layers stacked structure of WS_2 crystals were obtained from densely spread WO_3 powder. Larger triangular crystals ($\sim 70 \mu\text{m}$) are obtained by reducing the amount of WO_3 precursor to control the nucleation and growth sites. At the same time, the sulfurization of WO_3 with introduction of S vapor was critical to obtain larger WS_2 crystals. Controlling the amount of WO_3 precursor and rate of S introduction in the high temperature CVD zone, large monolayer WS_2 crystals can be grown. This finding can be significant to understand WS_2 crystals growth by the CVD process at atmospheric pressure and thereby realizing synthesis of larger single crystals.

3.5 References

- [1] Novoselov KS, Jiang D, Schedin F, Booth TJ, Khotkevich VV, Morozov SV, et al. Proc Natl Acad Sci 2005;102:10451-3.
- [2] Geim AK, Novoselov KS. Nat Mater 2007; 6: 183-191.

- [3] Jin CH, Lin F, Suenaga K, Iijima S. *Phys Rev Lett* 2009; 102: 195505.
- [4] Britnell L, Gorbachev RV, Jalil R, Belle BD, Schedin F, Mishchenko A et al. *Science* 2012; 335: 947-50.
- [5] Dean CR, Young AF, Meric I, Lee C, Wang L, Sorgenfrei S, et al. *Nature Nanotechnol* 2010; 5: 722-6.
- [6] Radisavljevic B, Radenovic A, Brivio J, Giacometti V, Kis A. *Nature Nanotechnol* 2011; 6: 147-50
- [7] Splendiani, A, Sun L, Zhang Y, Li T, Kim J, Chim C-Y, et al. *Nano Lett* 2010; 10: 1271-75.
- [8] Ma Y, Dai Y, Guo M, Niu C, Lu J, Huang B, *Phys Chem Chem Phys* 2011; 13: 15546-53.
- [9] Wang QH, Kalantar-Zadeh K, Kis A, Coleman JN, Strano MS, *Nature Nanotechnol* 2012; 7: 699-712.
- [10] Jung Y, Shen J, Sun Y, Cha JJ, *ACS Nano* 2014; 8: 9550-57
- [11] Mas-Balleste R, Gomez-Navarro C, Gomez-Herrero J, Zamora F, *Nanoscale* 2011;3: 20-30.
- [12] Gao G, Gao W, Cannuccia E, Tijerina JT, Balicas L, Mathkar A, et al. *Nano Lett* 2012; 12: 3518-25.
- [13] Gutiérrez HR, Perea-López N, Elías AL, Berkdemir A, Wang B, Lv R, et al. *Nano Lett* 2013;13: 3447-54.
- [14] Shinde SM, Kalita G, Tanemura M, *J Appl Phys* 2014; 116: 214306.
- [15] Eda G, Yamaguchi H, Voiry D, Fujita T, Chen M, Chhowalla M, *Nano Lett* 2011; 11: 5111-16.
- [16] Zhao W, Ghorannevis Z, Chu L, Toh M, Kloc C, Tan P, et al. *ACS Nano* 2013;

7: 791-97.

- [17] Mak KF, Lee C, Hone J, Shan J, Heinz TF, Phys. Rev. Lett. 105, 136805 (2010).
- [18] Coleman N, Lotya M, O'Neill A, Bergin S, King P, Khan U, et al. Science 2011; 331: 568-71.
- [19] Zhang Y, Ye J, Matsushashi Y, Iwasa Y, Nano Lett 2012; 12: 1136-40.
- [20] Sie EJ, McIver JW, Lee YH, Fu L, Kong J, Gedik N. Nature Mater 2015; 14: 29094.
- [21] Xiao D, Liu GB, Feng W, Xu X, Yao W, Phys Rev Lett 2012;108: 196802.
- [22] Cao T, Wang G, Han W, Ye H, Zhu C, Shi J, et al. Nature Commun 2012; 3: 887.
- [23] Zhao YH, Yang F, Wang J, Guo H, Ji W, Sci Rep 2015; 5: 8356.
- [24] Roy K, Padmanabhan M, Goswami S, Sai TP, Ramalingam G, Raghavan S, et al. Nat Nanotechnol 2013; 8: 826-30
- [25] Cong C, Shang J, Wu X, Cao B, Peimyoo N, Qiu C, et al. Adv Opt Mater 2014; 2: 131-36.
- [26] Cunningham G, Hanlon D, McEvoy N, Duesberg GS, Coleman JN, Nanoscale 2015; 7: 198-208.
- [27] Gong Y, Lin J, Wang X, Shi G, Lei S, Lin Z, et al. Nature Mater 2014; 13: 113542.
- [28] Coleman JN, Lotya M, O'Neill A, Bergin SD, King PJ, Khan U, et al. Science 2011; 331: 568-71
- [29] Song J, Park J, Lee W, Choi T, Jung H, Lee CW, et al. ACS Nano 2013; 7: 11333-40.
- [30] Najmaei S, Liu Z, Zhou W, Zou X, Shi G, Lei S, et al. Nat Mater 2013; 12: 754-59.
- [31] Elias AL, Perea-Lopez N, Castro-Beltran A, Berkdemir A, Lv R, Feng S, et al. ACS Nano 2013; 7: 5235-42.

CHAPTER 4

An effective approach to synthesize monolayer tungsten disulphide crystals using tungsten halide

4.1 Introduction

TMDCs based layered materials (MoS_2 , WS_2 etc.) have attracted significant interest as 2D semiconductors with a direct band gap [1-3]. There is strong in-plane covalent bonding of individual atomic layers and weak van der Waals interaction between two adjacent layers of TMDCs materials. These atomically thin layered materials are attractive for wide range of novel electronic, optoelectronic devices, sensors and other applications considering presence of a suitable band gap [2-10]. Recently, WS_2 has gaining a lot of attention as it possesses a band gap matching to the solar spectrum, which can be significant for optoelectronic devices [11-13]. A monolayer WS_2 is constructed with a sandwich of two atomic layers of S and one atomic layer of W through covalent W-S bonds, respectively. WS_2 shows a transition with a bulk indirect band gap to monolayer direct band gap of 1.4 eV and ~1.8 eV, respectively [14, 15]. It has been reported that WS_2 can act as an effective photoconductive layer in photo-detectors, photovoltaic devices and other optoelectronic devices [12, 13, 15]. Furthermore, hybridization of WS_2 layers with other 2D layered materials has been explored to fabricate vertical and in-plane heterostructure devices [16-18]. Considering the significant potential of WS_2 monolayer crystals in wide range of applications, the key challenge is controllable synthesis of large-area WS_2 crystals.

Recently, MoS_2 and WS_2 layered materials have been derived by various approaches, such as, mechanical exfoliation, liquid exfoliation, and sulfurization of transition metal and metal oxides [19-25]. Among these processes, CVD technique has attracted significant interest to obtain layered materials with control layer numbers, higher crystalline quality and large

single crystal [23-2]. The atomic layer growth process has significant advantages to obtain high-quality monolayer with wafer-scale uniformity [27]. At the same time, fabricating in-plane hetero structures of these materials is only possible by a growth technique [28]. However, there are several challenges to grow high quality WS₂ layers with the possibility of forming nanoparticles, few-layers structure and presence of residues thereby limiting the growth of individual crystals. In this work we have investigated WS₂ crystal growth using a tungsten halide precursor coated on SiO₂/Si substrate. In the developed process, a 0.05M solution of WCl₆ was drop-casted on the substrate, which was reduced and sulfurized by the APCVD process. We observed growth of triangular, star-shaped, as well as dendritic monolayer WS₂ crystals; where triangular crystals were obtained with a lateral size of more than 50 μm. The developed growth technique using solution-casted WCl₆ solid precursor can be significant to obtain large single crystals on arbitrary substrates.

4.2 Materials and methods

As explained in the chapter 2 section 2.1.2

4.3 Results and Discussion

The solution-casted WCl₆ precursor decompose effectively to react with S vapor for growth of WS₂ crystals. The density of WCl₆ precursor on substrate surface plays significant role in the nucleation and growth of WS₂ crystals.

Optical microscopy study

Figure 4-1 (a-d) shows optical microscope images of the synthesized WS₂ crystals with different shapes. We observed triangular monolayer WS₂ crystal along with six pointed star-shaped crystal. A nucleation point and growth of additional dendritic layers from the center can be observed for the star-shaped-crystals as shown in figure 4-1 (c-d). Various studies have been carried out on MoS₂ crystal synthesis and their geometrical structure evolution. It has been

reported that the geometry of MoS₂ crystals can be changed with pressure, temperature, substrates, precursors, cooling rates and other CVD parameters [29, 30]. In our experiments, we observed that various WS₂ crystal geometries can be obtained on the same sample substrate (figure 4-1 (a)), without changing any CVD parameters. This finding indicates that the sulfurization process of the precursor has a strong effect on the growth of individual domains. In the developed CVD process, S vapor flows along with Ar to the growth zone, where S reacts with W precursors for WS₂ crystal growth. Previously, Wang et al. has reported the formation of triangular and hexagonal geometries of MoS₂ domains with variation of MoO₃ precursor distribution [31]. Recent studies have also confirmed that mirror twin boundaries develop within a nucleated crystal, which determines the final geometry of the crystal [32]. Thus, the initial nuclei has a significant role in determining the final geometry of the WS₂ crystal.

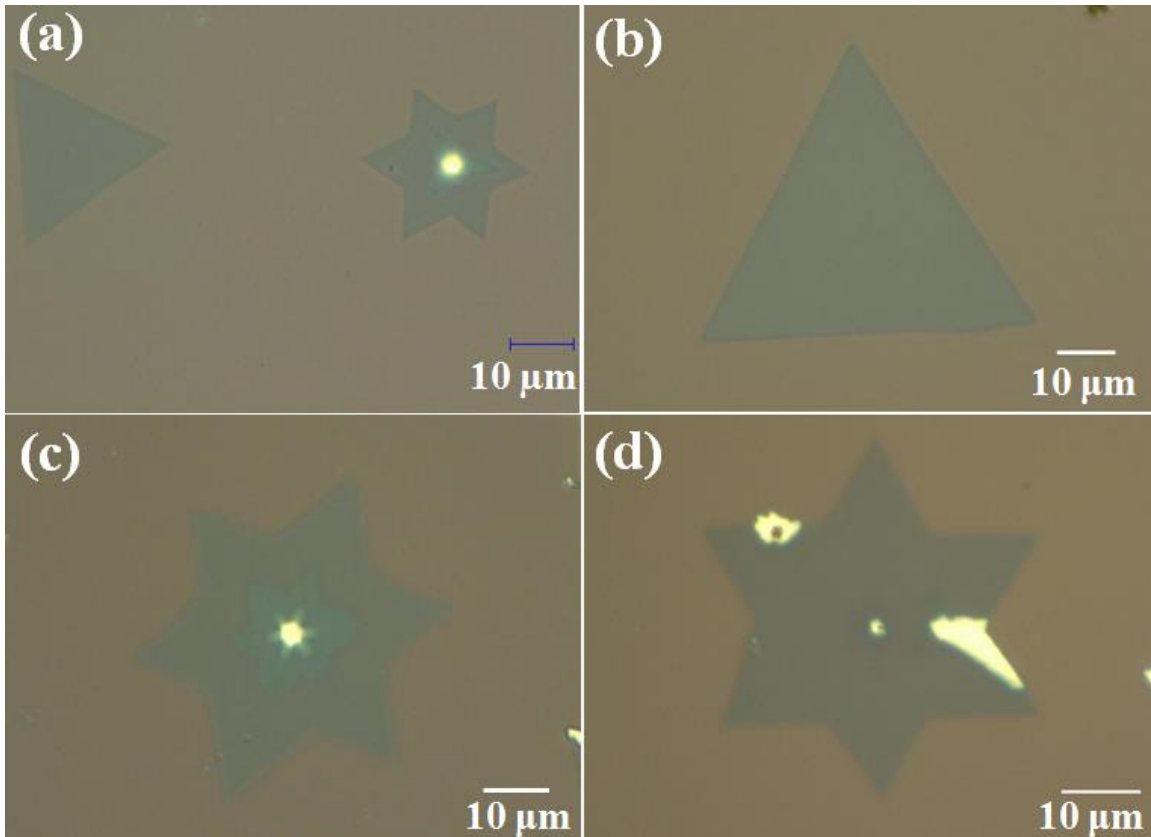


Figure 4-1 Optical microscope images of WS₂ crystals (a) with two different geometries on the same sample substrate, without changing any CVD parameters, (b) a triangular crystal. Six-arm star-shaped crystal with (c) and without (d) additional layer structures from the nuclei.

We have also observed growth of non-uniform triangular WS₂ crystal with a lateral size more than 100 μm. Figure 4-2 (a, b) shows optical microscope images of triangular-shaped WS₂ crystals with lateral size of 100 μm. However, we observed additional layers in the large crystals.

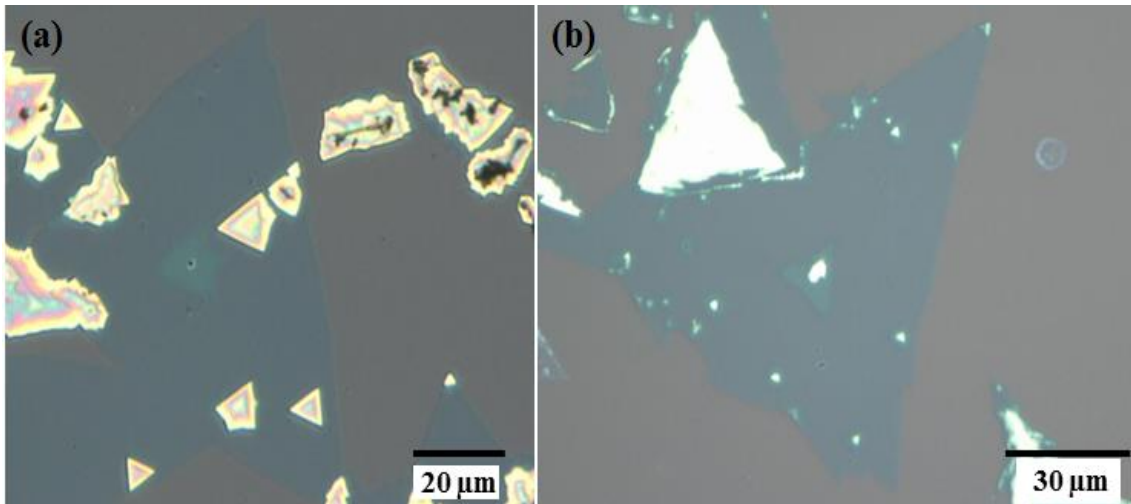


Figure 4-2 (a), (b) optical microscope image of triangular-shaped WS₂ crystal with lateral size of around 100 μm.

FE-SEM Study

Figure 4-3 shows FE-SEM analysis of the synthesized WS₂ crystals on the same sample substrate. As explained for the optical microscope images, we obtained WS₂ crystals with various geometries, which also can be confirmed by FE-SEM analysis.

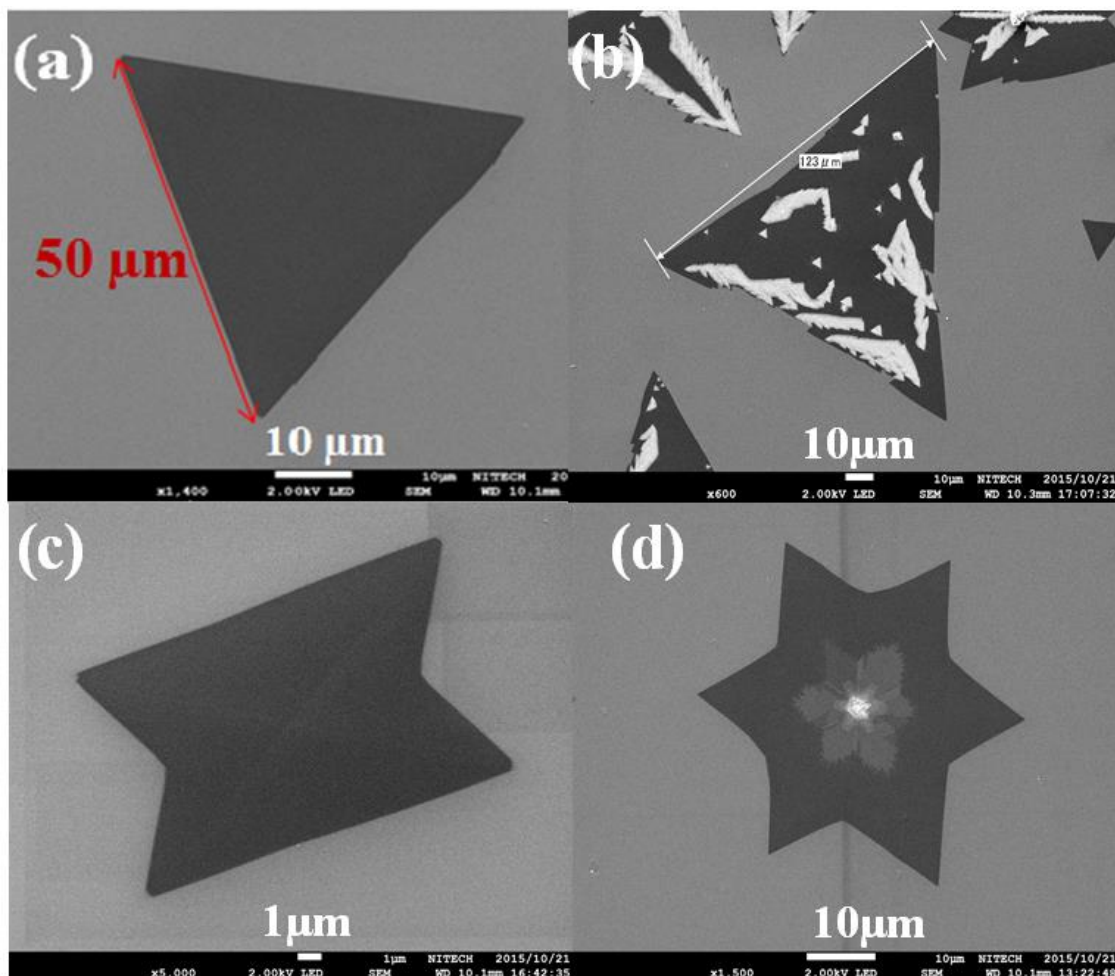


Figure 4-3 FE-SEM images of (a) triangular monolayer WS_2 crystal. (b) Uncompleted growth of triangular-shaped WS_2 crystal (size $\sim 123 \mu m$). FE-SEM images of WS_2 crystal with a geometry of (d) butterfly and (e) six-arm star-shaped.

Figure 4-3(a) shows a triangular monolayer WS_2 crystal of $50 \mu m$ size. Similarly, figure 4-3 (b) shows a FE-SEM image of triangular shaped crystal with a lateral size of $123 \mu m$. Figure 4-3 (c) shows a WS_2 crystal with a geometry of butterfly with much smaller size. Similarly, figure 4-3 (d) shows a six pointed star-shaped crystal, where in the center we can observe the nucleation point and growth of additional layers. As explained previously WS_2 crystals with various geometries are obtained on the same sample substrate, without changing any CVD parameters.

This indicates strong influence of W precursor and S vapor reaction process at a particular nucleation site. The mirror twin boundaries in a nucleated crystal can determine final butterfly, six pointed star-shaped and other various geometries of the crystals. As well as, thicker truncated triangular WS_2 crystals formation is observed with merging of smaller triangles. We also observed vertical growth of WS_2 sheets from the SiO_2/Si substrate with sulfurization of a larger cluster of WCl_6 precursor. Our findings show that the nucleation of WS_2 crystals significantly affects the final crystal geometry.

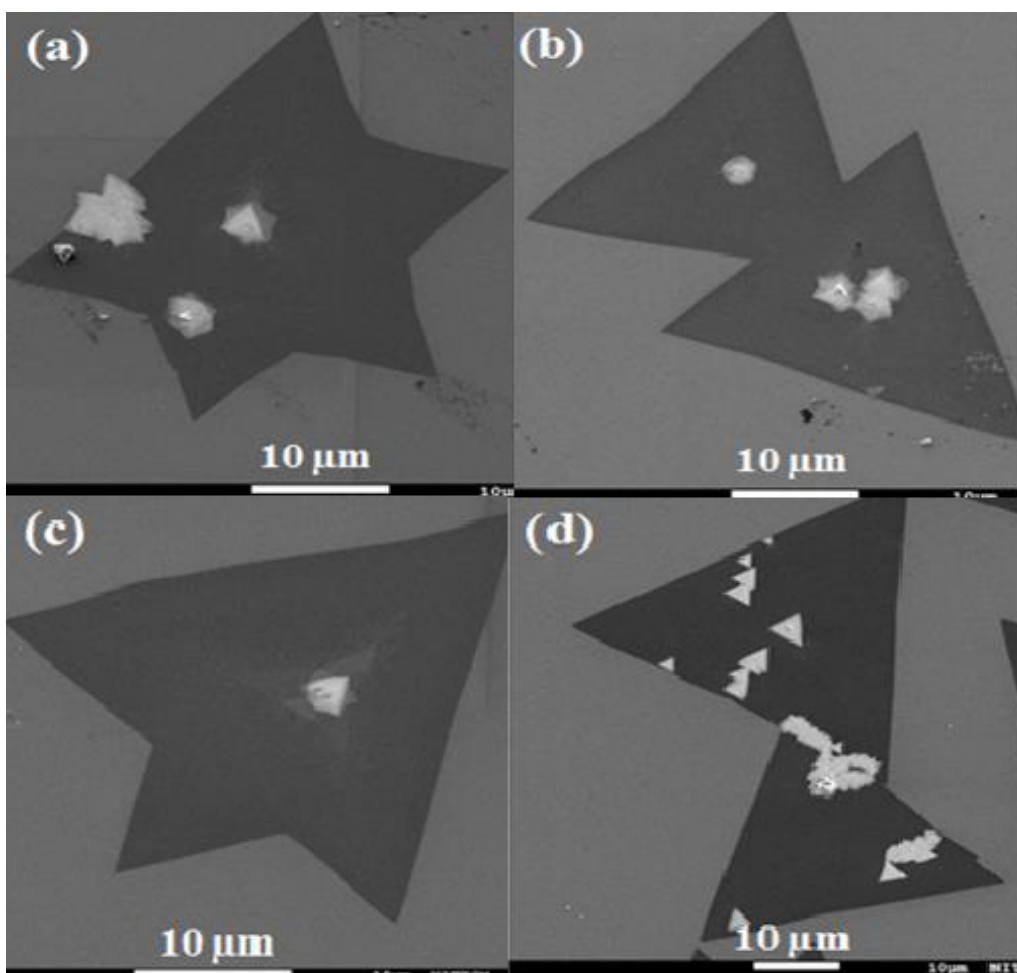


Figure 4-4 (a-d) FE-SEM images of the as grown WS_2 crystals on SiO_2/Si substrate with various geometries.

Figure 4-4 (a-d) shows FE-SEM images of the as-grown WS₂ crystals on SiO₂/Si substrates with various geometries. Not only the above mentioned WS₂ crystals are observed, but also several other geometries are obtained as shown in the FE-SEM images. Figure 4-4 (b) shows two triangular crystals nucleated from two different nuclei creating an overlapped structure, where a grain boundary forms at the point of interconnection [34, 35]. Similarly, figure 4-4 (d) shows two triangular crystals with 180° rotation to each other, similar crystals growth has been also reported for MoS₂ [36, 37]. As explained in the manuscript the nuclei of individual crystal significantly influence on the final geometry. Figure 4-5 (a) shows formation of 3 pointed star-shaped WS₂ crystals. This type of structure form with formation of series of triangles, which merged together to create a thicker truncated triangular structure. Previously Cong et al, has reported that the 3 pointed star structure transformed into monolayer triangular crystal with continuous heating and growth process [38]. Figure 4-5 (c) shows vertical growth of WS₂ sheets from the SiO₂/Si substrate surface with sulfurization of a cluster of WCl₆ precursor. Our findings show that the nucleation of WS₂ crystals significantly affects the final crystal geometry.

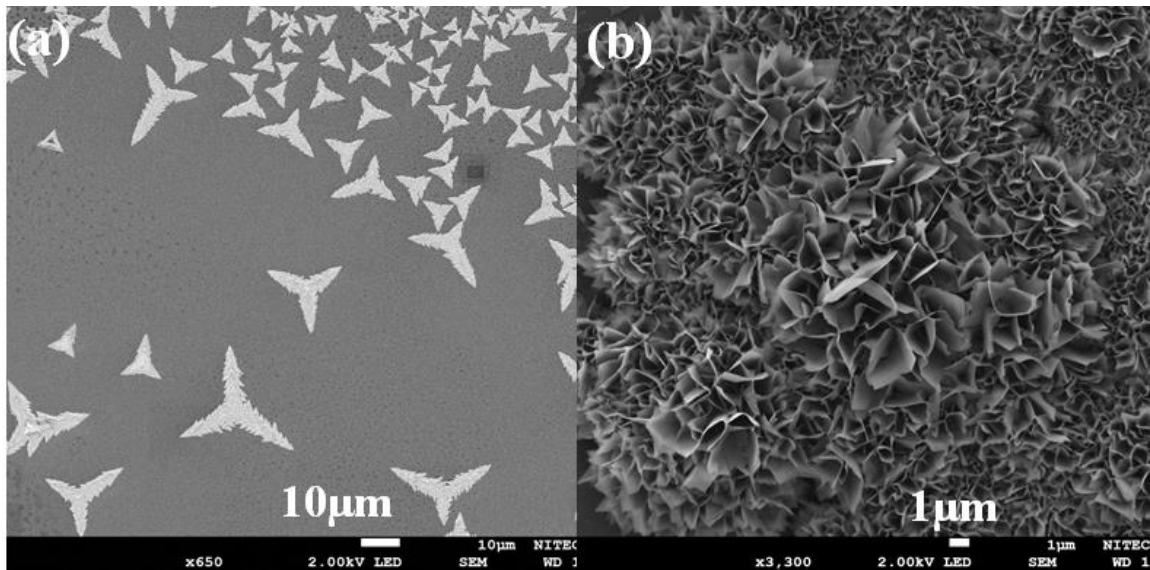


Figure 4-5 (a) Formation of 3 pointed star-shaped WS_2 crystal. (b) Growth of WS_2 sheets vertically from the SiO_2/Si substrate surface with sulfurization of a cluster of WCl_6 precursor.

The formation of additional layer at the center part of was further investigated by FE-SEM analysis. Figure 4-6 (a) shows star-shaped-crystals with highly symmetric six-arm structures. Now, if we concentrate at the center part of crystal around the nucleation site, dendritic growth is visible as shown in figure 4-6 (b) . The dendrite propagates in different directions from the nuclei. Similarly, figure 4-6 (c) shows a WS_2 triangular crystal coexisting with other growth fronts.

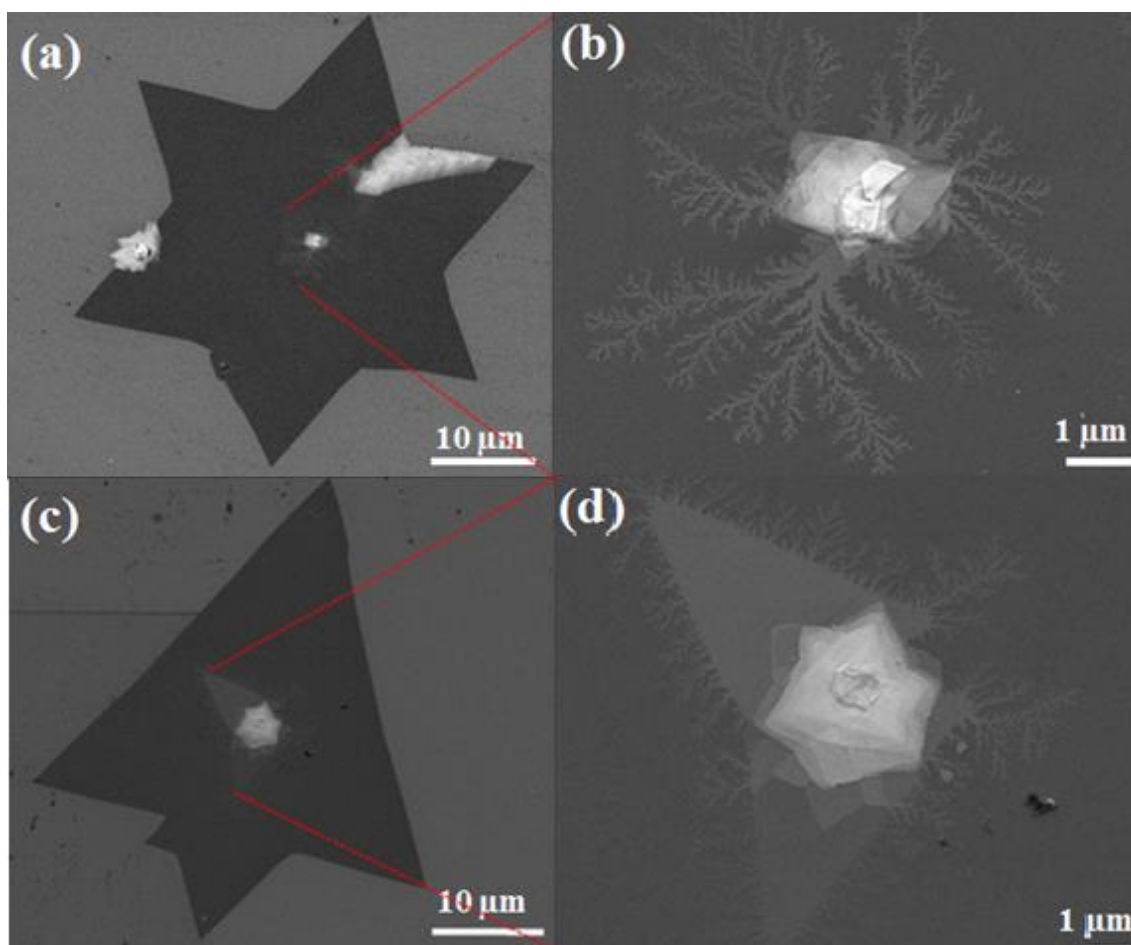


Figure 4-6 FE-SEM images of (a) star-shaped crystal with additional dendritic growth from the nuclei, (b) propagation of dendritic structure from the nuclei, (c) triangular crystal coexisting with other growth fronts and (d) dendritic growth fronts from the nuclei of the original crystal.

Previous studies have revealed presence of grain boundaries of such complicated WS₂ domains. The final geometry of the domain significantly affect by the nuclei. Figure 4-6 (d) shows dendritic growth fronts from the nuclei of the original crystal. As observed from the images dendritic growth fronts are significantly differ with initial shape of the nuclei. The grain boundaries are originated in the early stage of growth depending on the size and shape of the

nuclei which define the final geometries of WS₂ crystal. The observations of dendritic growth fronts from individual nuclei for various different geometries of WS₂ domain provide significant insight of the growth process in our developed CVD process.

Raman Study

Figure 4-7 shows a Raman mapping images of the six pointed star-shaped and triangular WS₂ crystals. Figure 4-7 (a, b) shows mapping images for the E¹_{2g} (363 cm⁻¹) and A¹_g (430 cm⁻¹) peaks for the six pointed star-shaped crystal with a laser excitation energy of 532.08 nm. Much higher intensity of E¹_{2g} peak is observed than that of A¹_g peak from the mapping images; however the intensity distribution is not uniform for the star-shaped crystal. The intensity of E¹_{2g} peak reduces at the center, while increases for the A¹_g peak. This confirms the nucleation point and additional layers growth at the center of the star-shaped crystal. As well as, it has been confirmed that the frequency of E¹_{2g} peak decreases while for the A¹_g peak increases with increasing layer number. Figure 4-7 (c, d) shows mapping images of full width at half maximum (FWHM) for the E¹_{2g} and A¹_g peaks of star shaped crystals. The FWHM of E¹_{2g} peak is slightly higher than that of the A¹_g peak. Other significant change in FWHM was not observed for both the E¹_{2g} and A¹_g peaks.

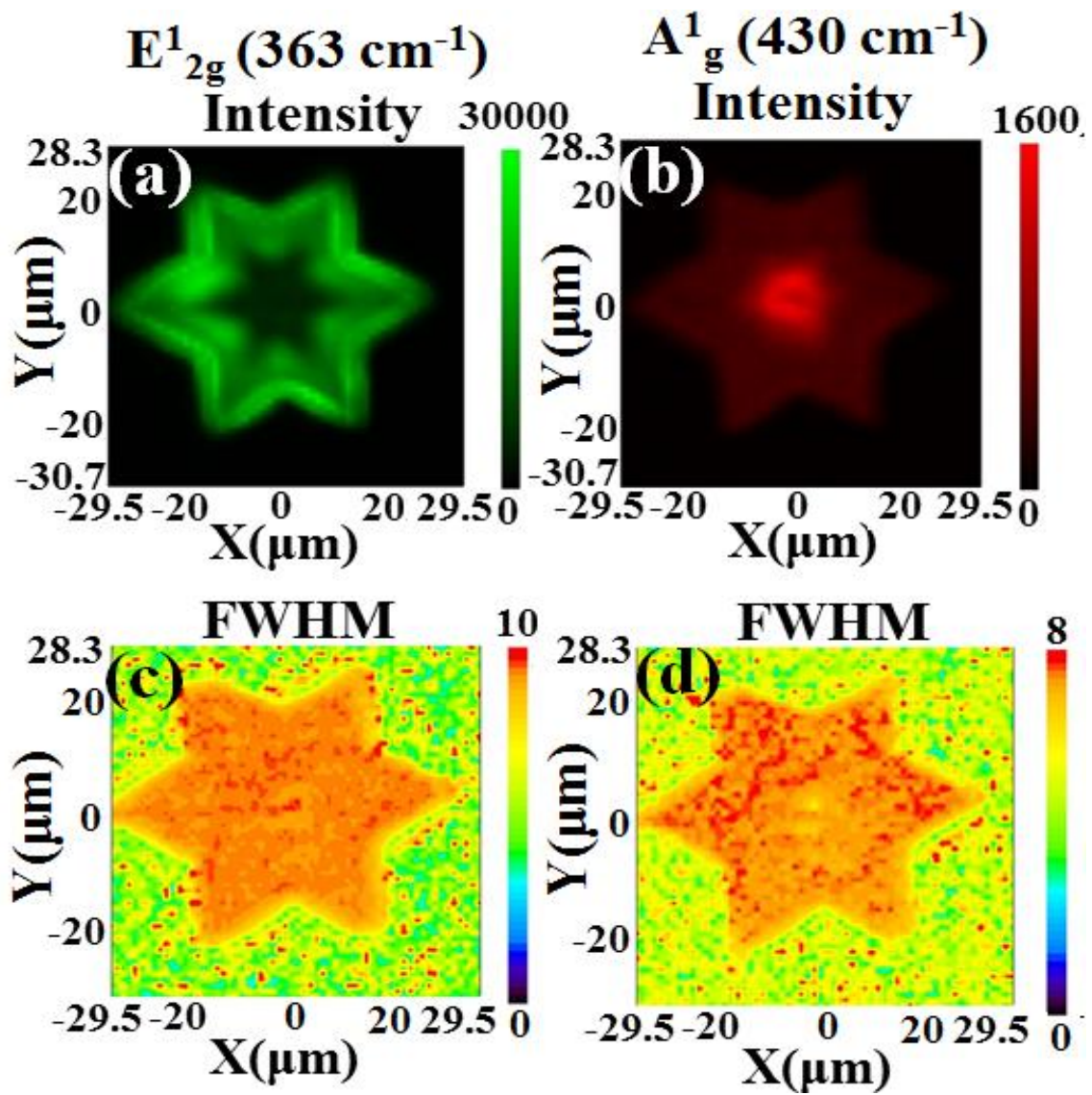


Figure 4-7 Raman mapping images for the six-arm star-shaped crystal (a) E_{2g}^1 (363 cm^{-1}), (b) A_g^1 (430 cm^{-1}) peak intensities and (c) E_{2g}^1 , (d) A_g^1 full width at half maximum (FWHM) of the peaks.

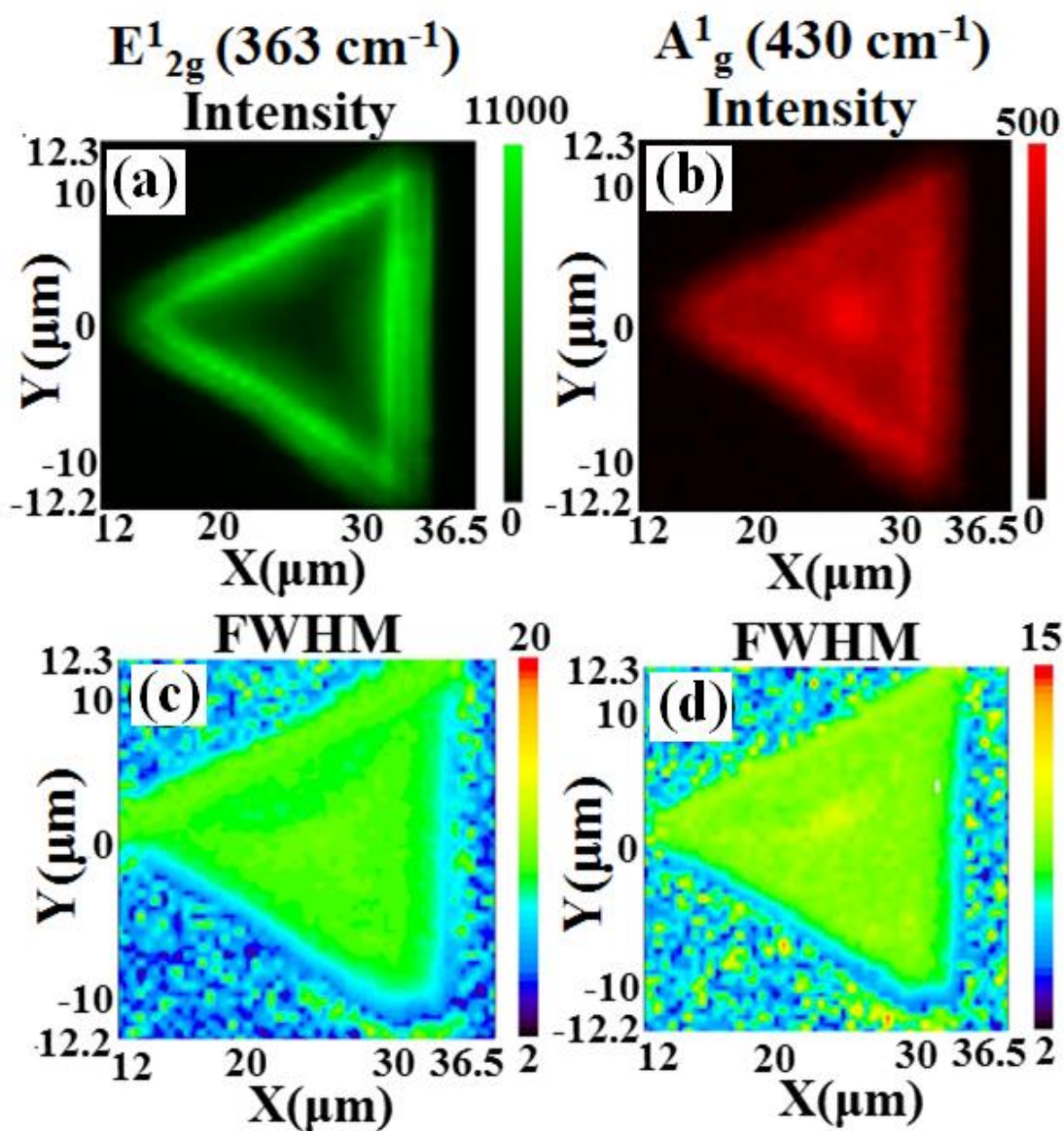


Figure 4-8 Raman mapping images for the triangular crystal (a) E_{2g}^1 (363 cm^{-1}), (b) A_g^1 (430 cm^{-1}) peak intensities and (c) E_{2g}^1 , (d) A_g^1 FWHM of the peaks. (Laser excitation energy $\sim 532.08\text{ nm}$)

Figure 4-8 (a, b) shows mapping images for the E_{2g}^1 and A_g^1 peaks for the triangular crystal with same laser excitation energy. The intensity distribution for the A_g^1 peak does not change significantly in contrast to star shaped crystal. Figure 4-8 (c, d) shows mapping images of

FWHM for the E_{2g}^1 and A_{1g}^1 peaks of the triangular crystal. Similar to previous case, the FWHM for the E_{2g}^1 peak is higher than that of the A_{1g}^1 . Again, FWHM for both the E_{2g}^1 and A_{1g}^1 peaks are almost uniform. Raman analysis showed that the triangular WS_2 crystal is a monolayer, which was further confirmed by AFM. The Raman mapping analysis provided a detail view of the star-shaped and triangular WS_2 crystals formation and nucleation sites. Further, layer distribution can be confirmed with blue and red-shift of Raman peaks, where the Van der Waals and Coulombic interlayer interactions plays significant roles in atomic vibration [34].

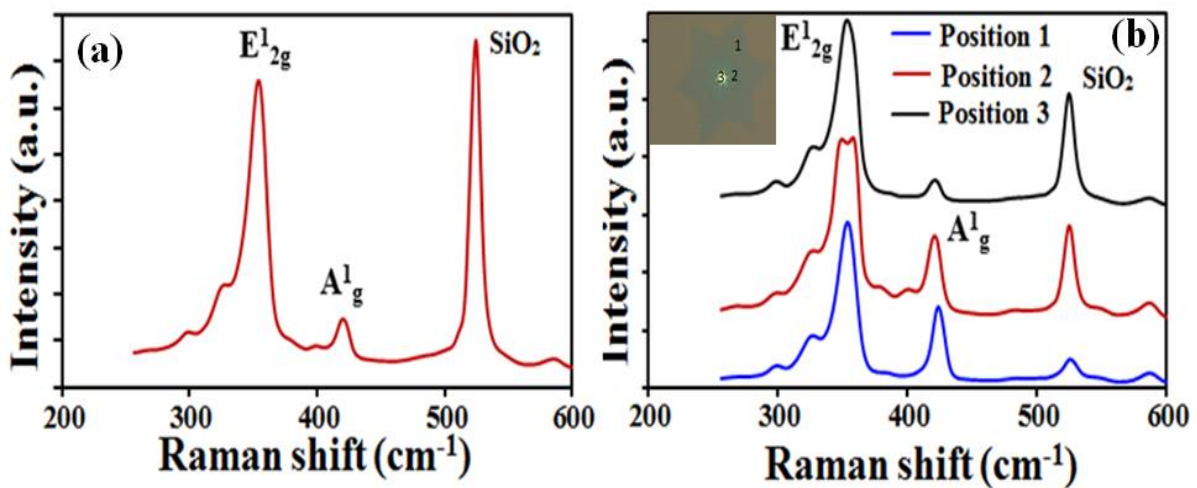


Figure 4-9 (a) Raman spectra of triangular WS_2 crystal and (b) Raman spectra of six armed star-shaped crystal (inset of the figure) at three different positions (1, 2 and 3)

Correlating the mapping analysis point Raman spectra were also analyzed. Figure 4-9 (a) shows Raman spectra of the triangular crystal. The peaks for E_{2g}^1 and A_{1g}^1 mode are observed at around ~ 360 and $\sim 430\text{ cm}^{-1}$, respectively. The intensity ratio of the peaks of A_{1g}^1 and E_{2g}^1 (A_{1g}^1/E_{2g}^1) is around 0.22, which corresponds a monolayer WS_2 . Similarly, Raman analysis was performed for six-armed star-shaped crystal at three different points as shown in the figure. Figure 4-9 (b) shows Raman spectra at positions 1, 2 and 3 optical microscope images. Similar E_{2g}^1 and A_{1g}^1 peaks are observed; however the intensity ratio of the two peaks significantly changes.

AFM Study

Figure 4-10 shows an AFM image of the as-synthesized WS₂ crystal on SiO₂/Si substrate. Line profile at the edge, presenting an approximate thickness of around ~0.9 nm, which is almost comparable to monolayer WS₂ crystal.

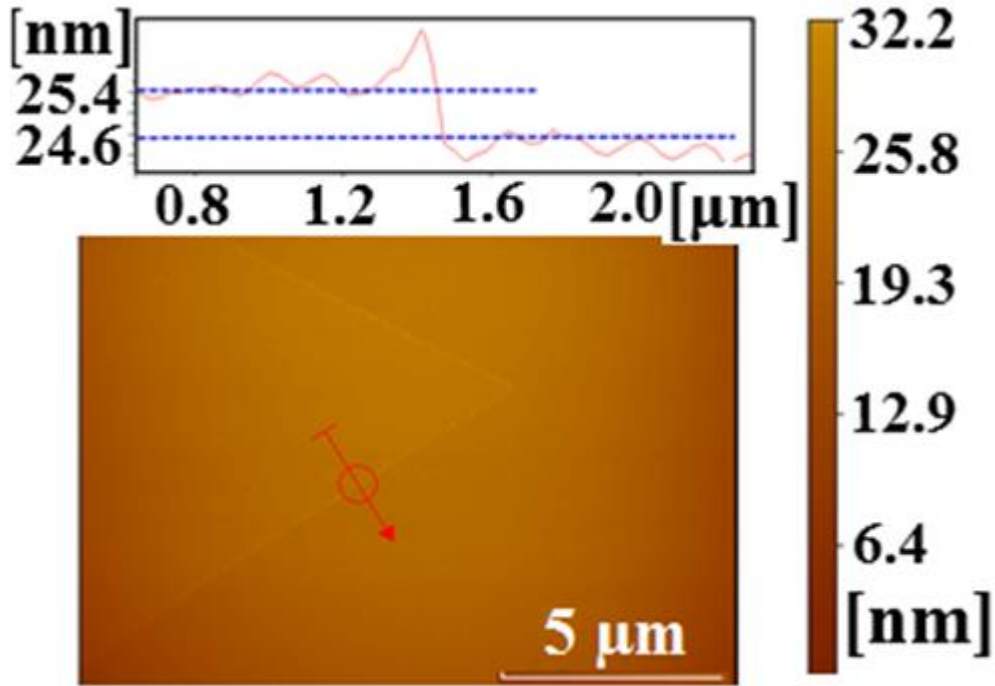


Figure 4-10 AFM image and line profile of the as-synthesized WS₂ crystal on SiO₂/Si substrate.

PL Spectroscopy Study

Figure 4-11 (a) shows PL spectra of a triangular-shaped WS₂ crystal at room temperature. PL measurements are carried out with an excitation wavelength of ~532 nm and laser power of ~16 mW. We did not observe much change in the PL spectra at two different locations of the crystal. It has been reported that PL peak is difficult to obtain for multi-layer WS₂ crystals, as band gap changes from direct to indirect with number of layers increasing from mono to multi-layer [26]. Peak position of the PL spectra is obtained at ~641.47 nm, corresponding to 1.93 eV, similar to reported previous values [21, 22]. The FWHM of the PL peak was obtained as 60 meV, which is comparable to other CVD-grown WS₂ crystals [22].

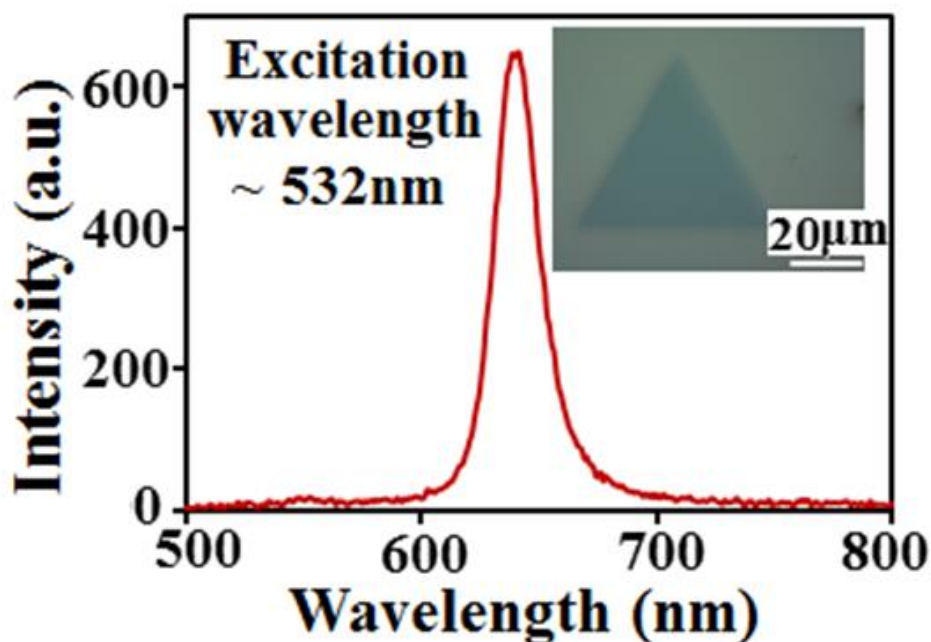


Figure 4-11 (a) PL spectra of the triangular-shaped (inset of the figure) WS₂ crystal.

4.4 Conclusion

We have demonstrated a simpler and effective approach to synthesis WS₂ crystals using drop-casted WCl₆ precursor on SiO₂/Si substrate. We observed high quality WS₂ crystals growth using 0.05M WCl₆ precursor with well distribution of nucleation sites on the in dendritic growth fronts were observed depending on the initial shape of the nuclei. The observation of dendritic growth front from individual nuclei for various different geometries of WS₂ domain provide significant insight of the growth process in the CVD substrate. Triangular, star-shaped and various other WS₂ crystal geometries were obtained in this growth process. We observed formation of dendritic additional layer structures at the center of six arm star-shaped and some of the other crystals. Significant differences process. These results showed that a solution-casting technique can be adopted for tungsten halide precursors for control growth of WS₂ monolayer crystals.

4.5 References

- [1] Splendiani, L. Sun, Y. Zhang, T. Li, J. Kim, and C.-Y. Chim, Nano Lett. 2010, 10, 1271.

- [2] Mas-Balleste, C. Gomez-Navarro, J. Gomez-Herrero, F. Zamora, *Nanoscale* 2011, 3, 20
- [3] Radisavljevic, A. Radenovic, J. Brivio, V. Giacometti, A. Kis. *Nature Nanotechnol* 2011, 6, 147.
- [4] Q. H. Wang, K. Kalantar-Zadeh, A. Kis, J. N. Coleman, and M. S. Strano, *Nature Nanotechnol.* 2012, 7, 699.
- [5] K. F. Mak, C. Lee, J. Hone, J. Shan, and T. F. Heinz, *Phys. Rev. Lett.* 2010, 105, 136805.
- [6] J. Pu, Y. Yomogida, K. K. Liu, L. J. Li, Y. Iwasa, T. Takenobu, *Nano Lett.* 2012, 12, 4013.
- [7] G. Eda, H. Yamaguchi, D. Voiry, T. Fujita, M. Chen, M. Chhowalla, *Nano Lett.* 2011, 11, 5111.
- [8] S. M. Shinde, G. Kalita, and M. Tanemura, *J. Appl. Phys.* 2014, 116, 214306.
- [9] M. Armstrong, C. O'Dwyer, W. Macklin, and J. Holmes, *Nano Res.* 2014, 7, 1 .
- [10] Y. Zhang, T.-R. Chang, B. Zhou, Y.-T. Cui, H. Yan, Z. Liu, F. Schmitt, J. Lee, R. Moore, Y. Chen, H. Lin, H.-T. Jeng, S.-K. Mo, Z. Hussain, A. Bansil, and Z.-X. Shen, *Nat. Nanotechnol.* 2013, 9, 111 .
- [11] A. Jager-Waldau, M. Lux-Steiner, G. Jager-Waldau and E. Bucher, *Appl. Surf. Sci.* 1993, 70/71, 731.
- [12] X. Hong, J. Kim, S.-F. Shi, Y. Zhang, C. Jin, Y. Sun, S. Tongay, J. Wu, Y. Zhang, and F. Wang, *Nature Nanotechnol.* 2014, 9, 682.
- [13] F. H. L. Koppens, T. Mueller, Ph. Avouris , A. C. Ferrari, M. S. Vitiello, and M. Polini, *Nature Nanotechnol.* 2014, 9, 780.
- [14] A. Klein, S. Tiefenbacher, V. Eyert, C. Pettenkofer, and W. Jaegermann, *Phys. Rev.* 2001, B 64, 2054.

- [15] L. Britnell, R. M. Ribeiro, A. Eckmann, R. Jalil, B. D. Belle, A. Mishchenko, Y.-J. Kim, R. V. Gorbachev, T. Georgiou, S. V. Morozov, A. N. Grigorenko, A. K. Geim, C. Casiraghi, A. H. Castro Neto, and K. S. Novoselov, *Science* 2013, 340,1311.
- [16] X. Duan, C.Wang, J. C. Shaw, R. Cheng, Y. Chen, H. Li, X. Wu, Y. Tang, Q. Zhang, A. Pan, J. Jiang, R. Yu, Y. Huang, and X. Duan, *Nature Nanotechnol.*2014, 9, 1024 .
- [17] Y. Jung, J. Shen, Y. Sun, J. J. Cha, *ACS Nano* 2014, 8(9), 9550.
- [18] K. Liu, Q. Yan, M. Chen, W. Fan, Y. Sun, J. Suh, D. Fu, S. Lee, J Zhou, S. Tongay, J. Ji, J. B. Neaton, and J. Wu, *Nano Lett.* 2014, 14(9), 5097.
- [19] L. Cheng, W. Huang, Q. Gong, C. Liu, Z. Liu, Y. Li, H. Dai, *Angew Chem. Int. Ed. Engl.* 2014, 53, 7860.
- [20] C. Cong, J. Shang, X. Wu, B. Cao, N. Peimyoo, C. Qiu, L. Sun, and T. Yu, *Adv. Opt. Mater.*2014, 2, 131.
- [21] A. L. Elías, N. Perea-López, A. Castro-Beltrán, A. Berkdemir, R. Lv, S. Feng, A. D. Long, T. Hayashi, Y. A. Kim, M. Endo, H. R. Gutiérrez, N. R. Pradhan, L. Balicas, T. E. Mallouk, F. López-Urías, H. Terrones, and M. Terrones, *ACS Nano* 2013, 7, 5235.
- [22] K. N. Kang, K. Godin, and E.-H. Yang, *Sci. Rep.* 2015, 5, 13205.
- [23] X. L. Li, J. P. Ge, and Y. D. Li, *Chem. - A Eur. J.* 2004, 10, 6163.
- [24] R. Lv, J. a. Robinson, R. E. Schaak, D. Sun, Y. Sun, T. E. Mallouk, and M. Terrones, *Acc. Chem. Res.* 2015, 48, 56.
- [25] M. Okada, T. Sawazaki, K. Watanabe, T. Taniguch, H. Hibino, H. Shinohara, and R. Kitaura, *ACS Nano* 2014, 8(8), 8273.
- [26] J. Park, W. Lee, T. Choi, S.-H. Hwang, J. M. Myoung, J.-H. Jung, S.-H. Kim, and H. Kim, *Nanoscale* 2015, 7, 1308.
- [27] Y. Shi, H. Li, and L.-J. Li, *Chem. Soc. Rev.* 2015, 44, 2744.

- [28] Y. Gong, J. Lin, X. Wang, G. Shi, S. Lei, Z. Lin, X. Zou, G. Ye, R. Vajtai, B. I. Yakobson, H. Terrones, M. Terrones, B. K. Tay, J. Lou, S. T. Pantelides, Z. Liu, W. Zhou and P. M. Ajayan, *Nature Mater.* 2014, 13, 1135 .
- [29] A. M. van der Zande, P. Y. Huang, D. a Chenet, T. C. Berkelbach, Y. You, G.-H. Lee, T. F. Heinz, D. R. Reichman, D. Muller, and J. C. Hone, *Nat. Mater.* 2013, 12, 554 .
- [30] X. Ling, Y.-H. Lee, Y. Lin, W. Fang, L. Yu, M. S. Dresselhaus, J. Kong, *Nano Lett.* 2014,14, 464.
- [31] S. Wang, Y. Rong, Y. Fan, M. Pacios, H. Bhaskaran, K. He, J. H. Warner, *Chem. Mater.* 2014, 26, 6371.
- [32] A. M. van der Zande, P. Y. Huang, D. a Chenet, T. C. Berkelbach, Y. You, G.-H. Lee, T. F. Heinz, D. R. Reichman, D. a Muller, J. C. Hone, *Nat. Mater.* 2013, 12, 554.
- [33] H. Li, Q. Zhang, C. C. R. Yap, B K. Tay, T. H. T. Edwin, A. Olivier, D. Baillargeat, *Adv. Funct. Mater.* 2012, 22, 1385.
- [34] T. Jiang, Q. Ji, Y. Zhang, Z. Li, Y. Shan, Y. Zhang, X. Gong, W. Liu, S. Wu, *Adv. Mater.* 2015, 27, 4069.
- [35] A. M. van der Zande, P. Y. Huang, D. A. Chenet, T. C. Berkelbach, Y. You, G.-H. Lee, T. F. Heinz, D. R. Reichman, D. A. Muller, J. C. Hone, *Nature Mater.* 2013, 12, 554.
- [36] Z. Liu, M. Amani, S. Najmaei, Q. Xu, X. Zou, W. Zhou, T. Yu, C. Qiu, A. G. Birdwell, F. J. Crowne, R. Vajtai, B. I. Yakobson, Z. Xia, M. Dubey, P. M. Ajayan, J. Lou, *Nature Commun.* 2014 5, 5246 .
- [37] Y. Zhang, Y. Zhang, Q. Ji, J. Ju, H. Yuan, J. Shi, T. Gao, D. Ma, M. Liu, Y. Chen, X. Song, H. Y. Hwang, Y. Cui, and Z. Liu, *ACS Nano* 2013,7(10), 8963.

- [38] C. Cong, J. Shang, X. Wu, B. Cao, N. Peimyoo, C. Qiu, L. Sun, and T. Yu, Adv. Optical Mater. 2014, 2, 131.

CHAPTER 5

Synthesis of Graphene and study of hydrogen etching of its crystal and film

5.1 Introduction

Synthesis of graphene by CVD process has been significantly explored owing to the possibility of depositing on a large-area with controllable layers number and large single crystal domains.[1-5] Synthesis of large single crystal graphene has been reported on Cu substrates using the LP and APCVD techniques.[6-12] Graphene growth on Cu surface is influenced by several factors such as, native oxygen, H₂, gas compositions, growth temperatures, flow rate of carbon source, and surface structure of substrate [6,13-17]. Thus, the morphology and structure of graphene crystals significantly differ with CVD processes and experimental conditions. Single and multilayer graphene with variety of shapes can be synthesized by the CVD method, which allows to fabricate controlled stacking and assembly of graphene. Hierarchical graphene architectures of hexagonal-snowflake-dendritic stacking have been also obtained by the CVD technique. [18] The graphene crystal nucleation and growth kinetics are important aspects, which control the monolayer, few-layer, hexagonal structure, layer stacking, and dendrite growth process. As various studies showed the effect of H₂ in the graphene growth process, there is significant influence of H₂ on etching process as well. [13, 19-21] H₂ induced etching of graphene is a fascinating tool to fabricate nanoribbons, hexagonal holes, Y-shaped junctions, and other nanostructures with control edges. [22– 24] Anisotropic etching behavior of graphene has been explored with metal nanoparticles in presence of H₂, oxidation, and introduction of water vapor at high temperature annealing. [25-28] Hexagonal holes were created with well-defined edges by the etching process for fabrication of inplane heterostructure with h-BN. [29] Very recently, we have demonstrated nanoribbons and Y-shaped junctions fabrication by H₂

induced anisotropic etching. [24] The graphene nanoribbons with armchair edges possess a band gap changing with the width of ribbons, while zigzag edges shows magnetically ordered edge states [30-33]. These features of nanoribbons only can be observed with very regular and pronounced edge structures. Regular edge structures can be obtained with highly anisotropy etching of graphene depending on the chemical reactivity of zigzag and armchair edges. This is an important aspect to fabricate well-defined structures of high quality CVD graphene for nano-electronics application. However, the etching process of individual graphene crystals can significantly differ with their original structure and morphology. In this prospect, exploring the etching behavior of snowflake-dendritic and other graphene crystals provide us an important information of growth and etching process. Significant differences in H₂ induced etching behavior were observed for the snowflake dendritic and other graphene crystals by annealing at 1055° C in a H₂ and Ar gas mixture

5.2 Materials and methods

Graphene synthesis

As explained in the chapter 2 section 2.2.1

Graphene transfer

As explained in the chapter 2 section 2.2.2

5.3 Results and discussion

On the electro-polished Cu foil, dendritic hexagonal shaped graphene crystals were obtained using solid camphor source in the APCVD process. While, graphene crystals apart from dendritic structures were also obtained in the same sample. This suggests that in particular, conditions graphene nucleation and growth of individual domains are not homogenous. At a steady atmosphere, six-fold symmetric hexagons can be obtained. Again, the growth of snowflake-dendritic structures indicate a diffusion limited growth kinetic as reported

previously.[34] Now, we observed interesting etching behavior of such graphene crystals by annealing at 1055 °C in Ar:H₂ gas mixture.

Optical microscope study

Figure 5-1(a) shows optical microscope image of H₂ induced etching of the hexagonal shaped dendritic structure along with non-dendritic graphene crystals. Inset of Figure 5-1(a) shows magnified view of the etched dendritic graphene. All the dendritic crystals were etched symmetrically from the branches of individual lob creating fractal pattern. [28] Figure 5-1(b) shows the etching features of graphene, where there were no dendrite crystals. Hexagonal holes and formation ribbon like structures can be confirmed owing to anisotropic etching process. Hexagonal-hexagonal-hexagonal stacking (stacking of three hexagonal layers) along with the snow- flake dendritic crystals is also observed. Figure 5-1(c) shows an optical microscope image of the etched dendritic and regular graphene crystals overlapping each other on the Cu foil. The graphene crystals were also transferred to SiO₂/Si substrate to obtain much clear information.

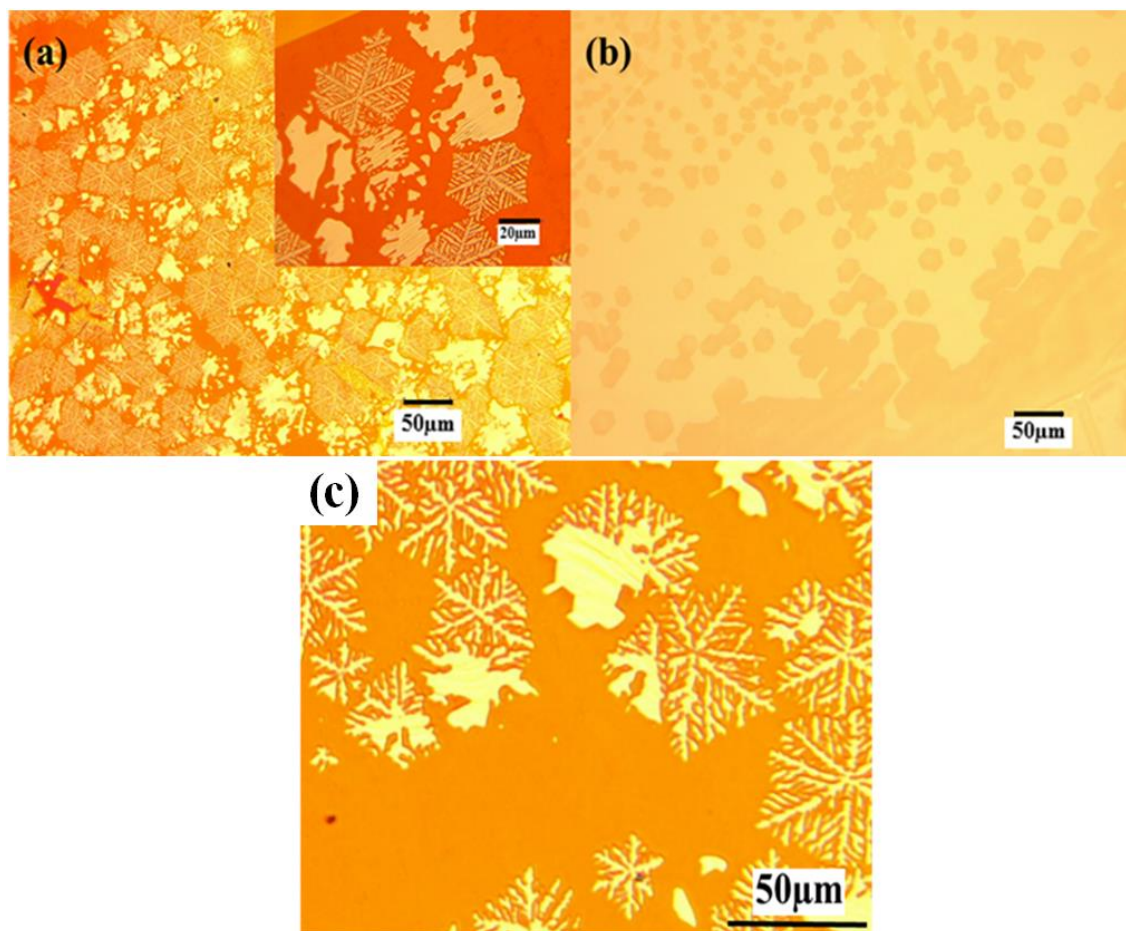


Figure 5-1. Optical microscope image of H₂ induced etching of (a) dendritic graphene along with regular graphene crystals (inset of the image magnified view). (b) Etching features of regular graphene. (c) Etched hierarchical graphene structures on Cu foil

Figure 5-2(a) shows an optical microscope image of the etched graphene crystals after transferring to SiO₂/Si substrate. The morphology of etched six-lobed dendritic and regular graphene crystals remains undamaged after the transfer process. Now, the graphene crystals on SiO₂/Si substrate show significant difference in color contrast. The six-lobed dendritic graphene is darker blue color than that of regular graphene crystals. Graphene stacking structures on SiO₂/Si substrate can be clearly recognized from the color contrast in the optical microscope image.

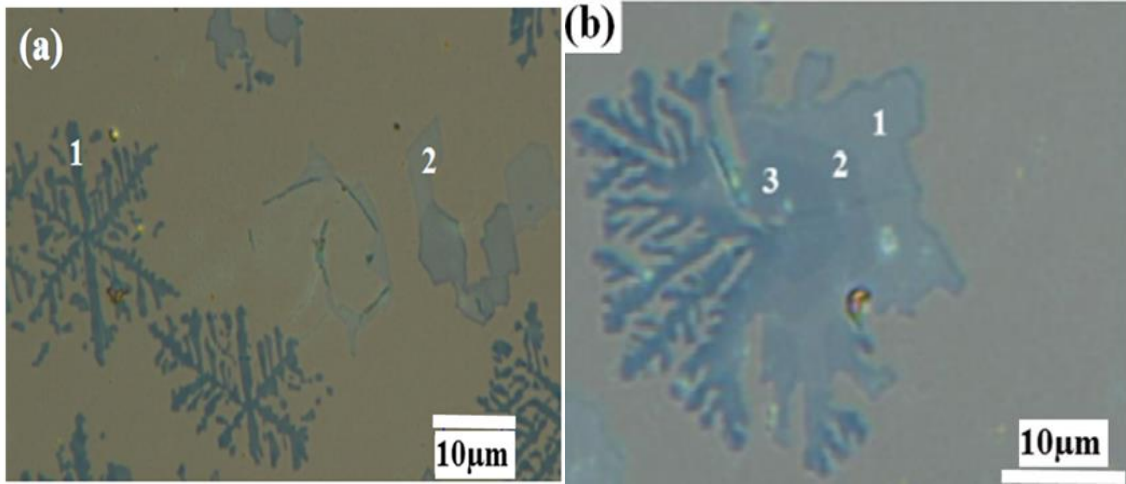


Figure 5-2 Optical microscope image of (a) Etched graphene crystals after transferring to SiO_2/Si substrate. (b) Stacking of hexagonal-hexagonal-hexagonal graphene (stacking of three hexagonal layers) along with the snowflake dendritic crystals on SiO_2/Si .

In the sample, we have also observed growth of graphene crystals with hierarchical structures. Such type of hierarchical structures of graphene is obtained with multiple nuclei of non-simultaneous seeding on the Cu surface, in addition to simultaneous seeding at the center of hexagonal crystal. Thus, the dendrite crystal grows from a separate seed, while the hexagonal three layers stacked structure grow from simultaneous seeding in this particular growth conditions. Non-simultaneous seeding occurs when the active carbon atoms find a more energetically favorable location rather than contributing to former domain growth [18].

FE-SEM Study

Figure 5-3(a) shows a FE-SEM image of etched six-lobed dendrite graphene crystals. Inset of Figure 5-3(a) shows a higher resolution FE-SEM image of the etched dendrite. From the image, it can be observed that the lobes are not fully etched and etching occurs from edges of branches, where all the hexagonal shaped snowflake-dendritic crystals have similar etching

pattern. Figure 5-3 (b) shows FE-SEM images of etched graphene crystals across two Cu grains. The etching occurs with clear edge structures, in contrast to the etching pattern of dendritic graphene. The graphene edges create angle of 60 and 120 as observed from the FE-SEM image, indicating etching along crystallographic directions. Thus, we observed simultaneous anisotropic and fractal etching behavior of the graphene domains depending on their original structures. The understanding of graphene etching process can be critical to fabricate well-defined shape with controlled edge structures. Figure 5-3(c) shows a FE-SEM image of the etched six lobed dendritic graphene and usual graphene crystals.

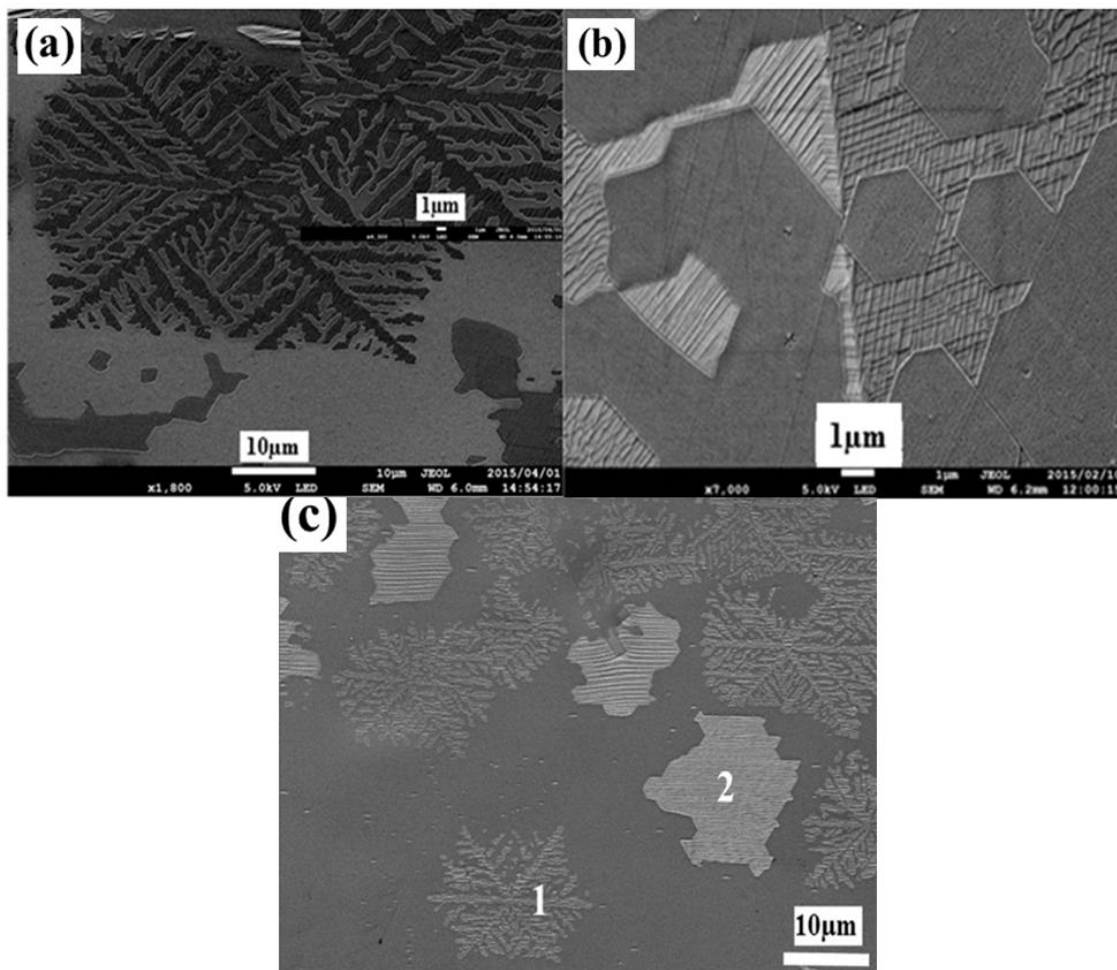


Figure 5-3 FE-SEM images of the etched (a) six-lobed dendritic graphene crystals (inset of the image magnified view). (b) Regular graphene crystals across two Cu grains. (c) six-lobed dendritic graphene along with regular graphene crystals.

Raman Study

Raman studies were carried out to investigate the structural properties of these two kinds of graphene crystals. Figure 5-4 (a) shows Raman spectra of the etched six-lobed dendritic and regular graphene crystals on Cu foil. For the dendritic graphene (position 1 of Figure 5-3 (c) FE-SEM image), graphitic G and second-order 2D Raman peaks are observed at around 1587 and 2712 cm^{-1} , respectively. The intensity of G peak is higher than that of 2D peak indicates more than a single layer graphene. The FWHM of G and 2D peaks are found to be around 19 and 50 cm^{-1} , respectively. Subsequently, for the regular graphene crystals (position 2 of Figure 5-3 (c) FE-SEM image), graphitic G and second-order 2D Raman peaks are observed at around 1588 and 2715 cm^{-1} , respectively. The higher intensity of 2D peak than that of G peak corresponds to monolayer or bi-layer graphene. The FWHM of G and 2D peaks are around 15 and 44 cm^{-1} , respectively. The Raman analysis shows a significant difference in structural morphology of the six-lobed dendritic graphene and other graphene crystals. This suggests non uniform growth of individual graphene crystals with the particular conditions of CVD process, which also affect the H_2 induced etching process. The etched graphene crystals were also investigated transferring to a SiO_2/Si substrate, where the color contrast indicates the thickness differences of graphene layers. Figure 5-4 (b) shows Raman spectra of the etched six-lobed dendritic and regular graphene on SiO_2/Si substrate. For the dendritic graphene (position 1 of Figure 5-2 (a)), graphitic G and second-order 2D Raman peaks are observed around 1580 and 2698 cm^{-1} , respectively. The FWHM of G and 2D peaks are around 22 and 64 cm^{-1} , respectively. Similarly, for the regular graphene (position 2 of Figure 5-2 (a)), graphitic G and second-order 2D Raman peaks were observed around 1588 and 2715 cm^{-1} , respectively. The higher intensity of 2D peak than that of G peak corresponds to monolayer graphene. Again, FWHM of G and 2D

peaks are obtained as 19 and 33 cm^{-1} , respectively. The Raman analysis of six-lobed dendritic graphene on Cu foil and SiO_2/Si substrate shows similar few-layer characteristics. This is due to fact that the six-lobed snowflake dendrite can grow faster than that of regular graphene crystals.[14] For a longer growth duration, growth of dendritic graphene crystals progress faster to form few-layer structure, while the regular crystals form monolayer or bilayer. Figure 5-4(c) shows Raman spectra of the hexagonal stacked graphene crystals at three different points. The graphitic G and second-order 2D Raman peaks for all three positions were observed around 1590 and 2698 cm^{-1} , respectively. At position 1 of Figure 5-2 (b), the 2D peak intensity is around 4 times higher than that of G peak, corresponding to monolayer graphene. At positions 2 and 3 of Figure 5-2 (b), the 2D peak intensity reduced corresponding to a bi- and tri-layer hexagonal graphene, respectively. The H_2 induced etching of dendritic graphene and edges of larger hexagonal graphene is observed for the hierarchical structure as well. The branches and lobes of the dendritic crystals were pronounced, whereas the hexagonal graphene etching creates clear edges. Thus, these results show significant difference in H_2 induced etching process of the graphene crystals depending on their original structures.

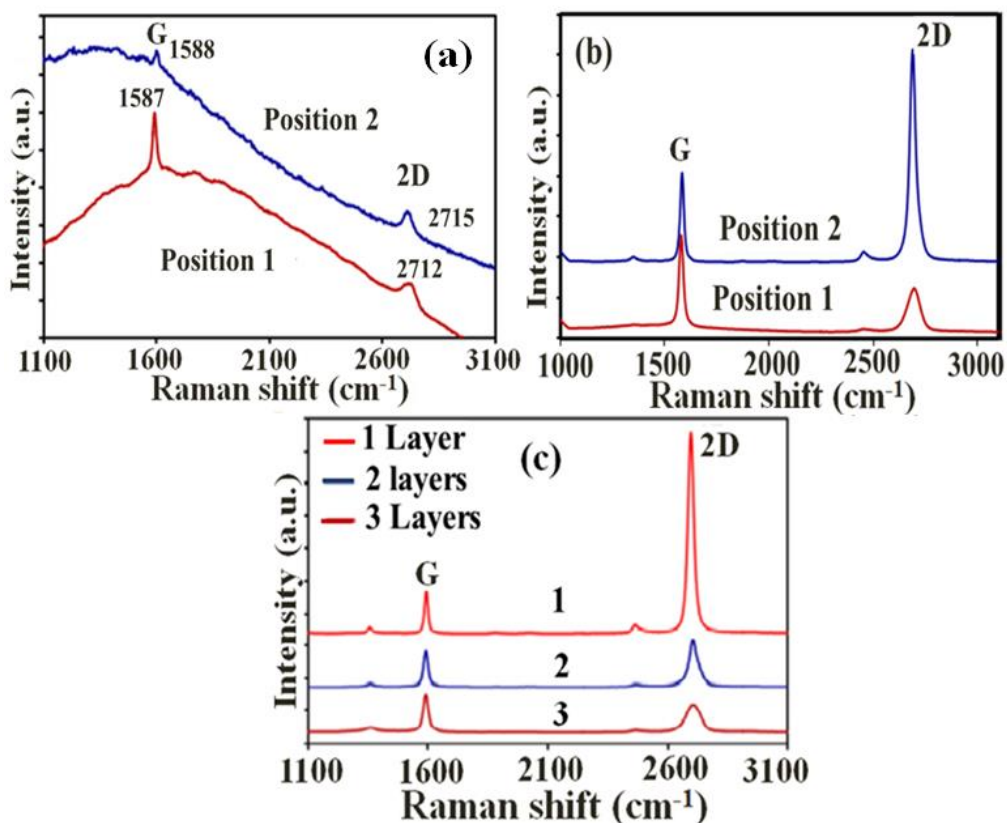


Figure 5-4. Raman spectra of etched (a) six-lobed dendritic graphene and regular graphene (position 1 of Figure 5-3 (c)). (b) Raman spectra of etched six-lobed dendritic graphene and regular graphene crystal (position 1 and 2 of Figure 5-2 (a)) on SiO₂/Si substrate (c) Raman spectra of the hexagonal stacked graphene crystals at three different points (mentioned in the Figure 5-2 (b))

5.4 Conclusions

In conclusions, we have demonstrated H₂ induced etching features of graphene crystals with different structures. We synthesized six-lobed dendritic graphene along with regular graphene crystals on electro-polished Cu foil by an APCVD process. Significant differences in H₂ induced etching behavior were observed for the snowflake-dendritic and

regular graphene crystal by annealing at 1055° C in a gas mixture of H₂ and Ar. Depending on the original structures anisotropic and fractal etching behavior of the graphene domains were observed. The etching of all snowflake dendritic crystals occurred from the branches of lobes creating symmetrical fractal pattern. Simultaneously, the regular crystals were etched anisotropically to form hexagonal hole and ribbon like structures with pronounced edges. The hexagonal-hexagonal stacking (stacking of three hexagonal layers) formation along with the snowflake dendritic crystals and their particular etching behavior also was observed. This finding can be significant to understand the nucleation and growth of graphene crystals as well as their selective etching process to fabricate well-defined structures.

5.5 References

- [1] S. Bae, H. K. Kim, Y. Lee, X. Xu, J. Park, Y. Zheng, J. Balakrishnan, D. Im, T. Lei, Y. Song, Y. Kim, K. Kim, B. Ozyimaz, J. Ahn, B. Hong, and S. Iijima, *Nat. Nanotechnol.* 2010, 5, 574.
- [2] K. S. Kim, Y. Zhao, H. Jang, S. Y. Lee, J. M. Kim, K. S. Kim, J. H. Ahn, P. Kim, J. Y. Choi, and B. H. Hong, *Nature* 2009, 457, 706.
- [3] X. S. Li, W. W. Cai, J. H. An, S. Kim, J. Nah, D. X. Yang, R. Piner, A. Velamakanni, I. Jung, E. Tutuc, S. K. Banerjee, L. Colombo, and R. S. Ruoff, *Science* 2009, 324, 1312.
- [4] S. Sharma, G. Kalita, R. Hirano, S. M. Shinde, R. Papon, H. Ohtani, and M. Tanemura, *Carbon* 2014, 72, 66.
- [5] H. Wang, G. Wang, P. Bao, S. Yang, W. Zhu, X. Xie, and W. J. Zhang, *J. Am. Chem. Soc.* 2012, 134, 3627 .
- [6] Y. Hao, M. S. Bharathi, L. Wang, Y. Liu, H. Chen, S. Nie, X. Wang, H. Chou, C. Tan, B. Fallahazad, H. Ramanarayan, C. W. Magnuson, E. Tutuc, B. I. Yakobson, K. F. McCarty, Y. W. Zhang, P. Kim, J. Hone, L. Colombo, and R. S. Ruoff, *Science* 2013,

342, 720–723 .

- [7] L. Gao, W. Ren, H. Xu, L. Jin, Z. Wang, T. Ma, L. P. Ma, Z. Zhang, Q. Fu, L. M. Peng, X. Bao, and H. M. Cheng, *Nat. Commun.* 2012, 3, 699.
- [8] Z. Yan, J. Lin, Z. Peng, Z. Sun, Y. Zhu, L. Li, C. Xiang, E. L. Samuel, C. Kittrell, and J. M. Tour, *ACS Nano* 2012, 6, 9110–9117 .
- [9] W. Wu, L. A. Jauregui, Z. Su, Z. Liu, J. Bao, Y. P. Chen, and Q. Yu, *Adv. Mater.* 2011, 23(42), 4898–4903.
- [10] H. Zhou, W. J. Yu, L. Liu, R. Cheng, Y. Chen, X. Huang, Y. Liu, Y. Wang, Y. Huang, and X. Duan, *Nat. Commun.* 2013, 4, 2096.
- [11] S. Zhu, Q. Li, Q. Chen, W. Liu, X. Li, J. Zhang, Q. Wang, X. Wang, and H. Liu, *RSC Adv.* 2014, 4, 32941–32945 .
- [12] V. Miseikis, D. Convertino, N. Mishra, M. Gemmi, T. Mashoff, S. Heun, N. Haghghian, F. Bisio, M. Canepa, V. Piazza, and C. Coletti, *2D Mater.* 2015, 2, 014006.
- [13] I. Vlassioux, P. Fulvio, H. Meyer, N. Lavrik, S. Dai, P. Datskos, and S. Smirnov, *Carbon* 2013, 54, 58–67.
- [14] P. Zhao, A. Kumamoto, S. Kim, X. Chen, B. Hou, S. Chiashi, E. Einarsson, Y. Ikuhara, and S. Maruyama, *J. Phys. Chem. C* 2013, 117, 10755–10763 .
- [15] T. Wu, G. Ding, H. Shen, H. Wang, L. Sun, D. Jiang, X. Xie, and M. Jiang, *Adv. Funct. Mater.* 2013, 23, 198–203.
- [16] B. Hu, H. Ago, Y. Ito, K. Kawahara, M. Tsuji, E. Magome, K. Sumitani, N. Mizuta, K. Ikeda, and S. Mizuno, *Carbon* 2012, 50, 57–65.
- [17] J. D. Wood, S. W. Schmucker, A. S. Lyons, E. Pop, and J. W. Lyding, *Nano Lett.* 2011, 11, 4547–4554.
- [18] B. Luo, B. Chen, L. Meng, D. Geng, H. Liu, J. Xu, Z. Zhang, H. Zhang, L. Peng, L. He,

- W. Hu, Y. Liu, and G. Yu, *Adv. Mater.* 2014, 26, 3218–3224.
- [19] M. Qi, Z. Ren, Y. Jiao, Y. Zhou, X. Xu, W. Li, J. Li, X. Zheng, and J. Bai, *J. Phys. Chem. C* 2013, 117(27), 14348–14353.
- [20] T. Ma, W. Rena, X. Zhang, Z. Liu, Y. Gao, L. C. Yin, X. L. Ma, F. Ding, and H. M.Cheng, *Proc. Natl. Acad. Sci. U.S.A.* 2013, 110, 20386–20391.
- [21] D. H. Jung, C. Kang, D. Yoon, H. Cheong, and J. S. Lee, *Carbon* 2015, 89, 242–248 .
- [22] L. C. Campos, V. R. Manfrinato, J. D. Sanchez-Yamagishi, J. Kong, and P.Jarillo-Herrero, *Nano Lett.* 2009, 9, 2600–2604.
- [23] L. Ci, Z. Xu, L. Wang, W. Gao, F. Ding, K. F. Kelly, B. I. Yakobson, and P. M. Ajayan, *Nano Res.* 2008, 1, 116–122.
- [24] R. Papon, S. Sharma, S. M. Shinde, A. Thangaraja, G. Kalita, and M. Tanemura, *RSC Adv.* 2015, 5, 35297–35301.
- [25] R. Yang, L. Zhang, Y. Wang, Z. Shi, D. Shi, H. Gao, E. Wang, and G. Zhang, *Adv. Mater.* 2010, 22, 4014–4019.
- [26] D. Luo, F. Yang, X. Wang, H. Sun, D. Gao, R. Li, J. Yang, and Y. Li, *Small* 2014, 10, 2809–2814.
- [27] H. Ago, Y. Kayo, P. Solis-Fernandez, K. Yoshida, and M. Tsuji, *Carbon* 2014, 78, 339–346.
- [28] D. Geng, B. Wu, Y. Guo, B. Luo, Y. Xue, J. Chen, G. Yu, and Y. Liu, *J. Am. Chem. Soc.* 2013, 135, 6431–6434.
- [29] L. Liu, J. Park, D. A. Siegel, K. F. McCarty, K. W. Clark, W. Deng, L. Basile, J. C. Idrobo, A. P. Li, and G. Gu, *Science* 2014, 343, 163–167.
- [30] Y.-W. Son, M. L. Cohen, and S. G. Louie, *Nature* 2006, 444, 347–349.
- [31] Z. Chen, Y. M. Lin, M. J. Rooks, and P. Avouris, *Physica E* 2007, 40, 228–232.

- [32] K. A. Ritter and J. W. Lyding, *Nat. Mater.* 2009, 8, 235–242.
- [33] W. S. Hwang, P. Zhao, K. Tahy, L. O. Nyakiti, V. D. Wheeler, R. L. Myers-Ward, C. R. Eddy, D. K. Gaskill, J. A. Robinson, W. Haensch, H. Xing, A. Seabaugh, and D. Jena, *APL Mater.* 2015, 3, 011101.
- [34] B. Wu, D. Geng, Z. Xu, Y. Guo, L. Huang, Y. Xue, J. Chen, G. Yu, and Y. Liu, *NPG Asia Mater.* 2013, 5, e36.

CHAPTER 6

Direct Growth of WS₂ crystals on CVD grown graphene and hBN

6.1 Introduction

TMDCs have attracted significant attention in recent years due to their intriguing physical and chemical properties.[1, 2] In particular, monolayer Mo and W-based TMDCs (MoS₂, MoSe₂, WS₂, WSe₂, etc.), which become direct band gap semiconductors, exhibit excellent on/off current ratios in FETs [3, 4] strong PL, [5-8] and unique spin-valley physics.[9-11] Therefore, TMDCs are expected to be a possible component in future electronic and optoelectronic devices.[1, 12] However, the quality of available samples still poses serious problems, such as in homogeneous lattice strain, charge doping, and structural defects. For example, high-resolution electron microscopy reveals various structural defects, such as monosulfur and disulfur vacancies in TMDCs. [13]

In recent years, many studies have been reported for the growth of high-quality TMDCs, mainly using CVD and metal film sulfurization. [20-29] In particular, several groups have used atomically flat surfaces of graphite (or graphene) and hBN as the growth substrates of TMDCs.[25-30] Considering monolayer growth on commonly used substrates such as SiO₂/Si and sapphire, this indicates that the growth substrate is one of the essential factors for reducing charged impurities and structural defects. Monolayer WS₂ grown by CVD on h-BN was very recently reported to exhibit a PL peak with a relatively narrow fwhm of 26 meV and a weak asymmetric profile.[25] h-BN has been proven to be the best substrate to observe intrinsic properties of atomic-layer materials.[14] h-BN is an insulator with a bandgap of about 6.4 eV and has the identical structure of graphene with boron and nitrogen atoms occupying the A and B sub lattices.[15, 16] h-BN can, therefore, provide an atomically flat surface without dangling bonds and charged impurity: one can mimic the free-standing situation using h-BN as substrates.

In fact, very high carrier mobility ($\sim 60\,000\text{ cm}^2\text{ V}^{-1}\text{ s}^{-1}$ at room temperature) has been reported on graphene transferred onto h-BN, Opening the possibilities of exploring new physics and electronics applications of graphene [17]. TMDCs sitting on h-BN are therefore the key structure to explore the intrinsic physical properties of TMDCs such as the photoinduced spin-Hall effect and the valley Hall effect. [19]

Here, we report the growth of high-quality monolayer WS_2 on a transferred CVD grown graphene and h-BN by CVD. Although the TMDC/h-BN structure can also be realized by the mechanical-exfoliation transfer method, the formation of TMDC/h-BN or graphene by direct CVD growth has great advantages over the transfer method. [18] We have used transferred CVD graphene and h-BN to cover the large area because exfoliated samples are usually few microns. Exfoliated samples are not suitable for large area applications. The single-crystal domains are triangular shaped with sizes of up to $2\text{-}7\ \mu\text{m}$.

6.2 Materials and methods

As explained in the chapter 2 section 2.1.1 (A)

Graphene transfer

As explained in the chapter 2 section 2.2.2

6.3 Results and discussion

The growth of individual crystal with sulfurization of WO_3 powder on a transferred graphene and h-BN substrate is investigated by atmospheric chemical vapor deposition method.

Optical Microscopy Study

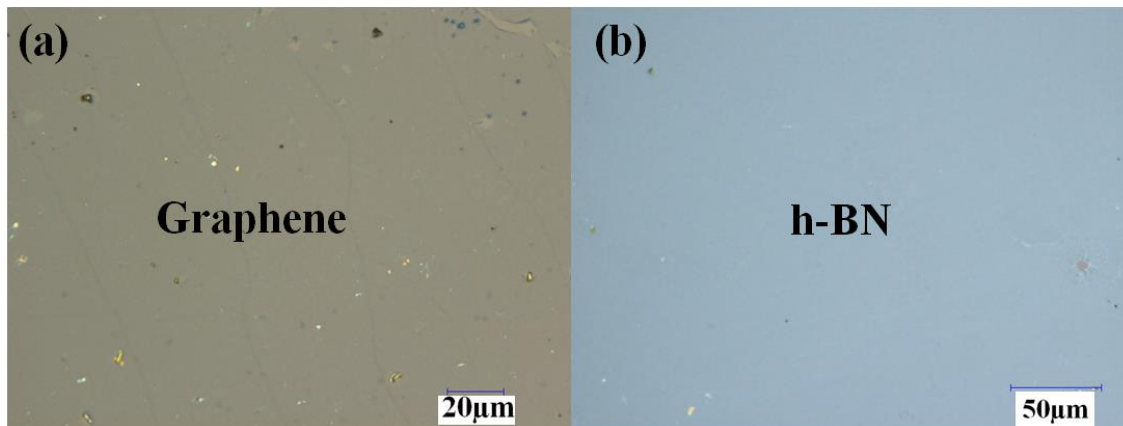


Figure 6-1 Optical microscopy images of (a) Graphene on SiO₂/Si (b) h-BN on SiO₂/Si

Figure 6-1(a) and (b) shows optical microscopy images of transferred graphene and h-BN on SiO₂/Si substrate for WS₂ crystals growth..

SEM Study

Synthesized materials are characterized by Scanning electron microscopy. Figure 6-2 (a) and (b) shows formation of WS₂ crystals on the graphene transferred SiO₂/Si substrate with sulfurization of the densely spread WO₃ powder at 750 °C. The size of obtained WS₂ triangular crystal is around 2-5 µm. In this case we are able to grow WS₂ crystals by spreading less amount of WO₃ powder on the substrate to reduce the nucleation site. We also observed vertically aligned WS₂ crystal on graphene and SiO₂/Si substrate. We have obtained vertically aligned WS₂ crystal on both substrate from densely spread WO₃ powder. Figure 6-3 (a) and (b) shows FE-SEM image of vertically aligned WS₂ crystals on SiO₂ and graphene transferred on SiO₂/Si substrate.

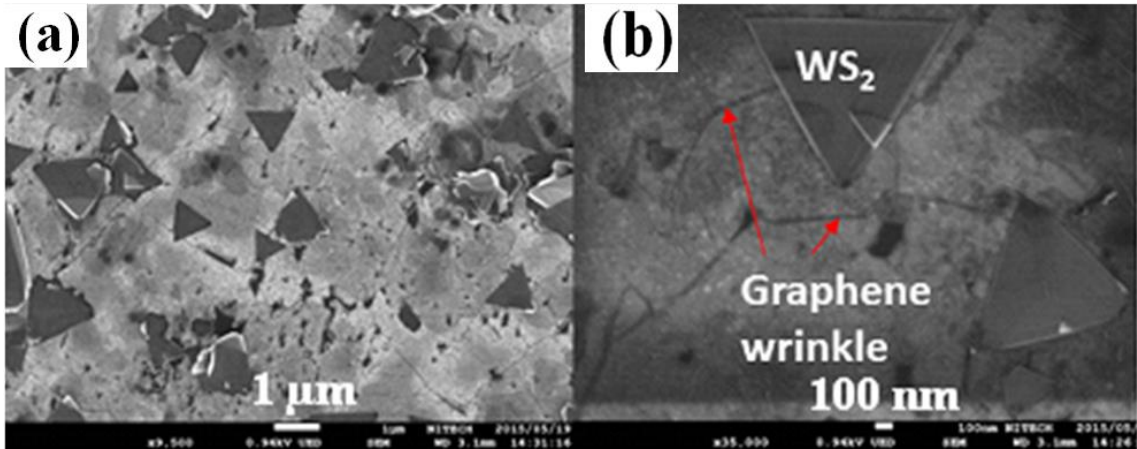


Figure 6-2 FE-SEM images of WS₂ triangular crystals on transferred graphene.

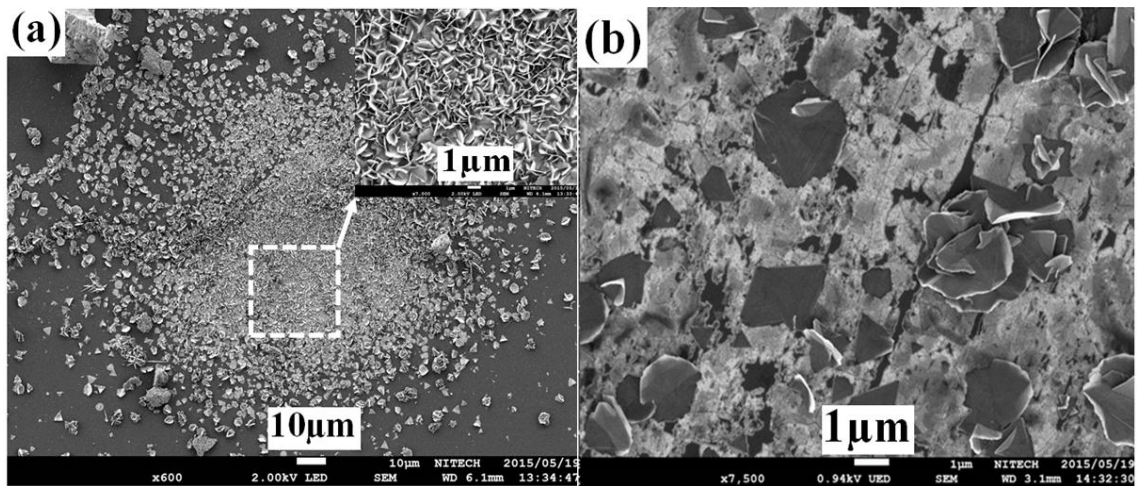


Figure 6-3 FE-SEM image of vertically aligned WS₂ crystal on (a) SiO₂/Si substrate and insert image is magnified view of vertically aligned WS₂ crystal (b) Graphene

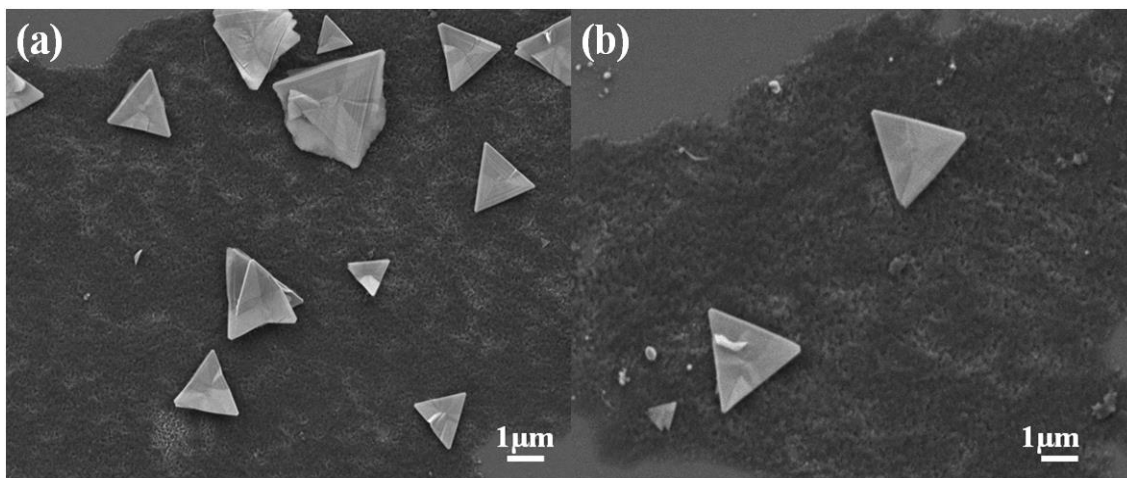


Figure 6-4 FE-SEM images of WS₂ triangular crystals on transferred h-BN.

6-4 (a) shows FE-SEM image of WS₂ crystals on transferred h-BN. On h-BN also we have observed the size of WS₂ triangular crystal is around 2-7 μm. We are able to grow WS₂ crystals on h-BN by using same method as graphene. Spreading less amount of WO₃ powder on the substrate to reduce the nucleation site and at the same time its help to stimulate the crystals growth.

Raman Study

We have carried out the Raman spectra studies for further confirmation of WS₂ crystals on graphene and h-BN substrate.

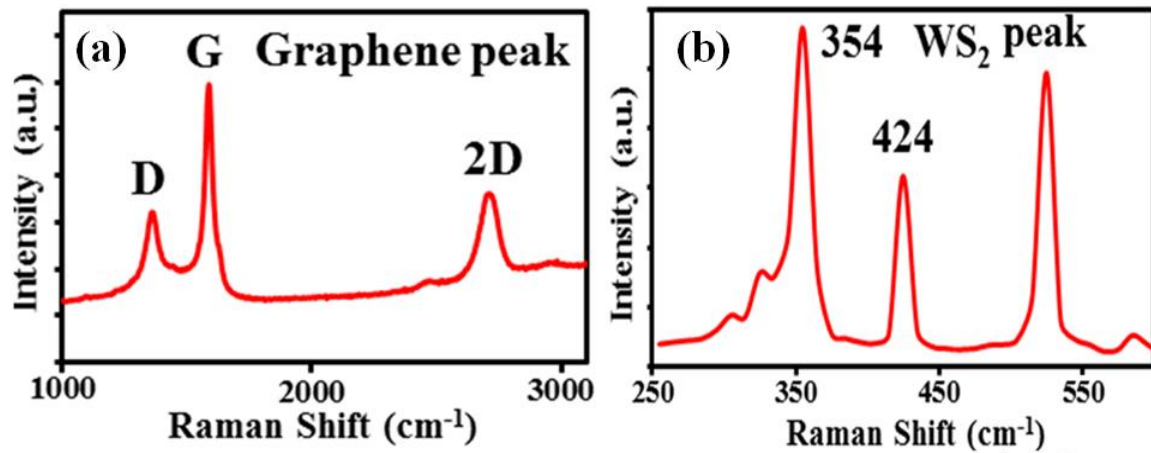


Figure 6-5. Raman spectra of (a) Graphene on SiO₂/Si (b) WS₂ crystal on SiO₂/Si.

Figure 6-5 (a) shows Raman spectra of Graphene on SiO₂/Si. Graphene can be identified by the position and shape of its G (1580 cm⁻¹) and 2D (2890 cm⁻¹) peak. Figure 6-5 (b) shows a Raman spectra of WS₂ crystals SiO₂/Si. The peaks for E_{12g}¹ and A_{1g} mode are observed at ~354 and 424 cm⁻¹, respectively. We observed higher intense A_{1g} peak, corresponding to the few-layer structure. The intensity ratio of two peaks (A_{1g}/E_{12g}¹) is around 0.56 which confirm it is a few layer WS₂ crystals.

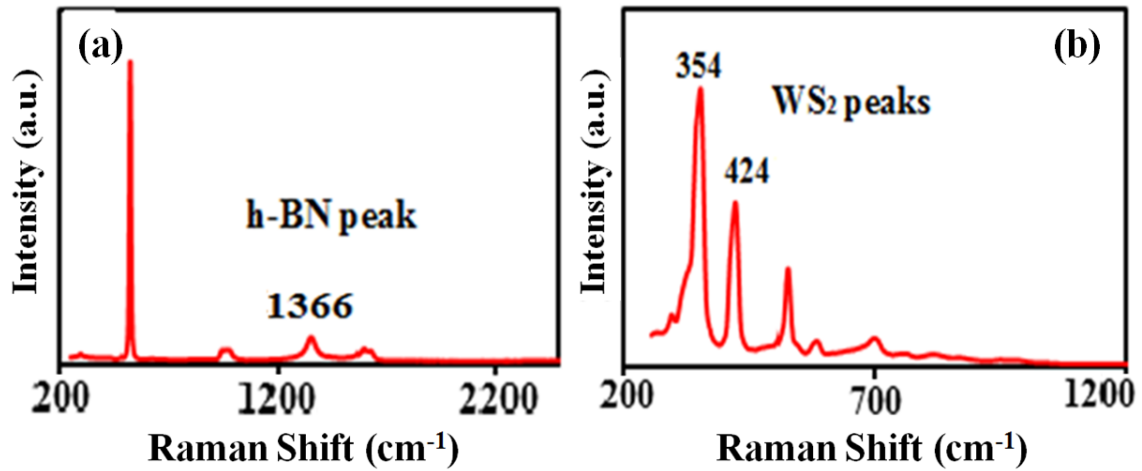


Figure 6-7. Raman spectra of (a) h-BN (b) WS₂ crystal on SiO₂/Si

Figure 6-7 shows Raman spectra of transferred h-BN SiO₂/Si substrate. For h-BN Raman peak occurs at 1366 cm⁻¹. The peaks for E_{12g}¹ and A_{1g} mode are observed at ~354 and 424 cm⁻¹, respectively. The high intensity of A_{1g} peak confirms its few layer WS₂ crystals. The frequency differences of the E_{12g}¹ and A_{1g} mode is around 70 cm⁻¹ where the two peaks intensity ratio (A_{1g}/E_{12g}¹) is around 0.55. The high intensity of the A_{1g} peak confirmed the few layer structure of the crystals.

6.4 Conclusions

We have investigated the WS₂ triangular crystals synthesis using WO₃ and S powder precursors on the CVD grown graphene and h-BN films by the APCVD technique. We observed that the quantity of WO₃ powder spread on the substrate surface significantly affects the nucleation and layer numbers of triangular-shaped WS₂ crystals. 2-7μm size WS₂ triangular crystals were obtained on a SiO₂/Si substrate than the substrates of graphene and h-BN. We observed the vertically aligned WS₂ sheet from densely spread WO₃ powder.

6.5 References

- [1]. Wang, Q. H.; Kalantar-Zadeh, K.; Kis, A.; Coleman, J. N.; Strano, M. S. *Nat. Nanotechnol.* 2012, 7, 699–712.
- [2]. Chhowalla, M.; Shin, H. S.; Eda, G.; Li, L.-J.; Loh, K. P.; Zhang, H. *Nat. Chem.* 2013, 5, 263–275.
- [3]. Radisavljevic, B.; Radenovic, A.; Brivio, J.; Giacometti, V.; Kis, A. Single-Layer MoS₂ Transistors. *Nat. Nanotechnol.* 2011, 6, 147–150.
- [4]. Ovchinnikov, D.; Allain, A.; Huang, Y.-S.; Dumcenco, D.; Kis, A. Electrical Transport Properties of Single-Layer WS₂. *ACS Nano* 2014, 8, 8174–8181.
- [5]. Zhao, W.; Ghorannevis, Z.; Chu, L.; Toh, M.; Kloc, C.; Tan, P.-H.; Eda, G. Evolution of Electronic Structure in Atomically Thin Sheets of WS₂ and WSe₂. *ACS Nano* 2012, 7, 791–797.
- [6]. Mak, K. F.; Lee, C.; Hone, J.; Shan, J.; Heinz, T. F. Atomically Thin MoS₂: A New Direct-Gap Semiconductor. *Phys. Rev. Lett.* 2010, 105, 136805.
- [7]. Splendiani, A.; Sun, L.; Zhang, Y.; Li, T.; Kim, J.; Chim, C.-Y.; Galli, G.; Wang, F. Emerging Photoluminescence in Monolayer MoS₂. *Nano Lett.* 2010, 10, 1271–1275.
- [8]. Eda, G.; Yamaguchi, H.; Voiry, D.; Fujita, T.; Chen, M.; Chhowalla, M. Photoluminescence from Chemically Exfoliated MoS₂. *Nano Lett.* 2011, 11, 5111–5116.
- [9]. Zhang, Y. J.; Oka, T.; Suzuki, R.; Ye, J. T.; Iwasa, Y. Electrically Switchable Chiral Light-Emitting Transistor. *Science* 2014, 344, 725–728. 1
- [10]. Zeng, H.; Dai, J.; Yao, W.; Xiao, D.; Cui, X. *Nat. Nanotechnol.* 2012, 7, 490–493.
- [11]. Mak, K. F.; He, K.; Shan, J.; Heinz, T. F. *Nat. Nanotechnol.* 2012, 7, 494–498.
- [12]. Huang, X.; Zeng, Z.; Zhang, H. *Chem. Soc. Rev.* 2013, 42, 1934–1946.

- [13] Zhou, W.; Zou, X.; Najmaei, S.; Liu, Z.; Shi, Y.; Kong, J.; Lou, J.; Ajayan, P. M.; Yakobson, B. I.; Idrobo, J.-C. *Nano Lett.* 2013, 13, 2615–2622. 14. Mak, K. F.; He, K.; Lee, C.; Lee
- [14] Dean, C. R.; Young, A. F.; Cadden-Zimansky, P.; Wang, L.; Ren, H.; Watanabe, K.; Taniguchi, T.; Kim, P.; Hone, J.; Shepard, K. L. *Nat. Phys.* 2011, 7, 693–696.
- [15] Watanabe, K.; Taniguchi, T.; Kanda, H. *Nat. Mater.* 2004, 3, 404–409.
- [16] Museur, L.; Brasse, G.; Pierret, A.; Maine, S.; Attal-Tretout, B.; Ducastelle, F.; Loiseau, A.; Barjon, J.; Watanabe, K.; Taniguchi, T.; et al. *Phys. Status Solidi-R* 2011, 5, 214–216.
- [17] Dean, C. R.; Young, A. F.; Meric, I.; Lee, C.; Wang, L.; Sorgenfrei, S.; Watanabe, K.; Taniguchi, T.; Kim, P.; Shepard, K. L.; et al. *Nat. Nanotechnol.* 2010, 5, 722–726.
- [18] Lee, G. H.; Yu, Y. J.; Cui, X.; Petrone, N.; Lee, C. H.; Choi, M. S.; Lee, D. Y.; Lee, C.; Yoo, W. J.; Watanabe, K.; et al. *ACS Nano*, 2013, 7, 7931–7936.
- [19] Xiao, D.; Liu, G. B.; Feng, W. X.; Xu, X. D.; Yao, W. *Phys. Rev. Lett.* 2012, 108, 196802
- [20] Wu, S.; Huang, C.; Aivazian, G.; Ross, J. S.; Cobden, D. H.; Xu, X. *ACS Nano* 2013, 7, 2768–2772.
- [21] van der Zande, A. M.; Huang, P. Y.; Chenet, D. A.; Berkelbach, T. C.; You, Y.; Lee, G.-H.; Heinz, T. F.; Reichman, D. R.; Muller, D. A.; Hone, J. C. *Nat. Mater.* 2013, 12, 554–561.
- [22] Lee, Y.-H.; Zhang, X.-Q.; Zhang, W.; Chang, M.-T.; Lin, C.-T.; Chang, K.-D.; Yu, Y.-C.; Wang, J. T.-W.; Chang, C.-S.; Li, L.-J.; et al. *Adv. Mater.* 2012, 24, 2320–2325.

- [23] Huang, J.-K.; Pu, J.; Hsu, C.-L.; Chiu, M.-H.; Juang, Z.-Y.; Chang, Y.-H.; Chang, W.-H.; Iwasa, Y.; Takenobu, T.; Li, L.-J. *ACS Nano* 2013, 8, 923–930.
- [24] Orofeo, C. M.; Suzuki, S.; Sekine, Y.; Hibino, H. *Appl. Phys. Lett.* 2014, 105, 083112.
- [25] Okada, M.; Sawazaki, T.; Watanabe, K.; Taniguchi, T.; Hibino, H.; Shinohara, H.; Kitaura, R. *ACS Nano* 2014, 8, 8273–8277.
- [26] Ge, W.; Kawahara, K.; Tsuji, M.; Ago, H. *Nanoscale* 2013, 5, 5773–5778.
- [27] Ling, X.; Lee, Y.-H.; Lin, Y.; Fang, W.; Yu, L.; Dresselhaus, M. S.; Kong, J. 2014, 14, 464–472.
- [28] Shi, Y.; Zhou, W.; Lu, A.-Y.; Fang, W.; Lee, Y.-H.; Hsu, A. L.; Kim, S. M.; Kim, K. K.; Yang, H. Y.; Li, L.-J.; et al. *Nano Lett.* 2012, 12, 2784–2791.
- [29] Zhang, C.; Johnson, A.; Hsu, C.-L.; Li, L.-J.; Shih, C.-K. *Nano Lett.* 2014, 14, 2443–2447.
- [30] Gutiérrez, H. R.; Perea-López, N.; Elías, A. L.; Berkdemir, A.; Wang, B.; Lv, R.; López-Urías, F.; Crespi, V. H.; Terrones, H.; Terrones, M. *Nano Lett.* 2012, 13, 3447–3454.

CHAPTER 7

Conclusions and future prospects

7.1 Conclusions

TMDCs, WS₂, have great attention due to their bandgap which is suitable for optoelectronics and nano-electronics applications. In this work high quality of WS₂ crystals were synthesized using APCVD technique. Various experimental parameters of the developed CVD process were optimized to synthesize large WS₂ monolayer crystals.

Chapter 1 describes mainly the general introduction of 2D materials with their physical and chemical properties, together with methods of their synthesis.

Chapter 2 deals with the experimental details, including APCVD for the synthesis of 2D materials and transfer methods for graphene and h-BN.

In chapter 3, the effect of sulfurization process and quantity of WO₃ precursor on the growth of WS₂ crystals is revealed. Pyramid-like few-layers stacked structure of WS₂ crystals were obtained from densely spread WO₃ powder. Larger triangular crystals (~70 μm) were obtained by reducing the amount of WO₃ precursor.

Chapter 4 deals with a simpler and effective approach to synthesis high quality monolayer WS₂ crystals using drop-casted WCl₆ precursor on SiO₂/Si substrate. The high quality WS₂ crystals grew using 0.05M WCl₆ precursor with well distribution of nucleation sites on the substrate. Depending on the amount of the precursor, various shapes of WS₂ crystals were formed, such as triangular, star-shaped, and dendritic structures of six arm-star-shaped, like a snowflake crystal. From the comparative study of precursors, it is concluded that the WO₃ precursor is suitable for the synthesis of higher quality WS₂ crystals.

Chapter 5 describes the H₂ induced etching features of graphene crystals of six-lobed dendritic structures along with regular hexagonal structures on electro-polished Cu foils. The etching of

all snowflake dendritic crystals occurred from the branches of lobes, creating symmetrical fractal pattern. On the other hand, the regular hexagonal crystals were etched anisotropically to form hexagonal hole and ribbon like structures with pronounced edges. It is believed that these findings should be fundamental to the formation of well-defined graphene structures with controlled edges for the future nano-electronics applications.

In Chapter 6, it is demonstrated that WS₂ triangular crystals of 2-7 μm in size were synthesized using WO₃ and S powder precursors on the CVD grown graphene and h-BN films. On the other hand, the vertically aligned WS₂ sheet formed using densely spread WO₃ powders on SiO₂/Si and graphene substrates.

Chapter 7 summarizes the whole thesis and future prospects.

7.2 Future prospects

As seen in Chapters 3 and 4, although 123 μm size WS₂ crystals were synthesized on SiO₂/Si substrate, the crystal size of WS₂ grown on graphene and h-BN was as small as 2-7 μm. This implies that the APCVD has the potential to grow the larger sized WS₂ also on graphene and h-BN. So the further optimization of the growth parameters or improvement of the APCVD system will be necessary to achieve growth of the larger crystals in the future work. In addition, extension in material synthesis from WS₂ to other TMDCs, such as MoS₂, WS₂, MoSe₂, WSe₂, NbS₂, SnS₂, will be interesting for wider range of applications. This will be also the future subjects.

List of research achievements

(A) Publications in international journals

- **Amutha Thangaraja**, Sachin M Shinde, G Kalita, M Tanemura, Effect of WO_3 precursor and sulfurization process on WS_2 crystals growth by atmospheric pressure CVD, Materials Letters, 156, 156-160, 2015.
- **Amutha Thangaraja**, Sachin M. Shinde, Golap Kalita, Remi Papon, Subash Sharma, Riteshkumar Vishwakarma, Kamal P. Sharma and Masaki Tanemura, Structure dependent hydrogen induced etching features of graphene, Appl. Phys. Lett., 106, 253106, 2015.
- **Amutha Thangaraja**, Sachin M Shinde, G Kalita, M Tanemura An effective approach to synthesis monolayer WS_2 crystals using tungsten halide precursor, Appl. Phys. Lett 108, 053104, 2016.

(B) Other publications

- Remi Papon, Subash Sharma, Sachin M Shinde, **Amutha Thangaraja**, Golap Kalita, and Masaki Tanemura, Formation of graphene nanoribbons and Y-junctions by hydrogen induced anisotropic etching, RSC Advance, 5, 35297-35301, 2015.
- Vishwakarma Riteshkumar; Sharma Subash; Shinde Sachin ; Sharma Kamal ; **Thangaraja Amutha**; Kalita Golap; Tanemura Masaki, Anisotropic etching of hexagonal boron nitride and boron-carbon-nitrogen basal plane for nanoribbons fabrication, Applied Physics Letters.79, 13-90, 2015.

(C) Conference presentation

- **Thangaraja Amutha**, Pradip Ghosh, M. Zamri Yusop and Masaki Tanemura Fabrication of Nano-ripple pattern of controllable dimension at Room temperature by Ion Irradiation method, IUMRS-ICA 2014, Fukuoka University, Fukuoka, Japan. August 24-30, 2014
- **Amutha Thangaraja**, Sachin M Shinde, G Kalita, M Tanemura, Effect of WO₃ precursor and sulfurization process on WS₂ crystals growth by atmospheric pressure CVD, The 76th JSAP Autumn Meeting , Nagoya Congress center, Nagoya, Japan, 13-16 September, 2015
- **Amutha Thangaraja**, Sachin M Shinde, G Kalita, M Tanemura Synthesis of WS₂ crystals on transferred graphene and hBN films by APCVD, 28th International Microprocesses and Nanotechnology Conference, Toyama International Conference Center, Toyama, Japan, November 10-13, 2015.
- **Amutha Thangaraja**, Sachin M. Shinde, Golap Kalita, Remi Papon, Subash Sharma, Riteshkumar Vishwakarma, Kamal P. Sharma and Masaki Tanemura (2015), Structure dependent hydrogen induced etching features of graphene, Appl. Phys. Lett., 106, 253106 JSAP SCTS, Nagoya University, Nagoya, Japan, November 2015 (Poster)

List of figures

- Figure 1-1** Schematic diagram of graphene with honeycomb lattice
- Figure 1-2** Graphene: the basic building block for other carbon allotropes, graphite (3D), fullerene (0D), and CNT (1D)
- Figure 1-3** Structure of h-BN is formed alternating by B and N atoms
- Figure 1-4** Boron nitride crystal structures
- Figure 1-5** Crystal structures of TMDs with a typical formula of MX_2 . (a) Three-dimensional model of the MoS_2 crystal structure. Reprinted with permission from ref [19]. Copyright 2011 Macmillan Publishers Ltd. (b) Unit cell structures of 2H- MX_2 and 1T- MX_2 .
- Figure 1-6** Layered structure of (a) graphite, (b) hexagonal boron nitride (h-BN), (c) molybdenum disulfide/ tungsten disulfide
- Figure 1-7** Electronic band gap structure of bulk and monolayer MoS_2 (reprinted with permission from Wang et al., 2012) [43]
- Figure 1-8** Electronic band gap structure of bulk and monolayer WS_2 (reprinted with permission from Wang et al., Nature Nanotechnology 2012) [43].
- Figure 1-9** Numerous applications of graphene.
- Figure 1-10** Numerous applications of BNNSs, MoS_2 , and WS_2
- Figure 1-11** An illustrative procedure of the Scotch-tape based micro- mechanical cleavage HOPG
- Figure.1-12** (a) Sonication of graphite dispersion giving graphene dispersion. (b) SEM image of the initial graphite flakes. (c) TEM image of the exfoliated graphene.

- Figure.1-13** Illustration of the mechanical mechanism for exfoliation via ball milling.
- Figure.1-14** Schematic description of them a in liquid exfoliation mechanisms. (A) Ion intercalation. (B) Ion exchange (C) Sonication- assisted exfoliation.
- Figure 2-1** Schematic diagram of experimental set up for WS₂ crystal synthesis
- Figure 2-3** Schematic diagram of drop casted WCl₆ solution on SiO₂/Si substrate
- Figure 2-4** Schematic diagram of graphene transfer process on the substrate
- Figure 3-1** Optical microscopy images of synthesized WS₂ crystals on SiO₂/Si substrate with sulfurization of the densely spread (a) 2mg WO₃ powder (b) 10mg WO₃ powder.
- Figure 3-2** FE-SEM images of synthesized WS₂ crystals on SiO₂/Si substrate with sulfurization of the densely spread WO₃ powder at (a), 750 0C and (b) 9500C.
- Figure 3-3** (a) FE-SEM image of triangular WS₂ crystals on SiO₂/Si substrate where the layers are stacked to form a pyramid-like structure. (b) Much larger triangular WS₂ crystals.
- Figure 3-4** (a)Raman spectra of the WS₂ crystal, presenting the plane vibrational (E¹_{2g}) and out of-plane vibrational (A_{1g}) mode at ~348.8 and ~419.8 cm⁻¹.(b)Raman spectra of the synthesized crystals, presenting the E¹_{2g} and A_{1g} mode peaks at ~348.8 and ~419.8 cm⁻¹.
- Figure 3-5** (a) and (b) Raman spectra of the WS₂ crystal at two different positions of (1 and 2) of figure 3-3(a)
- Figure 3-6** Raman spectra at the (a) edge, and (a) center part of the figure 3-1 (a)
- Figure 4-1** Optical microscope images of WS₂ crystals (a) with two different geometries on the same sample substrate, without changing any CVD parameters, (b) a triangular crystal. Six-arm star-shaped crystals with

(c) and without (d) additional layer structures from the nuclei

Figure 4-2 (a), (b) optical microscope image of triangular-shaped WS₂ crystal with lateral size of around 100 μm.

Figure 4-3 FE-SEM images of (a) triangular monolayer WS₂ crystal. (b) Uncompleted growth of triangular-shaped WS₂ crystal (size ~123 μm). FE-SEM images of WS₂ crystal with a geometry of (d) butterfly and (e) six-arm star-shaped

Figure 4-4 (a-d) FE-SEM images of the as-grown WS₂ crystals on SiO₂/Si substrates with various geometries.

Figure 4-5 (a) Formation of 3 pointed star-shaped WS₂ crystal. (b) Growth of WS₂ sheets vertically from the SiO₂/Si substrate surface with sulfurization of a cluster of WCl₆ precursor.

Figure 4-6 FE-SEM images of (a) star-shaped crystal with additional dendritic growth from the nuclei, (b) propagation of dendritic structure from the nuclei, (c) triangular crystal coexisting with other growth fronts and (d) dendritic growth fronts from the nuclei of the original crystal

Figure 4-7 Raman mapping images for the six-arm star-shaped crystal (a) E_{2g}¹ (363 cm⁻¹), (b) A_g¹ (430 cm⁻¹) peak intensities and (c) E_{2g}¹, (d) A_g¹ full width at half maximum (FWHM) of the peaks.

Figure 4-8 Raman mapping images for the triangular crystal (a) E_{2g}¹ (363 cm⁻¹), (b) A_g¹ (430 cm⁻¹) peak intensities and (c) E_{2g}¹, (d) A_g¹ FWHM of the peaks. (Laser excitation energy ~532.08 nm)

Figure 4-9 (a) Raman spectra of triangular WS₂ crystal and (b) Raman spectra of six armed star-shaped crystal (inset of the figure) at three different positions

(1, 2 and 3)

Figure 4-10 AFM image and line profile of the as-synthesized WS₂ crystal on SiO₂/Si substrate.

Figure 4-11 PL spectra of the triangular-shaped (inset of the figure) WS₂ crystal.

Figure 5-1 Optical microscope image of H₂ induced etching of (a) dendritic graphene along with regular graphene crystals (inset of the image magnified view). (b) Etching features of regular graphene. (c) Etched hierarchical graphene structures on Cu foil,

Figure. 5-2 Optical microscope image of (a) Etched graphene crystals after transferring to SiO₂/Si substrate. (b) Stacking of hexagonal-hexagonal-hexagonal graphene (stacking of three hexagonal layers) along with the snowflake dendritic crystals on SiO₂/Si.

Figure 5-3 FE-SEM image of the etched (a) six-lobed dendritic graphene crystals (inset of the image magnified view). (b) Regular graphene crystals across two Cu grains. (c) six-lobed dendritic graphene along with regular graphene crystals.

Figure5-2 Raman spectra of the etched (a) six-lobed dendritic graphene and regular graphene (position 1 of Figure5-3 (c)), (b) Raman spectra of etched six-lobed dendritic graphene and regular graphene crystal (position 1 and 2 of Figure 5-2 (a)) on SiO₂/Si substrate (c) Raman spectra of the hexagonal stacked graphene crystals at three different points (mentioned in the Figure 5-2 (b))

- Figure 6-1** Optical microscopy images of (a) Graphene on SiO₂/Si (b) h-BN on SiO₂/Si
- Figure 6-2** FE-SEM images of WS₂ triangular crystals on transferred graphene.
- Figure 6-3** FE-SEM image of vertically aligned WS₂ crystal on (a) SiO₂/Si substrate and insert image is magnified view of vertically aligned WS₂ crystal (b) Graphene substrate.
- Figure 6-4** FE-SEM images of WS₂ triangular crystals on transferred h-BN.
- Figure 6-5** Raman spectra of (a) Graphene on SiO₂/Si (b) WS₂ crystal on SiO₂/Si.
- Figure 6-7** Raman spectra of (a) h-BN (b) WS₂ crystal on SiO₂/Si

List of tables

- Table 2-1** Experimental parameters of WS₂ crystal synthesis using WO₃
- Table 2-3** Experimental parameters of WS₂ crystal synthesis using WCl₆